

FAR-INFRARED ABSORPTION OF  
ELECTRON-HOLE DROPS IN  
GERMANIUM

By



HILDA GRACIELA MALDONADO de ZÁRATE

A Thesis

Submitted to the School of Graduate Studies ,  
in Partial Fulfilment of the Requirements  
for the Degree  
Doctor of Philosophy

McMaster University

May, 1981

FAR-INFRARED ABSORPTION OF  
ELECTRON-HOLE DROPS IN  
GERMANIUM

DOCTOR OF PHILOSOPHY (1981)  
(Physics)

McMASTER UNIVERSITY  
Hamilton, Ontario

TITLE: Far-Infrared Absorption of Electron-Hole Drops  
in Germanium

AUTHOR: Hilda Graciela Maldonado de Zárate  
Licenciado en Ciencias Físicas (Universidad  
de Buenos Aires, Argentina)

SUPERVISOR: Dr. T. Timusk

NUMBER OF PAGES: xi, 127

## ABSTRACT

A detailed study is presented of the far-infrared absorption of electron-hole drops in germanium. Experimental observations in the frequency range 1 to 50 meV and at superfluid He temperatures are reported. The lineshape agrees well with Mie's theory of scattering of electromagnetic radiation from spheres with a dielectric constant that includes interband hole transitions and a frequency dependent damping, produced by electron-hole interaction. The electron-hole density is found to be  $(2.02 \pm 0.05) \times 10^{17} \text{ cm}^{-3}$ . The lineshape changes with excitation level. At low excitation surface effects are important, since drops are very small: within a layer of the excitonic Bohr radius the drops have a lower density, and the absorption is damped by collisions with the surface. At high excitation levels, the drops are larger and the absorption lineshape is explained including higher multipole terms in the Mie expansion. Estimates for the drop sizes are presented.

A study of the effect of uniaxial stress on the far-infrared absorption is conducted. Large variations in positions and lineshape are observed for different stress values and direction of polarization of the electric field with respect to the stress direction. The fit to the experimental results

to a theory with band structure modified by stress, allows the determination of the electron-hole density as a function of [111] stress, as well as a clearer understanding of the general properties of the fluid under the different conditions.

## ACKNOWLEDGEMENTS

I would like to thank my supervisor, Dr. T. Timusk, for his active and continuous advice and support throughout the course of this work, and to Dr. J. P. Carbotte for many helpful discussions. The cooperation of Dr. H. Navarro, P. Donders, Dr. F. Lin and P. Gillespie during many of the experiments is also gratefully acknowledged.

I thank Dr. S.M. Kelso, Dr. R.S. Markewicz, Dr. T.M. Rice, Dr. J.H. Rose and Dr. H.B. Shore for communicating unpublished results of their calculations. Dr. E.E. Haller and Dr. W.L. Hansen generously provided Ge samples.

I am also grateful to Mrs. H. Kennelly for her swift and accurate typing of this thesis and to S. Elliott for reviewing some of the sections.

I want to especially thank C. Zarate, who has been actively involved in this work, for all his help, useful technical advice and uncounted hours of discussion related to this thesis.

## TABLE OF CONTENTS

<u>CHAPTER</u>		<u>PAGE</u>
1	INTRODUCTION	1
2	EXPERIMENTAL TECHNIQUES	4
	2.1 Introduction	4
	2.2 Sample Preparation	4
	2.3 Experimental Set-up	6
	2.4 The Stress System	10
3	BASIC LINESHAPE OF THE PLASMA RESONANCE	14
	3.1 Introduction	14
	3.2 Band Structure	17
	3.3 Absorption of Light by Spheres: Mie Theory	21
	3.4 The Dynamic Dielectric Function	25
	3.5 The Frequency Dependent Damping	32
	3.6 Experimental Results	48
4	THE INFLUENCE OF DROPLET SIZE ON THE PLASMA RESONANCE	63
	4.1 Introduction	63
	4.2 The Line Shape of Drops with Radii Comparable to the Wavelength of Electromagnetic Radiation	64
	4.3 Surface Effects	65
	4.4 Experimental Results	67

<u>CHAPTER</u>		<u>PAGE</u>
5	THE INFLUENCE OF UNIAXIAL STRESS ON THE PLASMA RESONANCE	76
	5.1 Introduction	76
	5.2 The Absorption Cross Section for Small Drops Under Uniaxial Stress	79
	5.3 The Dielectric Function	80
	5.4 Experimental Results and Discussion	91
	5.5 Summary and Conclusions	107
6	CONCLUSIONS	110
	APPENDIX	114
	BIBLIOGRAPHY	122



LIST OF TABLES

<u>TABLE</u>		<u>PAGE</u>
1	Ge band structure parameters and effective masses	20
2	Experimental values of electron-hole pair density for EHD in Ge	62
3	Parameters used in Ge {111} calculations	87
4	Perpendicular plasma frequency and density for selected stress values	100

LIST OF FIGURES

<u>FIGURE</u>		<u>PAGE</u>
2-1	Inner view of the cryostat used in the experiments	8
2-2	The Stress system	11
2-3	Capacitor used as stress calibrator	13
3-1	Schematic energy band structure for germanium	18
3-2	Heavy and light-hole valence bands in germanium	29
3-3	Real ( $\epsilon_1$ ) and imaginary ( $\epsilon_2$ ) parts of the interband dielectric constant in units of $\epsilon_0$	31
3-4	Real ( $\epsilon_1$ ) and imaginary ( $\epsilon_2$ ) parts of the interband dielectric constant for damping comparable with the hole Fermi energy	33
3-5	Frequency-dependent damping produced by electron-hole scattering in Ge.	38
3-6	Integration regions for the hole interband polarization function in Ge	42
3-7	Frequency-dependent damping calculated considering the effect of the degeneracy of the valence band but taking the conduction band as isotropic	47
3-8	Overall electron-hole damping in Ge as a function of frequency	49
3-9	Absorption spectrum of EHD at 1.2°K from 2.5 to 30 meV	50
3-10	The low energy region of the absorption spectrum of EHD at 1.2°K	51

<u>FIGURE</u>		<u>PAGE</u>
3-11	The high-energy region of the absorption spectrum of LHD at 1.2°K	52
3-12	The low energy region of the spectrum at different temperatures (lines are shifted in 0.05 with respect to each other).	55
3-13	Overall absorption spectrum of EHD in Ge	57
3-14	Imaginary part of the interband dielectric constant with different matrix elements	60
4-1	Effect of the excitation level on the shape of the EHD absorption	70
4-2	Far-infrared spectrum of EHD at very low excitation levels	71
4-3	Change in the frequency of the low-energy half-maximum absorption point ( $E_{1/2}$ ) as a function of maximum absorption.	73
4-4	Calculated droplet radii as a function of absorption level.	74
5-1	Splitting of the conduction and valence bands for uniaxial compression along the [111] direction in Ge	82
5-2	Density-of-states masses for heavy and light holes in stressed Ge, as a function of reduced energy $E/S$	84
5-3	Longitudinal and transverse optical masses for heavy and light holes for [111] stressed Ge, as a function of reduced energy $E/S$	85
5-4	Imaginary part of the interband dielectric constant for several stress values for light polarized parallel to the stress direction	89
5-5	Imaginary part of the interband dielectric constant for several stress values for light polarized perpendicularly to the stress direction.	90

<u>FIGURE</u>		<u>PAGE</u>
5-6	Far-infrared absorption spectrum of EHD in Ge under small uniaxial stress for light polarized perpendicularly to the stress direction	92
5-7	Far-infrared absorption spectrum of EHD in Ge under intermediate uniaxial stress along [111] for light polarized along $[1\bar{1}0]$	93
5-8	Far-infrared absorption spectrum of EHD in Ge under $11 \text{ kg/mm}^2$ of [111] stress for light polarized along $[1\bar{1}0]$	94
5-9	Plasma resonance frequency of electron-hole drops for infrared light polarized perpendicularly to the stress direction as a function of stress, at $1.2^\circ\text{K}$	95
5-10	Absorption spectrum of electron-hole drops in Ge under [111] stress and perpendicular polarization	99
5-11	Square of the perpendicular resonance frequency as a function of reciprocal stress values	102
5-12	Far-infrared absorption of EHD in Ge with $1.5 \text{ kg/mm}^2$ of stress along [111] and parallel polarization.	103
5-13	Far-infrared absorption of EHD in Ge with $3.5 \text{ kg/mm}^2$ of stress along [111] and parallel polarization	104
5-14	Absorption spectrum of electron-hole drops in Ge under $7 \text{ kg/mm}^2$ , [111] stress and parallel polarization	106
6-1	Comparison between theoretical and experimental values of damping in Ge	112

## CHAPTER 1

### INTRODUCTION

The phenomenon of electron-hole condensation has drawn considerable attention from physicists in the last decade. The electron-hole liquid is a metal of a unique kind, being a better solid, state plasma than regular metals. A weaker coupling exists between its particles since they have low effective masses and the dielectric constant is larger. The fact that a Fermi Dirac condensation of electron-hole pairs into a metallic liquid occurs in semiconducting crystals is a fortunate circumstance. These solids, mostly Ge and Si, have a simple band structure which is well known, allowing the study of metals with relatively simple Fermi surfaces.

How and why is the liquid formed? When light of energy larger than the band gap strikes on a semiconductor crystal, electrons are excited to the conduction band, leaving behind holes in the valence band. At low temperatures, the electrons bind with the holes into hydrogen-like particles: the excitons. In indirect gap semiconductors, the recombination of electrons and holes is a slow process since the simultaneous participation of a phonon is necessary to conserve crystal momentum; hence high densities of excitons can be established. At sufficiently high concentrations and low temperatures a gas-

liquid phase transition occurs: the excitons condense into a metallic liquid, generally in the form of small drops in which the electron and holes are no longer bound into pairs. This plasma-like fluid was first proposed by Keldysh (1968) as the most stable phase for electrons and holes in his interpretation of photoconductivity experiments by Asnin et al. (1968). Several review articles have appeared about electron-hole drops (EHD); the most recently published are the ones by Rice (1977) for the theoretical aspects and Hensel et al. (1977) for the experiments. The dielectric response and conductivity of the fluid in a given spectral region can be obtained from the study of its electromagnetic properties at these frequencies. A particularly good probe for the study of EHD is far-infrared radiation, since the plasma frequency and inter valence band transitions occur in this region of the spectrum. The density of electron-hole pairs in the drop, the droplet size and relaxation times affect the absorption and scattering cross sections, hence the study of the far-infrared absorption spectra gives measures of these quantities.

In this thesis a detailed study of the absorption spectrum of the electron-hole liquid in Ge in the far-infrared is presented. The experimental results obtained by Fourier transform spectroscopy are compared with calculations of the dielectric function and conductivity.

The properties of the electron-hole fluid are determined by the particular band structure of the semiconductor that

is its host. Any alteration in the valence or conduction band will clearly affect the fluid. For this reason, application of uniaxial stress is clearly useful in the study of slow changes in the electron-hole liquid properties under small variations in band structure. In this thesis, the effect of uniaxial stress on the far infrared absorption is studied and the variations in the electron-hole fluid properties that produce such a change, is considered.

Chapter two of this thesis is a description of the experimental techniques used. Chapter three is a study of the basic lineshape of the EHD absorption spectrum. Experimental results are presented in this chapter as well as the theory necessary to understand them. Chapter four considers the influence of the droplet size on the plasma resonance, different droplet size being produced by changing excitation conditions. Chapter five is a study of the effect of uniaxial stress in the plasma resonance. Finally in chapter six results are summarized.

## CHAPTER 2

### EXPERIMENTAL TECHNIQUES

#### 2.1 Introduction

Electron-hole drops are obtained when a high purity germanium crystal is excited with a laser at a temperature below the critical point of the electron-hole liquid, which for Ge is around 6°K. If the crystal is at superfluid helium temperatures, most of the excitons are in the condensed phase and high concentrations of drops are generated with the laser.

Electron-hole drops have their plasma frequency in the far infrared. This makes radiation with wavelength in this region of the spectrum a good probe for the study of properties of the fluid. The best tool for the study of any optical properties in the far infrared is Fourier Transform Spectroscopy, and sensible detectors for these wavelengths are bolometers cooled at 0.3°K.

#### 2.2 Sample Preparation

The experimental absorption of EHD in unstressed Ge was measured on two samples with a concentration of electrically active impurities of less than  $2 \times 10^{10}$ , cut from crystals purchased from General Electric Company, Valley Forge, Pa. The dimensions of the samples were  $1 \times 6 \times 15 \text{ mm}^3$  and  $3 \times 15 \times 15 \text{ mm}^3$ . Most of the experiments were performed with the larger sample since a crystal



of large surface area minimizes the resistance to heat flow as described in section 6 of Chapter 3.

The large surface had a [100] orientation. This surface was exposed to the incoming radiation and was polished with  $1 \mu \text{ Al}_2\text{O}_3$ , then with Syton (a commercial product of Dow Corning Co.) and finally etched in CP4 (HF: acetic acid:  $\text{HNO}_3$ : liquid bromine in the approximate ratios 50:50:80:1). After three or four experiments the sample was repolished with Syton and etched. The samples used in the stress experiments were cut from a dislocation free Ge disc of 4 cm diameter and .8 cm thickness with the plane face perpendicular to [100], donated by E. E. Haller and grown by W.L. Hansen and E.E. Haller (E.E. Haller and W. L. Hansen, 1974). The concentration of electrically active impurities in this crystal was  $(N_A - N_D) \leq 2 \times 10^{11} \text{ cm}^{-3}$  where  $N_A$  and  $N_D$  are the concentration of acceptors and donors respectively.

After orientation using the Laue method, several rectangular samples were cut with sides along [111],  $[1\bar{1}0]$  and  $[11\bar{2}]$ . The longer dimension was always [111] along which the sample was stressed, and the smallest  $[11\bar{2}]$  was in the direction of the incoming radiation. The two samples used in most of the experiments had dimensions  $8.76 \times 5.54 \times 2.30 \text{ mm}^3$  and  $9.85 \times 3.56 \times 2.36 \text{ mm}^3$ . The second sample was generally preferred, especially for large stresses due to the smaller area perpendicular to the [111] direction.

The samples were cut with a diamond saw and the damage produced by the process removed by grinding and polishing. The surface facing the light as well as the two perpendicular to the stress direction were optically polished. Only the first one was etched with CP4A sometimes diluted with distilled water, and extreme care was taken that no etching of the [111] surfaces would occur to avoid any irregularities produced by the etching that would affect the homogeneity of the stress.

To generate electron-hole drops in the crystals a c.w. Y AlG:Nd laser was used . The 1.06  $\mu\text{m}$  wavelength of this laser (energy=1.17 eV) falls close to the band gap of Ge and provides a minimum amount of sample heating (Ge band gap: 0.744 eV at 0°K). In order to obtain a broad range of excitation levels, the output power of the laser and the focused spot on the crystal were varied. Absorbed powers ranging from 0.1 to 40 mW and spot sizes from 1 to 5 mm diameter were obtained. For the stress experiments the spot size was kept constant with a diameter of approximately 1 mm.

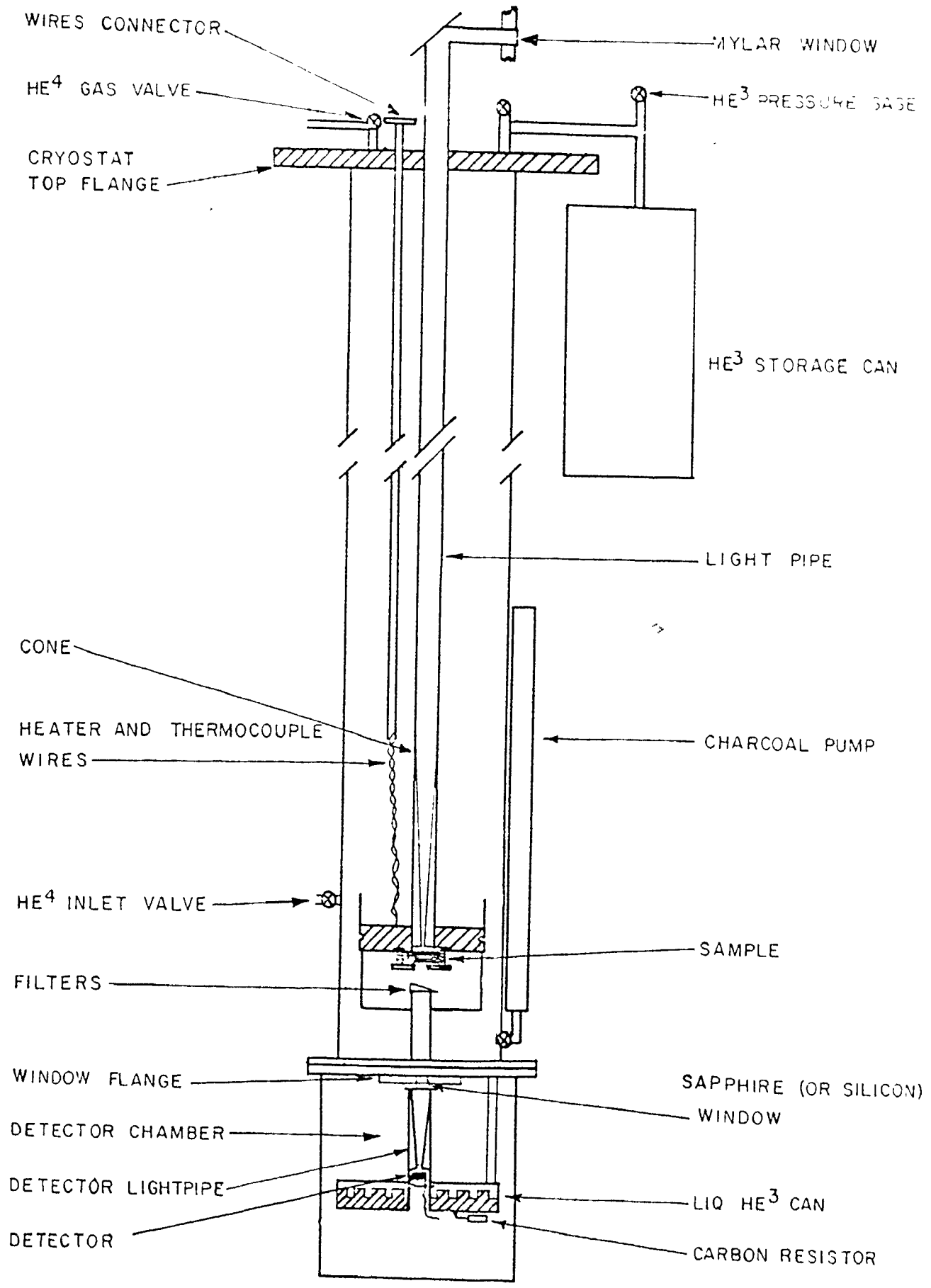
### 2.3 Experimental Set-up

The far infrared absorption experiments were done using Fourier transform spectroscopy. For measurements in the spectral range 4 to 50 meV (32 to 360  $\text{cm}^{-1}$ ) a RIIC FS720 Michelson interferometer was used. Its moving mirror was initially driven by a Slo-Syn #S25V stepping motor and in the later experiments by a linear motor with a hydrostatic pumped-oil bearing for rapid scan-

ning operation (T. Timusk, F. Lin (1979)). A lamellar grating interferometer (Beckman LR 100) was used for the measurements of the threshold region of EHD in unstressed Ge (1.5 to 5 meV). The latest measurements in stressed Ge were performed with a polarizing interferometer in the spectral region 0.4 to 18 meV. The light source was always a Hg lamp in a fused quartz envelope. After going through the sample, the light was filtered and detected. The amplified and processed signal was digitized with a A/D converter and its values stored in the memory of a 16 bit computer (Nova II, Data General Co.). After storing the data corresponding to a complete path of the moving mirror, that is an interferogram, the computer calculated the Fast Fourier Transform to obtain the spectrum. The computer also operated the interferometers through a series of interfaces, recorded and averaged the spectra, plotted and displayed them. Generally two sided interferograms were collected. Sometimes, as with the rapid scanning interferometer, interferograms were one sided and only a few points to the left of the central maximum were taken to allow phase correction of the interferogram. Light pipes take the infrared radiation from the interferometer to the sample, and from it to the detector. The radiation from the interferometer is fed through the window at the top of the light pipe in the upper right of figure 2.1. It is reflected towards the bottom at the flat mirror at  $45^\circ$  of the incoming light. A window at the centre of the mirror admits the laser beam into the light pipe to excite the sample in the same area where the f.i.r. was condensed to pass through by a cone.

Fig. 2-1

Inner view of the cryostat used in the experiments. It consists of two parts: the sample chamber, at the bottom of which the sample is mounted, and the detector chamber, almost completely thermally isolated from the first one. (After: Navarro, (1979)).



The sample is sandwiched between indium pads to improve the thermal contact with the sample holder and increase the effective area exposed to the superfluid He, minimized the superheating of the sample produced by the laser. The bath temperature was measured monitoring the He vapor pressure; for most of the experiments it was 1.2°K. The sample temperature was occasionally checked with a copper-gold 0.07% He thermocouple.

The detector is a heavily doped Ge bolometer (Drew and Severs, 1967), cooled to 0.3°K by a closed He<sup>3</sup> refrigeration system; its temperature was checked with a calibrated carbon resistor.

Various band-pass filters were placed between the sample and the detector to tailor the detected frequencies to the needs of the experiments. A sapphire window which eliminated the radiation above  $360\text{ cm}^{-1}$  (45 meV) was used in most cases. To study the high energy tail of EHD in unstressed Ge, this window was replaced by one of silicon that is transparent below  $700\text{ cm}^{-1}$  (85 meV). When necessary, the maximum transmitted frequency was further resolved using alkali halide filters, principally NaCl with a low cut-off of  $170\text{ cm}^{-1}$  (21 meV). White and near infrared light were eliminated either with black polyethylene or depositing a carbon layer on the alkali-halide filter.

#### 2.4 The Stress System

The stress device used allows the control of the force applied to the crystal from outside the cryostat. The stress chamber is illustrated schematically in figure 2.2. The 1/8" diameter steel rod at the left of the figure is pulled from the top of the cryostat and the necessary force is provided by a spring with a force constant  $k = 0.65 \text{ kg/mm}$ . The compression is controlled by a micrometer situated at the top of the pull rod. The small brass cylinder shown in the figure at the bottom of the pull rod constrains it to move only in the vertical direction. The vertical force is converted into horizontal and multiplied by the couple provided by the stress transmitter around the pivot axis. The dimensions of the system are such that the horizontal force is  $10 \pm 0.5$  times the one provided by the spring. The stress transmitter pushes the 1 cm disc brass cylinder shown in the figure through a ball bearing to eliminate non-horizontal components of the force. It, in turn, compresses the crystal against a wall. Resultant forces range between 0 and 100 kg, with a force constant of 16 kg per micrometer unit (0.1"). Thin folds of indium are placed before and after the sample to avoid non-uniform stress. The system is generally prestressed at room temperature to partially compress the indium, get good reproducibility of results and obtain best stress uniformity.

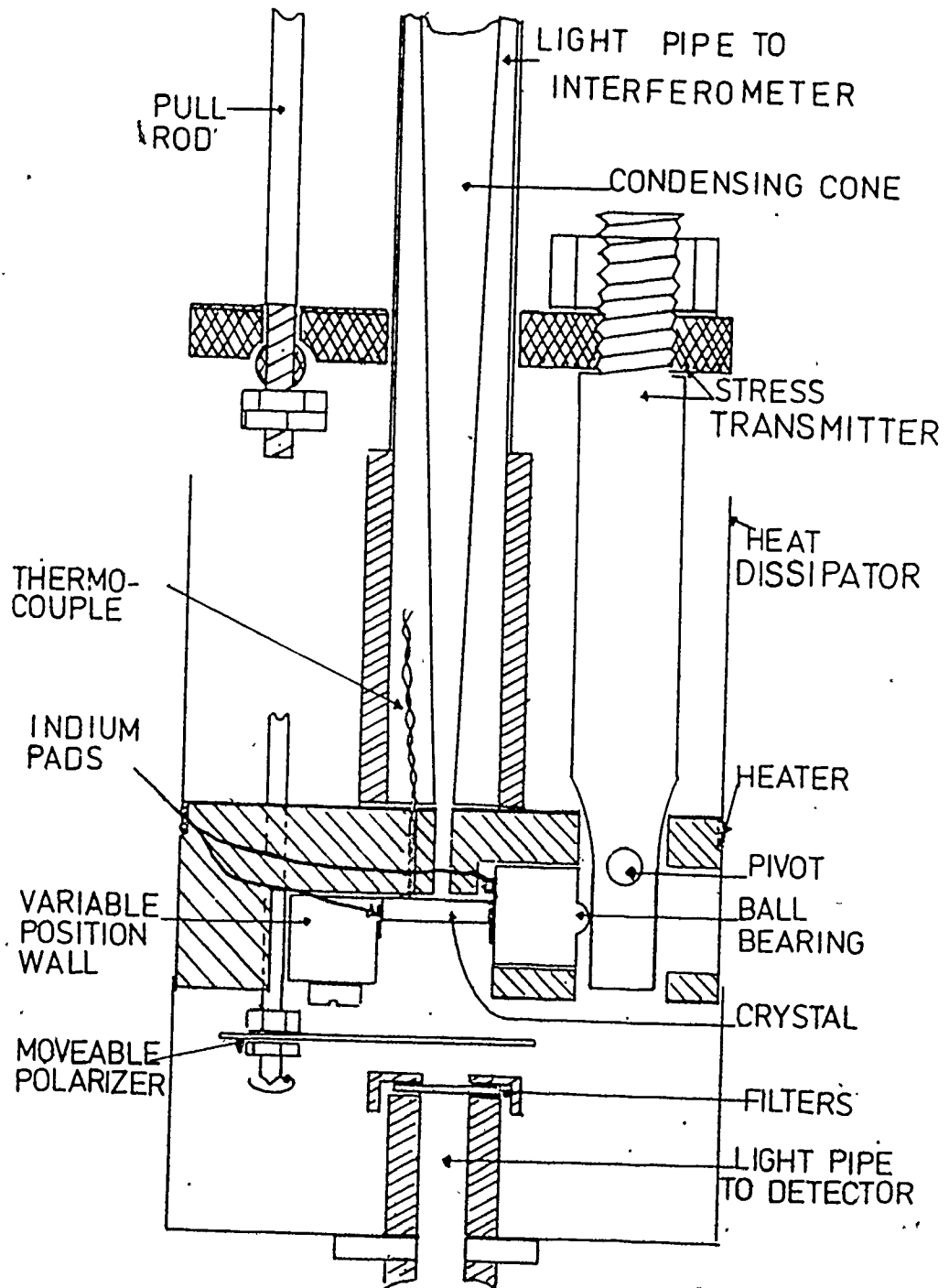
In order to check the calibration of the stress apparatus a capacitor was built by evaporating Al on two 6 mm diameter polished quartz rods and using a 50 G mylar sheet as dielectric

Fig. 2-2

The stress system: The rod at the left of the figure is pulled from outside the cryostat by a spring system (not shown). This vertical force is converted to a horizontal one and multiplied by the torque produced by the stress transmitter around the pivot axes. The crystal is pushed through a ball bearing perpendicularly to the incoming infrared light.







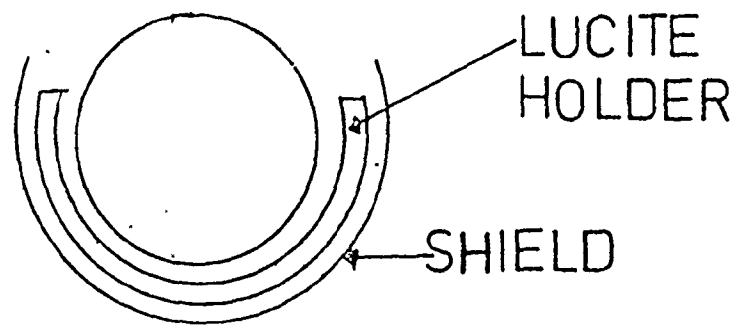
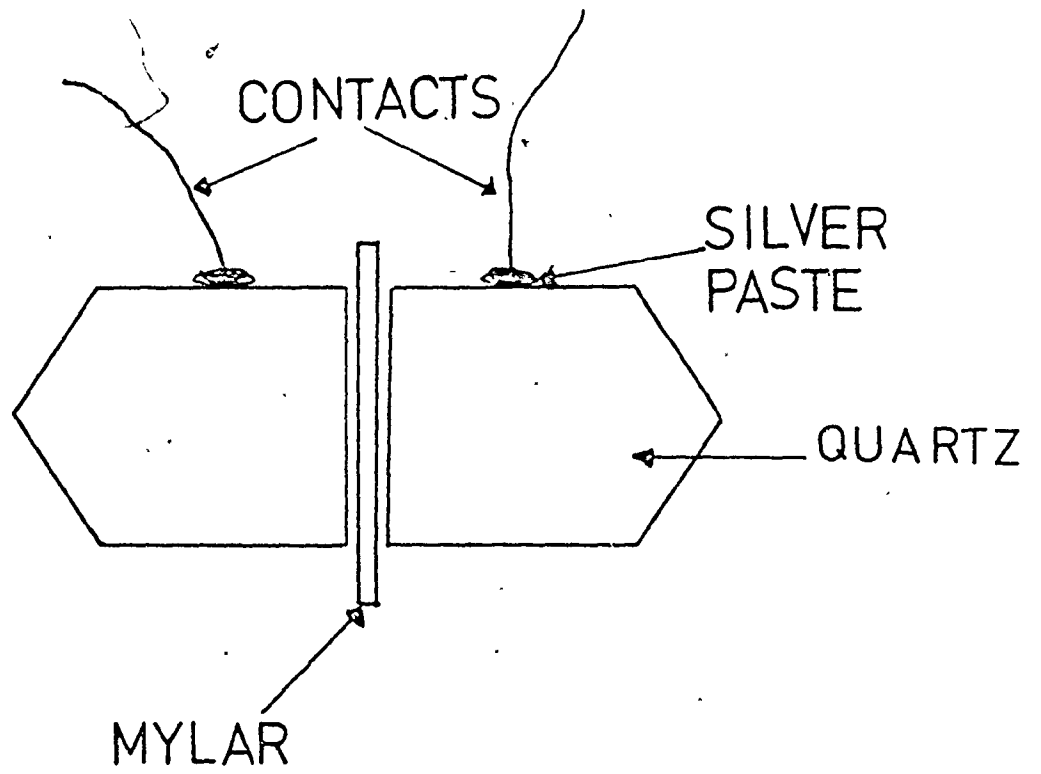
(see fig. 2-3). A force applied to the pointed ends of this apparatus will change the dielectric thickness hence the capacitance. Using the capacitor as one of the frequency determining parts of an oscillator, allows one to get a table of spring lengths against oscillator frequencies. By calibrating this capacitor using known forces the forces of the system can be obtained. The calibration was done at room and  $N_2$  temperatures.

As is clear from figure 2-2, the infrared light and exciting laser reaches the sample perpendicularly to the stress direction. A polarizer placed between the sample and detector allows one to study the effect on the absorption of the angle formed by the electric field and the stress direction. The polarizer used is a gold grid polarizer (Buckbee-Mears Company) with 1000 lines per inch on a mylar base.



Fig. 2-3

Capacitor used as stress calibrator. The thickness of the mylar dielectric changes when a force is applied to the quartz pointed ends, hence the capacitance varies, and these variations can be used to calibrate the forces on the stress apparatus.



## CHAPTER 3

### BASIC LINESHAPE OF THE PLASMA RESONANCE

#### 3.1 Introduction

Previous to this thesis, the far infrared absorption spectrum of electron-hole drops (EHD) in germanium has been measured by several investigators over a restricted range of energies and excitation levels (Vavilov, Zayats and Murzin, (1969); Timusk and Silin, (1975)). The absorption is a broad asymmetric line peaking at 9 mev. Vavilov et al. identified it as the resonant absorption of an electron-hole plasma. The position of the peak is related to the plasma frequency and can be used to obtain the density of the electron-hole fluid using elementary Drude theory. The fact that the line is very broad and asymmetric suggests a large and frequency dependent damping of the plasma oscillations; the aforementioned authors considered electron-hole collisions to be responsible for this damping. They used a quadratic frequency dependence that produces an asymmetric line. The quadratic frequency dependence is only valid for  $\hbar\omega \ll E_F$  (Gurzhi and Kaganov 1965) and the absolute value of the damping necessary to fit the data was too high, even for a strong mechanism such as electron-hole collisions.

Murzin, Zayats and Kononenko (1975) and independently Rose, Shore and Rice (1975,1978) pointed out that for a complete

description of the EHD dielectric constant it is necessary to include interband transitions between the heavy and light hole valence bands that occur in the frequency range of the plasma absorption. This extended model gave a good fit to Vavilov's experimental results, but it was still necessary to include damping constants as adjustable parameters for both the interband and intraband contributions. Since the damping affects the peak position, its calculation is necessary before an accurate estimate of the electron-hole pair density can be made.

In this chapter measurements of the EHD absorption over the range 1.5 meV to 50 meV are presented. This range includes the threshold and cutoff of the interband transitions. The aim of this chapter is a study of this line in some detail. Section 3.2 describes the band structure of Ge and shows the approximations used in the rest of the work. Section 3.3 deals with the calculation of the absorption cross section; a brief description of Mie theory for scattering and absorption by a sphere is presented. In section 3.4 the electron-hole liquid dielectric constant is calculated following Rose, Shore and Rice. Section 3.5 presents a calculation of the frequency dependent damping produced by electron-hole interactions. The treatment is based on calculations in the static approximation by Tzoar and Platzman (1976). The effects produced by the anisotropy of the conduction band and the splitting of the valence band are considered (Zarate, Carbotte and Timusk, 1980). Section 3.6 presents the

experimental results at 1.2°K and at an excitation level such that the dipole approximation holds. The experimental results are fitted to the theory presented in Sections 3.2, 3.3, 3.4 and 3.5 with the density as the only adjustable parameter. The electron-hole pair density is obtained from this fit and from the threshold and cut-off of the interband transitions.

Most of the results in this chapter have been published previously (Timusk and Zarate, 1977; Zarate and Timusk, 1979; Zarate, Carbotte and Timusk, 1980). In the second of these publications, a fit to the absorption spectrum using the damping calculated by Tzoar and Platzman for a set of parameters closer to the case of EHD in Ge, is presented. The experiments however show a sharp threshold at 2.8 meV; this fact can not be explained within that model since the predicted absorption would be larger than is actually observed. In that work the damping was reduced in the low energy region by an order of magnitude below the value calculated by Tzoar and Platzman to qualitatively account for anisotropy; in this way a very good fit to the data was obtained. This reduction of the damping at low frequencies is necessary to explain the far infrared absorption as well as the magneto plasma resonance results of Gavrilenko et al. (1976), who obtained damping values considerably smaller than those predicted by Tzoar and Platzman in the range 1.5 to 3 meV, and motivated the calculation of the frequency dependent damping presented in this thesis.

### 3.2 Band Structure

Germanium has the diamond structure, an fcc Bravais lattice with a primitive basis of two atoms at positions  $(0,0,0)$  and  $(\frac{1}{4}, \frac{1}{4}, \frac{1}{4})$ . Being a semiconductor, an energy gap separates the filled and empty states. Figure 3.1 shows the valence and conduction bands (Herman, 1955). The valence band maximum occurs at  $\bar{k} = 0$  ( $\Gamma$  point) and in the absence of spin orbit coupling it would be six-fold degenerate at this point. However, the spin-orbit interaction breaks it into a four-fold degenerate state ( $j = \frac{3}{2}$  and  $\Gamma_8^+$  symmetry) and a two-fold "split-off" band ( $j = \frac{1}{2}$  symmetry  $\Gamma_7^+$  with an energy difference between them of 0.29 eV. When  $\underline{k}$  moves away from the centre of the Brillouin zone the  $\Gamma_8^+$  level splits into heavy and light hole bands. These bands have a warped energy surface, and near  $\bar{k} = 0$  are given by (Dresselhaus, Kip and Kittel, 1955:

$$E_{\pm}(\underline{k}) = Ak^2 \pm [B^2k^4 + C^2(k_x^2k_y^2 + k_y^2k_z^2 + k_z^2k_x^2)]^{1/2}. \quad (3.2.1)$$

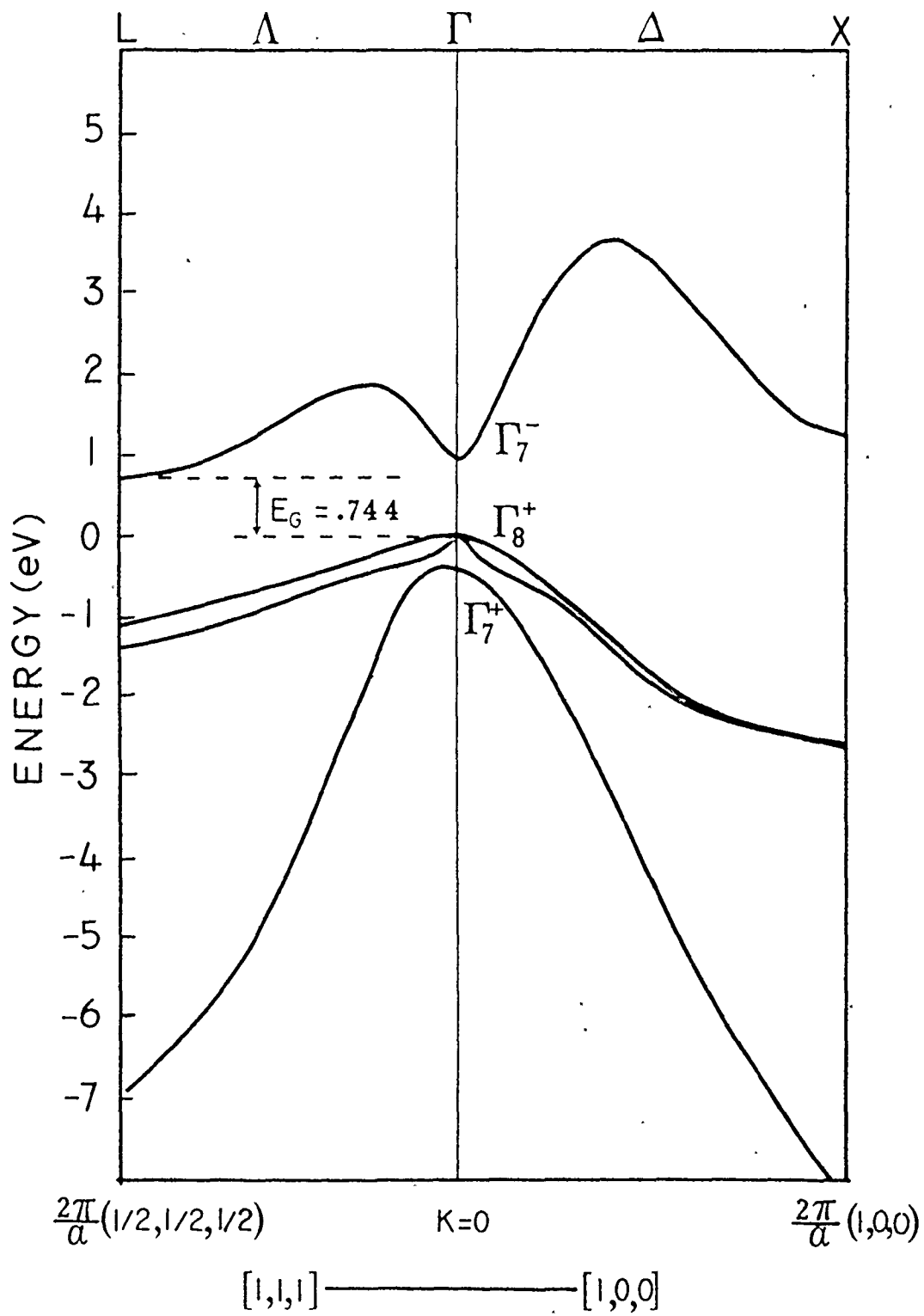
The values of the parameters A, B and C, determined by cyclotron resonance (Hensel and Suzuki, 1974) are listed in Table 1.

The electron minima are located at the L points, which are at the zone boundaries in the  $\{111\}$  directions, producing four equivalent electron minima. The constant energy surfaces are very elongated ellipsoids of revolution, with ratio between the major and minor axes of around 20.



Fig. 3-1

Schematic energy band structure for germanium. The conduction and valence bands are shown. The conduction band minimum at the L point is .744 eV above the valence band maximum at the  $\Gamma$  point. The two upper valence bands correspond to electron states with  $J = \frac{3}{2}$ . The split-off band of  $J = \frac{1}{2}$  is .29 eV below the two other valence bands at the  $\Gamma$  point.



The fact that the conduction band minimum and valence band maximum are separated in  $\underline{k}$  space makes Ge an indirect gap semiconductor. In these materials optical recombination is a slow process since it can occur only with the simultaneous emission or absorption of a phonon in order to conserve crystal momentum. In the effective mass model, an electron near one of the conduction band maxima can be described (Kohn, 1965) as a particle with negative charge and a mass determined by the local curvature of the band. Similar considerations apply to a hole at one of the maxima in the valence band, assigning it positive charge.

The transverse ( $m_{et}$ ) and longitudinal ( $m_{el}$ ) electron effective masses (Levinger and Frankl, 1961) are given in Table 1, as well as the density of states average ( $m_{de}$ ) and optical average ( $m_{oe}$ ) given by:

$$m_{de}^3 = m_{el} m_{et}^2 \quad (3.2.2)$$

$$3m_{oe}^{-1} = m_{el}^{-1} + 2m_{et}^{-1} \quad (3.2.3)$$

Also listed in Table 1 are the heavy and light hole densities of states masses  $m_{dHh}$ ,  $m_{dLh}$ , obtained by taking the average (Brinkman and Rice, 1972):

$$\frac{m_{hL,H}^{3/2} E^{1/2}}{\sqrt{2} \pi^2 \hbar^3} = \sum_{\underline{k}} \delta[E - E_{\pm}(\underline{k})] \quad (3.2.4)$$

( $E_{\pm}(\underline{k})$  given by equation 3.2.1).

Table 1

Ge band structure parameters and effective masses

<u>Electrons:</u>	$m_{et}$	$m_{el}$	$m_{oe}$	$m_{de}$
	1.58	0.082	0.12	0.022

Holes:

	A	B	C
	13.38	8.48	13.15
	$m_{oHh}$	$m_{oLH}$	$m_{dHh}$
	0.275	0.042	0.347
			$m_{dLh}$
			0.042

Static dielectric constant  $\epsilon_0$ : 15.36

Optical or conductivity average masses were defined originally by Lax and Mavroides in 1955. They found that, for a single band:

$$\frac{n}{m_{ij}(E)} = \frac{1}{4\pi 3\hbar^2} \int \frac{\partial E}{\partial k_1} \frac{\partial E}{\partial k_j} \frac{\partial k}{\partial E} k^2 d\Omega \quad (3.2.5)$$

where  $n$  is the density of particles in the band

$$\frac{1}{m_o} = \frac{1}{3} \left[ \frac{1}{m_{xx}} + \frac{1}{m_{yy}} + \frac{1}{m_{zz}} \right] . \quad (3.2.6)$$

The optical effective masses  $m_{oHh}$  and  $m_{oLh}$  (Murzin, Zayats and Kononenko, 1975) are also listed in Table 1.

An approximation commonly used is to neglect the valence band warping and to define heavy and light hole masses as

$$\frac{1}{m_{hL,H}} = A \pm \sqrt{B^2 + \frac{C^2}{16}} .$$

In this approximation the bands are taken as spherical and there is no difference between optical and density of states masses.

### 3.3 Absorption of Light by Spheres: Mie Theory

The scattering and absorption of electromagnetic radiation by a homogeneous sphere is fully described by classical Mie theory (e.g., see van de Hulst, 1957 or Kerker, 1969). In isotropic media the fields  $\vec{E}$  and  $\vec{H}$  satisfy a vector wave equation

$$\nabla^2 \underline{A} + k^2 \epsilon \underline{A} = 0 \quad (3.3.1)$$

where  $k$  is the wavevector of the radiation and  $\epsilon$  the dielectric constant of the medium. Solutions to the wave equations are

$$\underline{E} = \underline{\nabla} \times (\underline{r}v) + \frac{i}{k\sqrt{\epsilon}} \underline{\nabla} \times \underline{\nabla} \times (\underline{r}u) \quad (3.3.2)$$

$$\underline{H} = \sqrt{\epsilon} (-\underline{\nabla} \times (\underline{r}u)) + \frac{i}{R\sqrt{\epsilon}} \underline{\nabla} \times \underline{\nabla} \times (\underline{r}v) \quad (3.3.3)$$

taking the  $z$  axis along the direction of propagation of the incident wave,  $u$  and  $v$  in spherical coordinates are given by:

a) Outside incident wave: ( $r > R$ : sphere's radius)

$$u = e^{i\omega t} \cos\phi \sum_{n=1}^{\infty} (-i)^n \frac{2n+1}{n(n+1)} p_n^1(\cos\theta) j_n(k_1 r) \sqrt{\epsilon_1} \quad (3.3.4)$$

$$v = e^{i\omega t} \sin\phi \sum_{n=1}^{\infty} (-i)^n \frac{2n+1}{n(n+1)} p_n^1(\cos\theta) j_n(k_1 r) \sqrt{\epsilon_1} \quad (3.3.5)$$

where  $p_n^l$  are Legendre polynomials and  $j_n$  spherical Bessel functions.

b) Outside, scattered wave:  $r > R$

$$u = e^{i\omega t} \cos\phi \sqrt{\epsilon_0} \sum_{n=1}^{\infty} -a_n (-i)^n \frac{2n+1}{n(n+1)} p_n^1(\cos\theta) h_n(k_1 r) \quad (3.3.6)$$

$$v = e^{i\omega t} \sin\phi \sqrt{\epsilon_0} \sum_{n=1}^{\infty} -b_n (-i)^n \frac{2n+1}{n(n+1)} p_n^1(\cos\theta) h_n(k_1 r) \quad (3.3.7)$$

where  $a_n, b_n$ : coefficients to be determined

$h_n$ : spherical Haenkel functions.

c) Inside wave: ( $r < R$ )

$$u = i\omega t \cos\phi \sum_{n=1}^{\infty} \sqrt{\epsilon} c_n (-i)^n \frac{2n+1}{n(n+1)} p_n^1(\cos\theta) j_n(k_2 r) \quad (3.3.8)$$

$$v = i\omega t \sin\phi \sum_{n=1}^{\infty} \sqrt{\epsilon} d_n (-i)^n \frac{2n+1}{n(n+1)} p_n^1(\cos\theta) j_n(k_2 r) \quad (3.39)$$

where  $c_n, d_n$ : undetermined coefficients

$\epsilon_0, k_1$  are the dielectric constant and wave vector in the outside medium and  $\epsilon$  and  $k_1$  inside the drop.

Using the boundary conditions the coefficients  $a_n, b_n, c_n$  and  $d_n$  can be determined; in particular  $a_n$  and  $b_n$  are given by:

$$a_n = \frac{j_n(k_2 R) \frac{\partial}{\partial r} [r j_n(k_1 R)] - j_n(k_1 R) \frac{\partial}{\partial r} [r j_n(k_2 R)]}{h_n(k_1 R) \frac{\partial}{\partial r} [r j_n(k_2 R)] - j_n(k_2 R) \frac{\partial}{\partial r} [r h_n(k_1 R)]} \quad (3.3.10)$$

$$b_n = \frac{\epsilon j_n(k_2 R) \frac{\partial}{\partial r} [r j_n(k_1 R)] - \epsilon_0 j_n(k_1 R) \frac{\partial}{\partial r} [r j_n(k_2 R)]}{\epsilon_0 h_n(k_1 R) \frac{\partial}{\partial r} [r j_n(k_2 R)] - \epsilon_0 j_n(k_2 R) \frac{\partial}{\partial r} [r h_n(k_1 R)]} \quad (3.3.11)$$

The cross section for absorption and scattering by the sphere are obtained as the sum of the contributions from the various multipole orders obtained as functions of these coefficients.

The total, or extinction, cross section is the sum of scattering and absorption contributions:

$$\sigma_{\text{ext}} = \frac{2\pi}{k_1^2} \sum_{n=1}^{\infty} (2n+1) \text{Re}(a_n + b_n) \quad (3.3.12)$$

The scattering cross section is given by:

$$\sigma_{\text{scattering}} = \frac{2\pi}{k_1^2} \sum_{n=1}^{\infty} (2n+1) \{ |a_n|^2 + |b_n|^2 \} . \quad (3.3.13)$$

Electron-hole drops ( $\alpha$  drops) usually have radii of a fraction of a micron to a few microns; for electromagnetic radiation in the far infrared region, the drop radii are small compared to the wavelength both inside and outside the drop; in this case only the lower order terms of the expansion contribute to the cross section. Retaining terms up to second order in  $k_1 R$ , the extinction and scattering cross sections are given by:

$$\begin{aligned} \sigma_{\text{ext}} = & 4\pi k_1 R^3 \left\{ \text{Im} \left[ \frac{\bar{\epsilon}-1}{\bar{\epsilon}+2} + \frac{(k_1 R)^2}{15} \frac{(\bar{\epsilon}-1)^2}{\bar{\epsilon}+2} \frac{\bar{\epsilon}^2 + 27\bar{\epsilon} + 38}{2\bar{\epsilon}+1} \right] \right. \\ & \left. - \frac{2}{3} (k_1 R)^3 \text{Re} \left( \frac{\bar{\epsilon}-1}{\bar{\epsilon}+2} \right)^2 \right\} \end{aligned} \quad (3.3.14)$$

$$\sigma_{\text{scatt}} = 4\pi k_1 R^3 \left| \frac{\bar{\epsilon}-1}{\bar{\epsilon}+2} \right|^2 (k_1 R)^3 \quad (3.3.15)$$

Here  $\bar{\epsilon} = \frac{\epsilon}{\epsilon_0}$  is the dielectric constant relative to the medium. For spheres with radii lower than  $1\mu$  and infrared radiation with wavelength of the order of  $100\mu$  only the term in  $R^3$  contributes to the absorption. In this region (Rayleigh limit) the cross-section of each drop is proportional to its volume and the absorption line shape is independent of the drop size. If  $N$  drops per unit volume contribute to the absorption, the absorption coefficient in the dipole approximation is given by:



$$\alpha(\omega) = N \cdot \sigma(\omega) = 4\pi \frac{\omega}{c} \sqrt{\epsilon_0} NR^3 \text{Im} \left( \frac{\bar{\epsilon} - 1}{\bar{\epsilon} + 2} \right) \quad (3.3.16)$$

( $\epsilon_0$ , the dielectric constant for Ge, is given in table 4.)

### 3.4 The Dynamic Dielectric Function

In order to evaluate the absorption cross section as given in the previous section, the dielectric response function of the metallic drops to the incident radiation must be calculated.

In the general case the dielectric constant of a semiconductor, within the random phase approximation, is given by (Ehrenreich and Cohen, 1959)

$$\epsilon(q, \omega) = \epsilon_0 - \frac{4\pi e^2}{q^2} \sum_{\underline{k}} \sum_{ij} \frac{(f_{\underline{k}}^i - f_{\underline{k}+\underline{q}}^j) (E_{\underline{k}}^i - E_{\underline{k}+\underline{q}}^j)}{(E_{\underline{k}}^i - E_{\underline{k}+\underline{q}}^j)^2 - \omega(\omega + i\gamma)} \left| \rho_{\underline{k}, \underline{k}+\underline{q}}^{ij} \right|^2 \quad (3.4.1)$$

Here the indices  $i, j$  are summed over  $\underline{k}$  states in the different bands;  $\rho_{\underline{q}}^{ij}$  denotes the matrix element of the density operator between the state  $\underline{k}$  in the  $i$ th band and the state  $\underline{k}+\underline{q}$  in the  $j$  band;  $f_{\underline{k}}^i$  and  $f_{\underline{k}+\underline{q}}^j$  are the thermal occupation factors of these states. In this expression  $\gamma$  is an infinitesimal, but it has generally been applied to real problems in which damping processes produce finite width states; for these cases  $\gamma$  is a finite damping constant.

The summation over the bands can be divided into two parts. The intraband part contains those transitions in which

the initial and final states are in different bands.

The  $\underline{q}$  vector of the incoming electromagnetic radiation is very small as compared with the  $\underline{k}$  vectors of the electron and hole states. In this case the contribution of intraband transitions to the dielectric constant is the Drude expression

$$\epsilon_{\text{intra}} = -\epsilon_0 \frac{\omega_p^2}{\omega(\omega+i\gamma)} \quad (3.4.2)$$

$$\omega_p^2 = \omega_{pe}^2 + \omega_{ph}^2 \quad (3.4.3)$$

$$\omega_{pe}^2 = \frac{4\pi e^2}{\epsilon_0} \frac{n_e}{m_{oe}} \quad (3.4.4)$$

$$\omega_{ph}^2 = \frac{4\pi e^2}{\epsilon_0} \left[ \frac{n_H}{m_{oHh}} + \frac{n_L}{m_{oLh}} \right] \quad (3.4.5)$$

$\omega_{pe}$  and  $\omega_{ph}$  are the plasma frequencies for electrons and holes;  $n_e$ ,  $n_H$  and  $n_L$  are the densities of electrons, heavy holes and light holes inside the drop. Charge neutrality determines  $n_e = n_H + n_L$ . Another equation relating  $n_H$  and  $n_L$  can be obtained considering that holes in both bands have the same Fermi energy  $E_{Fh}$

$$E_{Fh} = \frac{\hbar^2}{2m_{dHh}} [3\pi^2 n_H]^{2/3} = \frac{\hbar^2}{2m_{dLh}} [3\pi^2 n_L]^{2/3} \quad (3.4.6)$$

$$\frac{n_L}{n_H} = \left( \frac{m_{dLh}}{m_{dHh}} \right)^{3/2} \equiv \rho^{3/2}$$

With these considerations (3.4.3) can be written as

$$\omega_p^2 = \frac{4\pi e^2}{\epsilon_0} \left[ \frac{1}{m_{oe}} + \frac{1}{m_{OHh}} \frac{1}{1+\rho^{3/2}} + \frac{1}{m_{OLh}} \frac{\rho^{3/2}}{1+\rho^{3/2}} \right] \quad (3.4.7)$$

Vavilov et al (1969), when fitting the first EHD far infrared absorption measurements, considered  $\epsilon_{intra}$  as the only contribution to the dielectric constant and took the Rayleigh limit for the cross section. This choice, for  $\gamma = 0$ , gives a Lorentzian lineshape with a resonance at  $\frac{\omega_p}{\sqrt{3}}$ . The finite value of  $\gamma$  shifts the position of the peak. Considering only intraband terms, the relative dielectric constant is:

$$\bar{\epsilon} = 1 - \frac{\omega_p^2}{\omega(\omega+i\gamma)} \quad (3.4.8)$$

The effect of  $\gamma$  on the peak position can be seen easily expanding  $\bar{\epsilon}$  in powers of  $\frac{\gamma}{\omega}$ . The calculations of  $\gamma(\omega)$  of the next section show that, for every frequency,  $\gamma(\omega)$  is at least one order of magnitude smaller than  $\omega$ . Then second order terms in  $\frac{\gamma}{\omega}$  can be neglected. With this approximation:

$$\bar{\epsilon} = 1 - \frac{\omega_p^2}{\omega^2} + \frac{i\gamma}{\omega} \frac{\omega_p^2}{\omega^2} \quad (3.4.9)$$

The absorption coefficient is obtained replacing (3.4.9) in (3.3.17):

$$\alpha(\omega) \approx \omega \text{Im} \left( \frac{\bar{\epsilon}-1}{\bar{\epsilon}+2} \right) = \frac{3\gamma \omega_p^2}{\omega [(3\omega^2 - \omega_p^2)^2 + \gamma^2 \frac{\omega_p^4}{\omega^2}]} \quad (3.4.10)$$

Eq. (3.4.10) has a maximum for:

$$\omega_0^4 = \frac{\omega_p^4}{9} \left( 1 + 2 \frac{\gamma^2}{\omega_0^2} \right) \quad (3.4.11)$$

Obviously the intraband damping has the effect of shifting the resonant frequency towards higher values than the predicted  $\frac{\omega_p}{\sqrt{3}}$ . Of all the possible interband transitions between the valence or conduction bands in Ge, only transitions between the heavy and light hole bands have energies in the far infrared region.

Fig. 3.2 shows that vertical transitions are possible between two energy limits  $\hbar\omega_1$  and  $\hbar\omega_2$  determined by the Fermi energy of the holes and the structure of the two bands. For each direction of  $k$ ,  $\hbar\omega_1$  and  $\hbar\omega_2$  are given by:

$$\hbar\omega_1(\theta, \phi) = E_{Fh} \left[ 1 - \frac{E_-(\theta, \phi)}{E_+(\theta, \phi)} \right] \quad (3.4.12)$$

$$\hbar\omega_2(\theta, \phi) = E_{Fh} \left( \frac{E_+(\theta, \phi)}{E_-(\theta, \phi)} - 1 \right) \quad (3.4.13)$$

The extremum values of  $\hbar\omega_1$  and  $\hbar\omega_2$  are obtained in the directions (100) and (111). As a function of the Fermi energy:

$$\hbar\omega_{\min} = E_{Fh} \cdot (.776) \quad (3.4.14)$$

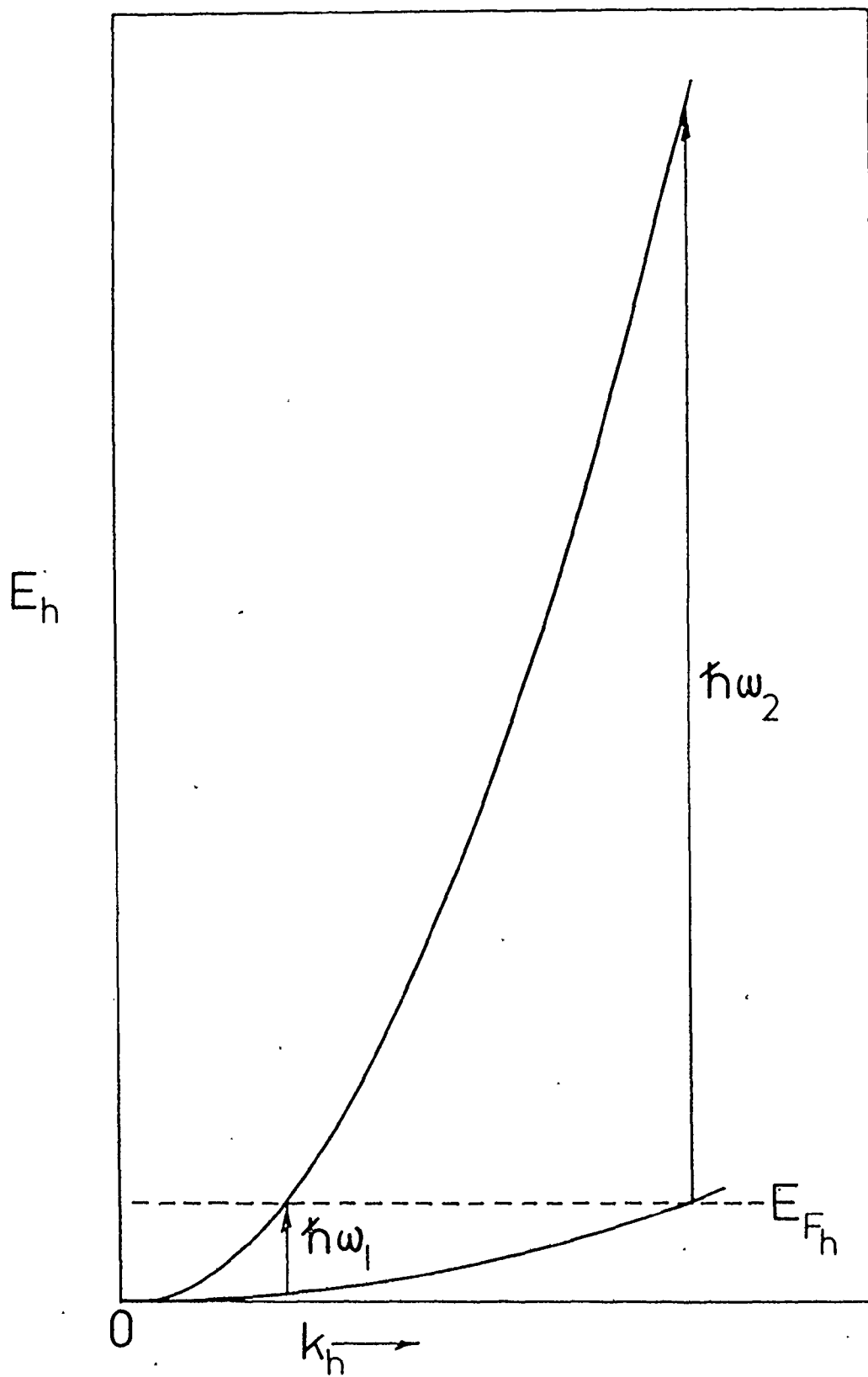
$$\hbar\omega_{\max} = E_{Fh} \cdot (11.39) \quad (3.4.15)$$

The plasma resonance  $\omega_0$  is such that  $\omega_{\min} < \omega_0 < \omega_{\max}$ .

The evaluation of the interband contribution to equation (3.4.1) requires the knowledge of the interband matrix elements. Combescot and Nozières (1972) have calculated them in the spherical approximation obtaining

Fig. 3-2

Heavy and light-hole valence bands in germanium. In EHD the bands are filled to  $E_{Fh}$  and interband transitions can occur only between a threshold  $\hbar\omega_1$  and a cutoff  $\hbar\omega_2$ .



$$\langle \underline{k}, H | \rho_{\underline{q}}^{H,L} | \underline{k} + \underline{q}, L \rangle = \frac{3}{4} \sin^2(\theta_{\underline{k}, \underline{k} + \underline{q}}) \quad (3.4.16)$$

and

$$\langle \underline{k}, H | \rho_{\underline{q}} | \underline{k} + \underline{q}, H \rangle = \langle \underline{k}, L | \rho_{\underline{q}} | \underline{k} + \underline{q}, L \rangle = \frac{1}{4} (1 + 3 \cos^2 \theta) \quad (3.4.17)$$

For small  $\underline{q}$ , (3.4.13) becomes:

$$\lim_{q \rightarrow 0} |\rho_{\underline{q}}^{H,L}| = \frac{3}{4} \frac{q^2}{k^2} \sin^2 \alpha \quad (3.4.18)$$

where  $\alpha$  is the angle between  $\underline{k}$  and  $\underline{q}$ .

Averaging (3.4.18) for all possible  $\alpha$  values, the interband dielectric function is:

$$\epsilon_{\text{inter}} = -4\pi e^2 \frac{2}{(2\pi)^3} \int \frac{[f_1(\underline{k}) - f_2(\underline{k})][E_+(\underline{k}) - E_-(\underline{k})]}{[E_+(\underline{k}) - E_-(\underline{k})]^2 - \omega(\omega + \gamma')} \frac{d^3 k}{k^2} \quad (3.4.19)$$

with  $E_{\pm}$  given by eq. (3.2.1).

Eq. (3.4.19) was evaluated by numerical integration at  $T=0$ , in which case the Fermi distribution functions can be replaced by  $\theta$  functions. Fig. 3.3 shows the real ( $\epsilon_1$ ) and imaginary ( $\epsilon_2$ ) parts of  $\epsilon_{\text{int}}$  obtained using a hole Fermi energy  $E_{\text{Fh}} = 3.5$  meV, and  $\gamma' = 0.001$  meV.

The interband transitions affect the condition for resonance which becomes:

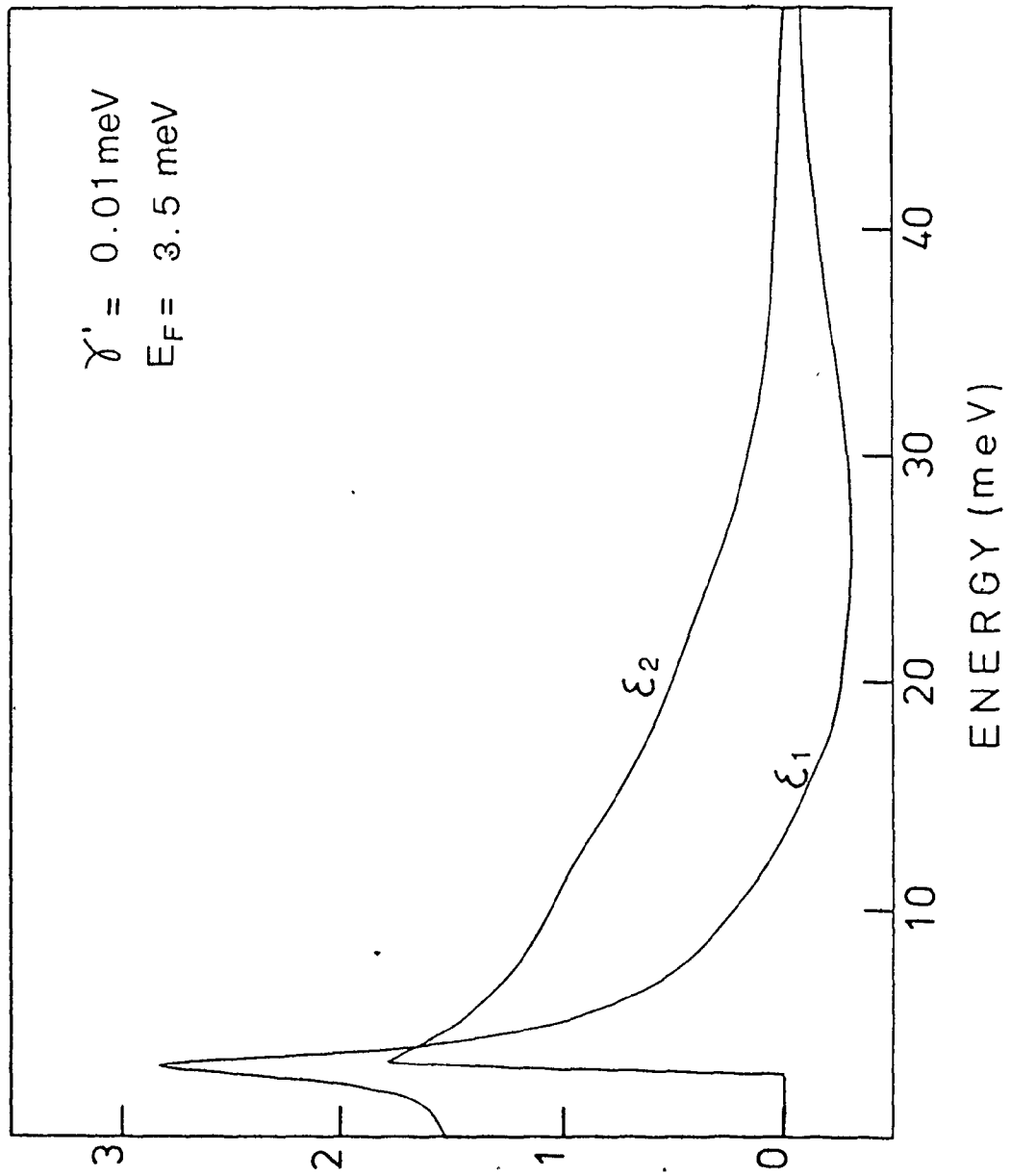
$$\omega_0^2 = \frac{\omega_p^2}{3 + \epsilon_1(\omega_0)} \quad (3.4.20)$$

A positive  $\epsilon_1$  shifts the resonance condition towards lower frequency than that predicted by the Drude value  $\frac{\omega_p}{\sqrt{3}}$ . A larger

Fig. 3-3

Real ( $\epsilon_1$ ) and imaginary ( $\epsilon_2$ ) parts of the interband dielectric constant in units of  $\epsilon_0$ . The interband damping used is very small compared with the Fermi energy. Note the sharp threshold near 3 meV ( $\hbar\omega_1$  in fig. 3-1).





value of  $\gamma'$  would smooth the dielectric function. Fig. 3.4 shows  $\epsilon_1$  and  $\epsilon_2$  for  $\gamma' = 2.5$  meV. It can be seen that for  $\omega \sim 9$  meV (close to the resonance condition)  $\epsilon_1$  is increased by the damping. Interband damping not only contributes to the width of the absorption but affects the resonance condition. If we then use the position of the peak to obtain the plasma frequency and hence the density of the fluid we will find that the result depends on the value of interband damping chosen.

### 3.5 The Frequency Dependent Damping

#### 1) Isotropic bands

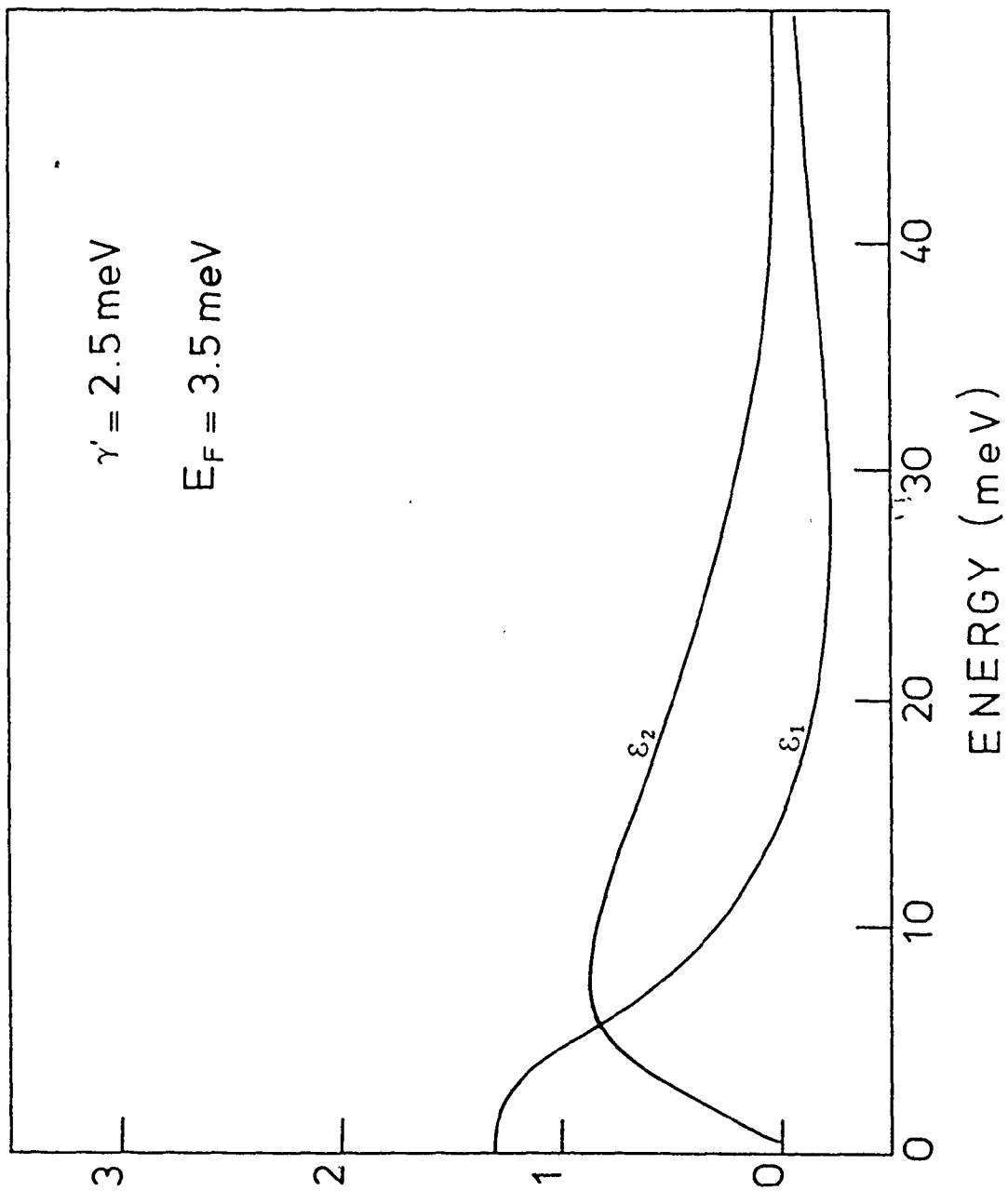
A calculation of the conductivity of an electron-hole plasma was performed by Tzoar and Platzman, (1976) using the temperature dependent Green's function formalism for several  $r_s$  values ( $r_s$ : radius of the volume occupied by a particle in units of the Bohr radius) and electron-hole mass ratios. They started from the general expression of the long wavelength conductivity for a system of charged particles as given by Kubo (1957).

$$\sigma_{\mu\nu}(\omega) = \frac{1}{V} \int_0^{\infty} d\tau e^{i\omega\tau} \int_0^{\beta} d\lambda \langle j_{\mu}(\tau - ih\lambda) j_{\nu}(0) \rangle \quad (3.5.1)$$

where  $\omega$  is the frequency of the electromagnetic wave,  $\underline{j}$  is the current operator in the Heisenberg representation and  $\beta$  the inverse of the temperature in energy units. Integrating eq. (3.5.1) by parts they obtained:

Fig. 3-4

Real ( $\epsilon_1$ ) and imaginary ( $\epsilon_2$ ) parts of the interband dielectric constant for damping comparable with the hole Fermi energy. Considerable broadening appears and the threshold is erased. The values are given in units of  $\epsilon_0$ .



$$\sigma_{\mu\nu}(\omega) = \sigma_{\mu\nu}^{(0)}(\omega) + \sigma_{\mu\nu}^{(1)}(\omega) \quad (3.5.2)$$

$$\sigma_{\mu\nu}^{(0)}(\omega) = -\frac{1}{i\omega V} \int_0^{\beta} d\lambda \langle j_{\mu}(-i\hbar\lambda) j_{\nu}(0) \rangle \quad (3.5.3)$$

Calculation of (3.5.3) yields:

$$\begin{aligned} \sigma_{\mu\nu}^{(0)}(\omega) &= i\sigma_0(\omega) \delta_{\mu\nu} = i \frac{1}{4\pi\omega} \left( \sum_s 4\pi^2 \frac{n_s}{m_s} \right) \delta_{\mu\nu} = \\ &= i \frac{1}{4\pi\omega} \omega_p^2 \delta_{\mu\nu} \end{aligned} \quad (3.5.4)$$

and

$$\sigma_{\mu\nu}^{(1)}(\omega) = \frac{1}{\hbar\omega} \frac{1}{V} \int_0^{\infty} d\tau e^{i\omega\tau} \langle [j_{\mu}(\tau), j_{\nu}(0)] \rangle. \quad (3.5.5)$$

For a cubic crystal  $\sigma_{\mu\nu}$  reduces to a scalar, then:

$$\sigma(\omega) = i\sigma_0(\omega) + \sigma_1(\omega) \quad (3.5.6)$$

$\sigma(\omega)$  can be obtained in terms of the resistivity of the system

$$R = \text{Re}\left(\frac{1}{\sigma}\right) = \frac{\sigma_1}{\sigma_0^2} \text{ for real } \sigma_1.$$

Then

$$\sigma(\omega) = i \frac{\omega_p^2}{4\pi\omega} + R \left( \frac{\omega_p^2}{4\pi\omega} \right)^2$$

and the effective dielectric constant of the system:

$$\epsilon = 1 - \frac{4\pi}{i\omega} \sigma(\omega) = 1 - \frac{\omega_p^2}{\omega^2} + i \frac{\omega_p^4}{4\pi\omega^3} R \quad (3.5.7)$$

Comparing (3.5.7) with (3.4.9), we have the usual relation between damping and resistivity:

$$\gamma = \frac{\omega_p^2 R}{4\pi} \quad (3.5.8)$$

For a medium with static dielectric constant  $\epsilon_0$  these equations are generalized to:

$$\bar{\epsilon} = \frac{\epsilon}{\epsilon_0} = 1 - \frac{\omega_p^2}{\omega^2} + i\epsilon_0 \frac{\omega_p^4}{4\pi\omega^3} R \quad (3.5.9)$$

and

$$= \frac{\omega_p^2 R \epsilon_0}{4\pi} \quad (3.5.10)$$

Tzoar and Platzman found that both at very low and at very high frequencies  $\sigma^{(1)}$  can be dealt with using the static approximation. Electrons and holes interact via a statically screened Coulomb potential. The calculations presented in this section are all performed within this approximation.

$$R = \frac{C}{\omega} \int \frac{dq}{\epsilon_q^2} \int_0^\omega dx \operatorname{Im} B_q(x) \operatorname{Im} Q_q(\omega-x) \quad (3.5.11)$$

where  $B_q$  and  $Q_q$  are the polarization functions for free holes and electrons respectively.

For free electrons (Lindhard, 1954):

$$\operatorname{Im} Q_q(x) = \frac{2m_e}{\hbar^2} \frac{1}{16\pi q} \begin{cases} \frac{2m_e}{\hbar^2} x & \text{for } q < k_F \text{ and } \frac{2m_e}{\hbar^2} x \geq 2k_F q - q^2 \\ k_F^2 - \left(\frac{2m_e}{\hbar^2} x - q^2\right)^2 \frac{1}{4q^2} & \text{for } \left|2k_F q - q^2\right| < \frac{2m_e}{\hbar^2} x \leq 2k_F q + q^2 \\ 0 & \text{otherwise} \end{cases} \quad (3.5.12)$$

The expression for  $\operatorname{Im} B_q(x)$  is the same replacing  $m_h$  (hole mass) for  $m_e$  (electron mass);  $q$  and  $x$  are the transfer of momentum.

and energy respectively and  $\epsilon_q$  is the Lindhard static dielectric function:

$$\epsilon_q = 1 + \frac{4\pi e^2}{q^2 \epsilon_0} (Q_q(0) + B_q(0)) \quad (3.5.13)$$

$$Q_q(0) = \frac{2m_e}{\hbar^2} \frac{k_F}{4\pi^2} \left[ 1 + \frac{(k_F^2 - q^2)}{q k_F} \ln \left| \frac{2k_F + q}{2k_F - q} \right| \right] \quad (3.5.14)$$

and similarly for  $B_q(0)$ .

The constant at the front of (3.5.11) is:

$$C = \frac{32\pi^2 \left( \frac{1}{m_e} + \frac{1}{m_h} \right)}{3(\omega_{pe}^2 + \omega_{ph}^2)^2} \quad (3.5.15)$$

where  $\omega_{pe}$  and  $\omega_{ph}$  are the plasma frequencies for electrons and holes.

In this thesis I present an application and generalization of these equations to the case of EHD in Ge using different approximations. I will treat the heavy and light hole bands as parabolic with density of states effective masses as given in Table 1; the optical effective masses are employed in the calculation of  $C$ . The spatial degeneracy is taken into account by considering the electron Fermi wavevector  $k_{Fe}$  as  $\frac{k_{Fh}}{4^{1/3}}$ , where  $k_{Fh}$  is the Fermi wavevector for the holes; in the Tzoar and Platzman calculations,  $k_{Fe} = k_{Fh}$  since no band structure effects are considered and  $\epsilon_0 = 1$ .

In the simplest approximation, the splitting of the valence band is neglected and the holes are considered to have an

average effective mass: )

$$m_{dh} = [m_{dHh}^{3/2} + m_{dLh}^{3/2}]^{2/3} . \quad (3.5.16)$$

In this approximation the equivalent to eq. (3.5.12) for  $\text{Im } B_{\vec{q}}(x)$  is valid. The results of eqs. (3.5.10) to (3.5.15) for  $E_{Fh} = 3.5$  meV obtained by numerical calculations are shown in figure 3.5 (dashed line).

## 2) Band structure effects

Equation (3.5.1) has to be generalized when the effect of anisotropy of the conduction band is taken into account. The polarization functions  $B$  and  $Q$  depend now on the wavevector  $\vec{q}$ , not only on its absolute value. The corresponding expression is:

$$R = \frac{C}{4\pi\omega} \int \frac{d^3q}{q^2 \epsilon_q^2} \int_0^\omega dx \text{Im } B_{\vec{q}}(x) \text{Im } Q_{\vec{q}}(\omega-x) \quad (3.5.17)$$

The polarization function for an ellipsoidal band can be obtained directly from the spherical case with the aid of the coordinate transformation:

$$q'_x = q_x , \quad q'_y = q_y , \quad q'_z = \sqrt{\rho} q_z \quad \text{with } \rho = \frac{m_{et}}{m_{el}}$$

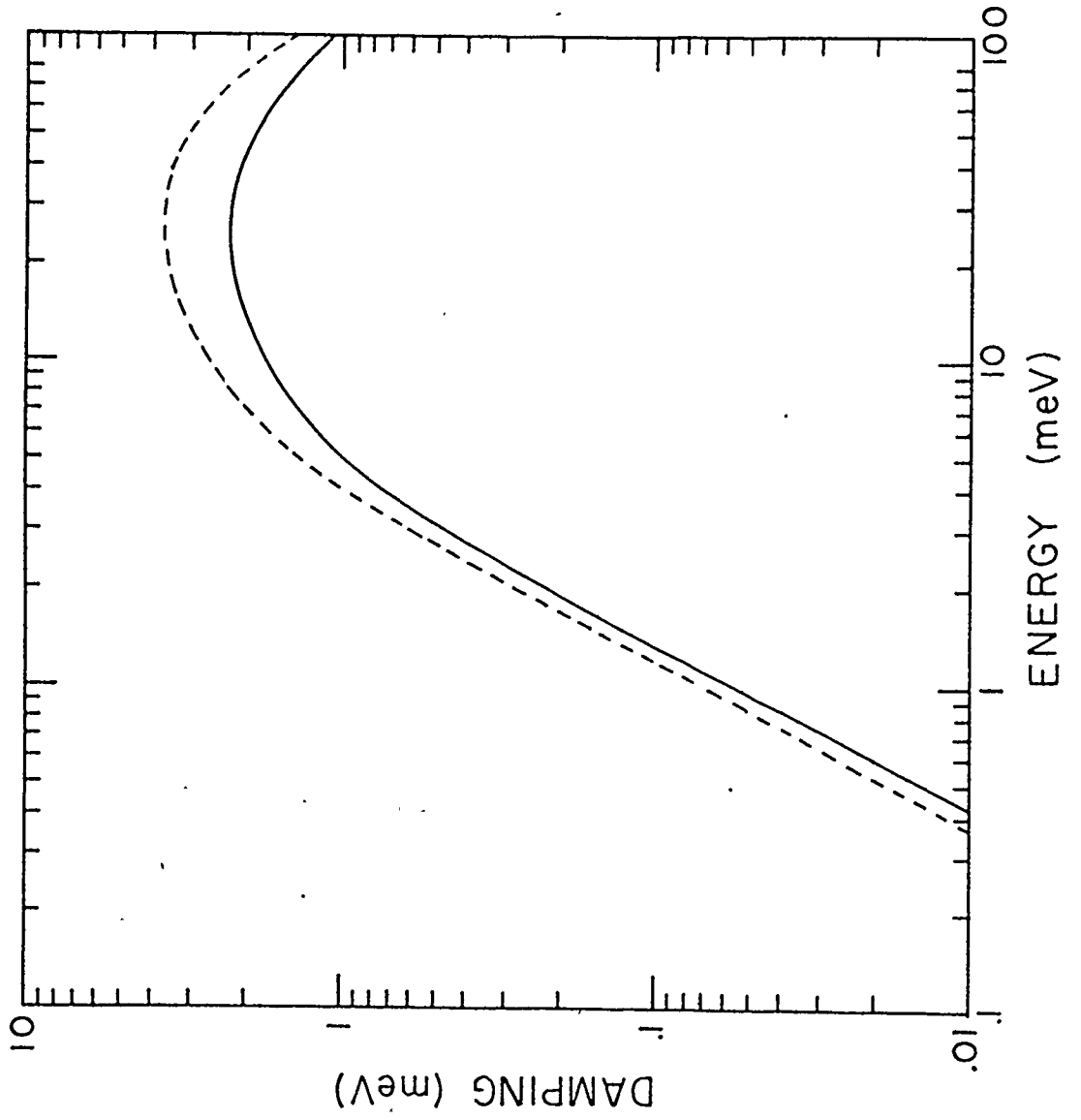
We have then:

$$\begin{aligned} Q_{\text{ellip}}(q, x) &= \frac{1}{\sqrt{\rho}} Q(q'x) \\ q'^2 &= q_x^2 + q_y^2 + \rho q_z^2 \\ k'_{Fe} &= \rho^{1/2} k_{Fe} \end{aligned} \quad (3.5.18)$$



Fig. 3-5

Frequency-dependent damping produced by electron-hole scattering in Ge. The dashed line has been calculated assuming isotropic conduction and valence bands with effective masses  $0.22 m$  and  $0.347 m$ , respectively. The solid line has been obtained considering the anisotropy of the conduction band.



With these considerations we can integrate (3.5.17) in cylindrical coordinates. After computation, the solid curve in fig. 3.5 is obtained. As can be seen, the overall result is a reduction of the damping in the frequency region considered of around 30%.

The inclusion of the valence band structure is much more complicated, even when both light and heavy hole bands are taken as isotropic. The hole bands are coupled by the Coulomb interaction, and matrix elements of the density operator  $\rho_q(k_i, k_j)$  need to be considered. In general  $\text{Im} B_q(x)$  has the form (Ehrenreich and Cohen, 1959):

$$\begin{aligned} \text{Im} B_q(x) = & \int \frac{d^3k}{(2\pi)^3} \langle \underline{k}_i | \rho_q | \underline{k} + \underline{q}_j \rangle \left\{ \delta \left( x - \frac{\hbar^2}{2} \left( \frac{(\underline{k} + \underline{q})^2}{m_i} - \frac{k^2}{m_j} \right) \right) + \right. \\ & \left. + \delta \left( x + \frac{\hbar^2}{2} \left( \frac{k^2}{m_i} - \frac{(\underline{k} + \underline{q})^2}{m_j} \right) \right) \right\} \end{aligned} \quad (3.5.19)$$

with the integration limits:

$$\begin{aligned} \frac{\hbar^2 |\underline{k} + \underline{q}|^2}{2m_i} &> E_F \\ \frac{\hbar^2 k^2}{2m_j} &< E_F . \end{aligned}$$

Two kinds of contributions will occur: when an electron interacts with a hole, the hole can either go to an empty state in its own band (intraband transitions) or jump from the heavy hole band to the light hole band that is nearly empty (interband transition). The matrix elements are given by eq. (3.4.18) and (3.4.19).

a) Interband

In units of  $\frac{\hbar^2}{2m} = 1$  the imaginary part of the polarization function is:

$$\text{Im } B_{\text{inter}}(\underline{q}, x) = \int \frac{d^3 \underline{k}}{(2\pi)^3} \pi \left\{ \delta \left( x - \left[ \frac{(\underline{k}+\underline{q})^2}{m_{\text{Lh}}} - \frac{k^2}{m_{\text{Hh}}} \right] \right) + \delta \left( x + \frac{k^2}{m_{\text{Hh}}} - \frac{(\underline{k}+\underline{q})^2}{m_{\text{Lh}}} \right) \right\} \times \\ \times \frac{3}{4} \sin^2 \beta \quad (3.5.20)$$

with the integration limits: .

$$|\underline{k}+\underline{q}| > k_{\text{F}2} = (E_{\text{Fh}} m_{\text{Lh}})^{1/2}$$

$$k < k_{\text{F}1} = (E_{\text{Fh}} m_{\text{Hh}})^{1/2}$$

$m_{\text{Lh}}$  and  $m_{\text{Hh}}$  in units of the electron mass  $m$  and  $\beta$  is the angle between  $\underline{k}$  and  $\underline{k}+\underline{q}$ .

For  $x > 0$ , the second  $\delta$  function in eq. (3.5.20) does not contribute to the polarization. Writing it in spherical coordinates we have:

$$\text{Im } B_{\text{inter}}(\underline{q}, x) = \frac{1}{4\pi} \int k^2 dk \int_{-1}^1 d\mu \delta \left( x - \frac{k^2 + 2kq\mu + q^2}{m_{\text{Lh}}} + \frac{k^2}{m_{\text{Hh}}} \right) \frac{3}{4} \frac{q^2 (1-\mu)^2}{k^2 + 2kq\mu + q^2} \times \\ \times \theta \left( (k^2 + 2kq\mu + q^2)^{1/2} - k_{\text{F}2} \right) \theta \left( k_{\text{F}1} - k \right) \quad (3.5.21)$$

where  $\mu = \cos \alpha$  ( $\alpha$  angle between  $\underline{k}$  and  $\underline{q}$ )

and  $\theta$  denotes the step function.

From  $\delta$  and  $\theta$  functions, we find that the integral is different from zero only if:

$$\left| - \frac{q + (x m_{\text{Lh}} (1-R) + R q^2)^{1/2}}{(1-R)} \right| \leq k \leq \frac{q + (x m_{\text{Lh}} (1-R) + R q^2)^{1/2}}{(1-R)} \quad (3.5.22)$$

and

$$(k_{F1}^2 - m_{Hh}x)^{1/2} < k < k_{F1}$$

$$R = \frac{m_{Lh}}{m_{Hh}} .$$

This equation determines the integration limits for  $k$ ; the result of the integration in  $\mu$  is

$$\begin{aligned} \text{Im } B_{\text{inter}}(q, x) &= \frac{3}{128\pi} \frac{m_{Lh}}{q} \int_{k_a}^{k_b} \frac{dk}{k} \frac{4k^2q^2 - [m_{Lh}x - (1-R)k^2 - q^2]^2}{[m_{Lh}x + k^2R]^2} \\ \text{Im } B_{\text{inter}}(q, x) &= -\frac{3}{128\pi q} \frac{m_{Lh}}{q} \left\{ -\frac{(m_{Lh}x + q^2R)^2}{2m_{Lh}xR^2} [\ln(m_{Lh} + k^2R)]_{k_a}^{k_b} + \right. \\ &\quad \left. + \frac{(m_{Lh}x - q^2)^2}{m_{Lh}x} [\ln k]_{k_a}^{k_b} + \frac{(1-R)^2}{2R^2} [k^{2R+m_{Lh}x}]_{k_a}^{k_b} \right\} \end{aligned} \quad (3.5.23)$$

$k_a$  and  $k_b$  are obtained using equation (3.5.22); different integration regions are determined by the value of the wavevector  $q$ ; as we can see in figure 3.6 a, b and c for  $q < (k_{F1} - k_{F2})$ ,  $k_{F1} - k_{F2} < q < k_{F1} + k_{F2}$  and  $q > k_{F1} + k_{F2}$  respectively.

The intersections between the four inequalities of eq. (3.5.22) determine the points  $E_1$ ,  $E_2$ ,  $F_1$  and  $F_2$ ; they are given by:

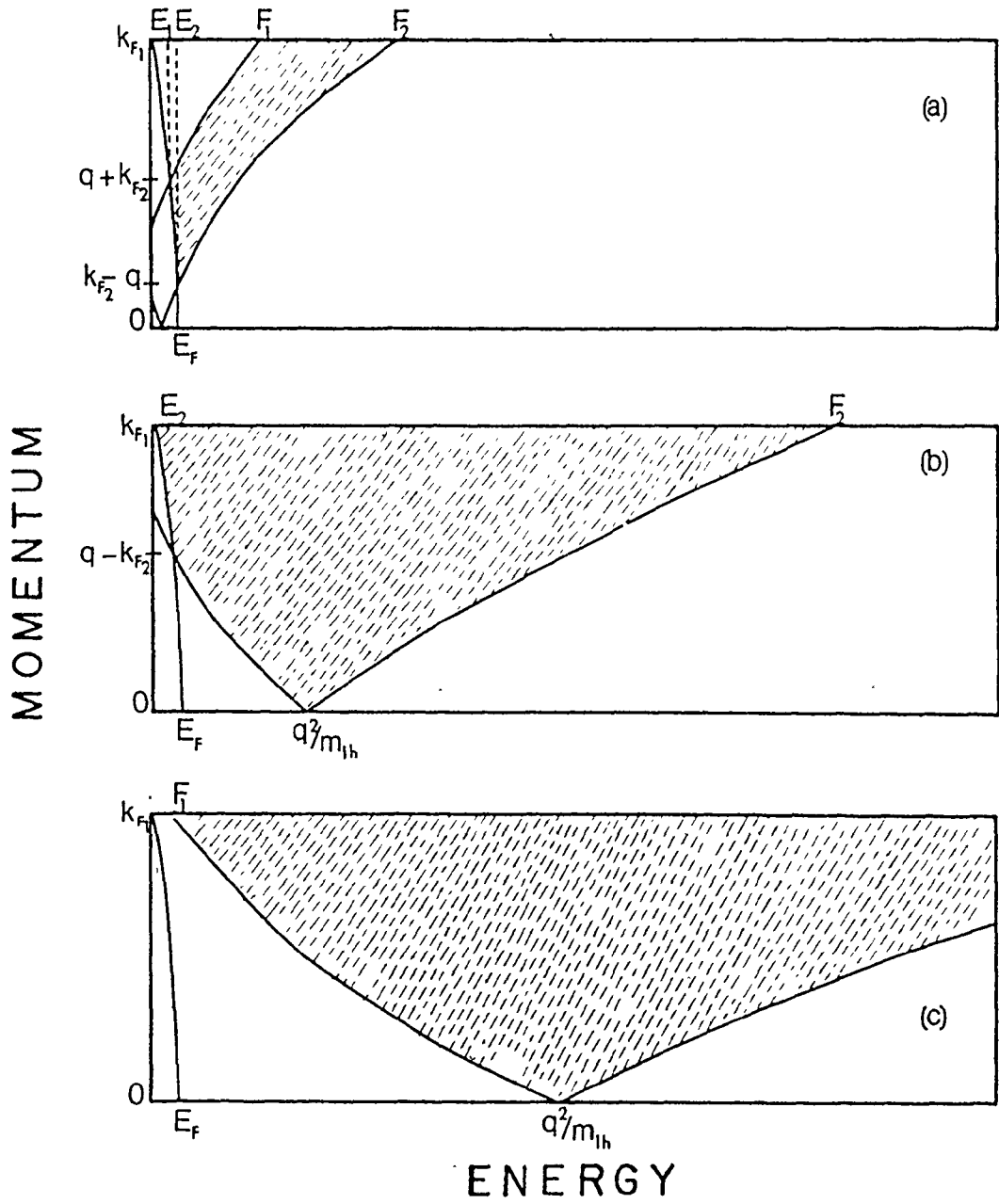
$$E_{1,2} = \frac{1}{m_{Lh}} [k_{F2}^2 (1-R) - Rq^2 \mp 2k_{F2}qR] \quad (3.5.24)$$

$$F_{1,2} = \frac{1}{m_{Lh}} [k_{F1}^2 (1-R) + q^2 \mp 2k_{F1}q]$$

Calculating (3.5.23) in the regions shown in fig. (3-6.a) we have,

Fig. 3-6

Integration regions for the hole interband polarization function in Ge. (a) for  $q < k_{F1} - k_{F2}$  (the figure corresponds to  $q = 0.18 k_{F1}$ ); (b) for  $k_{F1} - k_{F2} < q < k_{F1} + k_{F2}$  ( $q = 0.91 k_{F1}$ ); (c) for  $q > k_{F1} + k_{F2}$  ( $q = 1.45 k_{F1}$ ). The quantities  $k_{F1}$  and  $k_{F2}$  are the Fermi momenta of the heavy- and light-hole bands, respectively and  $q$  is the momentum transfer of the hole.



for  $q < k_{F1} - k_{F2}$ .

$$\text{Im } B_{\text{inter}}(q, x) = \begin{cases} 0 & \text{for } x \leq E_1 \\ I_1(q, x) & \text{for } E_1 \leq x \leq E_2 \\ I_2(q, x) & \text{for } E_2 \leq x \leq F_1 \\ I_3(q, x) & \text{for } F_1 \leq x \leq F_2 \\ 0 & \text{for } x \geq F_2 \end{cases} \quad (3.5.25)$$

From fig. (3-6.b):

For  $k_{F1} - k_{F2} < q < k_{F1} + k_{F2}$

$$\text{Im } B_{\text{inter}}(q, x) = \begin{cases} I_4(q, x) & \text{for } x \leq E_2 \\ I_3(q, x) & \text{for } E_2 \leq x \leq F_2 \\ 0 & \text{for } x \geq F_2 \end{cases} \quad (3.5.26)$$

From fig. (3-6.c)

For  $q > k_{F1} + k_{F2}$

$$\text{Im } B_{\text{inter}}(q, x) = \begin{cases} 0 & \text{for } x \leq F_1 \\ I_3(q, x) & \text{for } F_1 < x \leq F_2 \\ 0 & \text{for } x \geq F_2 \end{cases} \quad (3.5.27)$$

with

$$\begin{aligned} I_1(q, x) &= \frac{3}{128\pi q} m_{Lh} x \\ &\times \left\{ -\frac{m_{Lh} x + q^2 R}{2m_{Lh} x R^2} \ln \left[ \frac{(x m_{Lh} + R q^2) (1-R) + 2qR (m_{Lh} x (1-R) + R q^2)^{1/2}}{k_{F2}^2 (1-R)^2} \right] + \right. \\ &+ \frac{1}{2R} \left[ (q + (q + (m_{Lh} x (1-R) + R q^2)^{1/2})^2) - (k_{F1}^2 - m_{Hh} x) (1-R)^2 \right] \\ &\left. + \frac{m_{Lh} x - q^2}{m_{Lh} x} \ln \left[ \frac{q + (m_{Lh} x (1-R) + R q^2)^{1/2}}{[k_{F1}^2 - m_{Hh} x]^{1/2} (1-R)} \right] \right\} \quad (3.5.28) \end{aligned}$$



$$\begin{aligned}
I_2(q, x) = & -\frac{3}{128\pi q} m_{Lh} \times \\
& \times \left\{ -\frac{(m_{Lh}x+q^2R)^2}{2m_{Lh}xR^2} \ln \left[ \frac{m_{Lh}x(1-R)^2 + R[q+(m_{Lh}x(1-R)+Rq^2)^{1/2}]}{m_{Lh}x(1-R)^2 + R[-q+(m_{Lh}x(1-R)+Rq^2)^{1/2}]} \right] \right. \\
& + \frac{(m_{Lh}x-q^2)^2}{m_{Lh}x} \ln \left[ \frac{q+(m_{Lh}x(1-R)+Rq^2)^{1/2}}{|-q+(m_{Lh}x(1-R)+Rq^2)^{1/2}|} \right] + \\
& \left. + \frac{2}{R} q(m_{Lh}x(1-R)+Rq^2)^{1/2} \right\} \quad (3.5.29)
\end{aligned}$$

$$\begin{aligned}
I_3(q, x) = & -\frac{3}{128\pi q} m_{Lh} \times \\
& \times \left\{ -\frac{(m_{Lh}x+q^2R)^2}{2m_{Lh}xR^2} \ln \left[ \frac{(m_{Lh}x+k_{F1}^2)(1-R)^2}{m_{Lh}x(1-R)^2 + R[-q+(m_{Lh}x(1-R)+Rq^2)^{1/2}]} \right] \right. \\
& + \frac{(m_{Lh}x-q^2)^2}{m_{Lh}x} \ln \left[ \frac{k_{F1}(1-R)}{|-q+(m_{Lh}x(1-R)+Rq^2)^{1/2}|} \right] + \\
& \left. + \frac{1}{2R} [k_{F1}^2(1-R)^2 - (-q+(m_{Lh}x(1-R)+Rq^2)^{1/2})^2] \right\} \quad (3.5.30)
\end{aligned}$$

$$\begin{aligned}
I_4(q, x) = & -\frac{3}{128\pi q} m_{Lh} \times \\
& \times \left\{ -\frac{(m_{Lh}x+q^2R)^2}{2m_{Lh}xR^2} \ln \left( 1 + \frac{x}{E_{Fh}} \right) - \frac{(m_{Lh}x-q^2)^2}{2m_{Lh}x} \ln \left( 1 + \frac{1}{E_{Fh}} \right) \right. \\
& \left. + \frac{(1-R)^2}{2R} m_{Hh}x \right\} \quad (3.5.31)
\end{aligned}$$

In the limit of  $q \rightarrow 0$ ,  $\text{Im } B_{\text{inter}}(0, x)$  gives the known dependence in  $x^{-1/2}$  as obtained by Sherrington and Kohn (1968)

$$\text{Im } B_{\text{inter}}(0, x) = \begin{cases} \frac{q^2}{8\pi} \left( \frac{m_{\text{Lh}}}{(1-R)x} \right)^{1/2} & \text{for } E_{\text{Fh}}(1-R) \leq x \leq \frac{E_{\text{Fh}}}{R} (1-R) \\ 0 & \text{otherwise} \end{cases} \quad (3.5.32)$$

The contribution to the damping of the interaction of an electron with a hole that jumps from the heavy hole to the light hole band is obtained from eq. (3.5.11) with  $\text{Im } B_{\text{inter}}$  as given by eqs. (3.5.25) to (3.5.31). The result of the numerical integration is shown in Fig. 3-7 (dotted line).

b) Intraband

The imaginary part of the intraband polarization function is given by eq. (3.5.21) with  $i = j$  and the matrix element of eq. (3.4.18). In this case  $m$  stands for  $m_{\text{Hh}}$  or  $m_{\text{Lh}}$  and  $k_{\text{F}}$  for  $k_{\text{F1}}$  or  $k_{\text{F2}}$  depending on which contribution is going to be calculated (heavy hole or light hole). After considerable calculations similar to the ones used for the interband contribution, an algebraic expression for  $B_{\text{intra}}(q, x)$  is obtained:

$$\begin{aligned}
 \text{Im } B_{\text{intra}}(q, x) = & \left\{ \begin{array}{l}
 \text{For } q < 2k_F \quad \text{and} \quad x < \frac{1}{m} (-q^2 + 2qk_F) \\
 = \frac{m}{16\pi q} xm - \frac{3m}{128\pi q} \left[ \frac{(mx+q^2)^2}{2mx} \ln \left( 1 + \frac{x}{E_F} \right) + \right. \\
 \quad \left. + \frac{(mx-q^2)^2}{2mx} \ln \left( 1 - \frac{x}{E_F} \right) \right] \\
 \text{For } \frac{1}{m} |-q^2 + 2qk_F| < x < \frac{1}{m} (q^2 + 2qk_F) \\
 = \frac{m}{16\pi q} \left( k_F^2 - \frac{(mx-q^2)}{4q^2} \right) + \\
 + \frac{3}{128\pi q} \left\{ - \frac{(q^2+mx)^2}{2mx} \ln \frac{4q^2(mx+k_F^2)}{(mx+q^2)^2} + \frac{(mx-q^2)}{2mx} \ln \frac{2qk_F}{|mx-q^2|} \right\} \\
 = 0 \quad \text{otherwise}
 \end{array} \right. \quad (3.5.33)
 \end{aligned}$$

The result of computing the resistivity from eq. (3.5.1) with (3.5.33) for  $\text{Im } B(q, x)$  and the usual free electron value given by (3.5.12) for  $\text{Im } Q(q, x)$  is shown in fig. 3-7. The full line corresponds to heavy holes and the broken line to light holes. It can be seen that the contribution to the damping coming from holes that have initial and final states within the heavy hole band is by far the most important. The light hole intraband and the interband contribute only a few percent to the total.

The correct damping is obtained considering the combined effect of valence band splitting and conduction band anisotropy. The value obtained by adding heavy hole, light hole and interband contributions is corrected for the anisotropy of the electron band as in figure 3-5.

Fig. 3-7

Frequency-dependent damping calculated considering the effect of the degeneracy of the valence band but taking the conduction band as isotropic. The solid line gives the contribution to the damping produced by electrons interacting with heavy holes and the dotted line with light holes. The dashed line corresponds to the interaction of electrons with holes in the heavy-hole band that jump to empty states in the light-hole band.

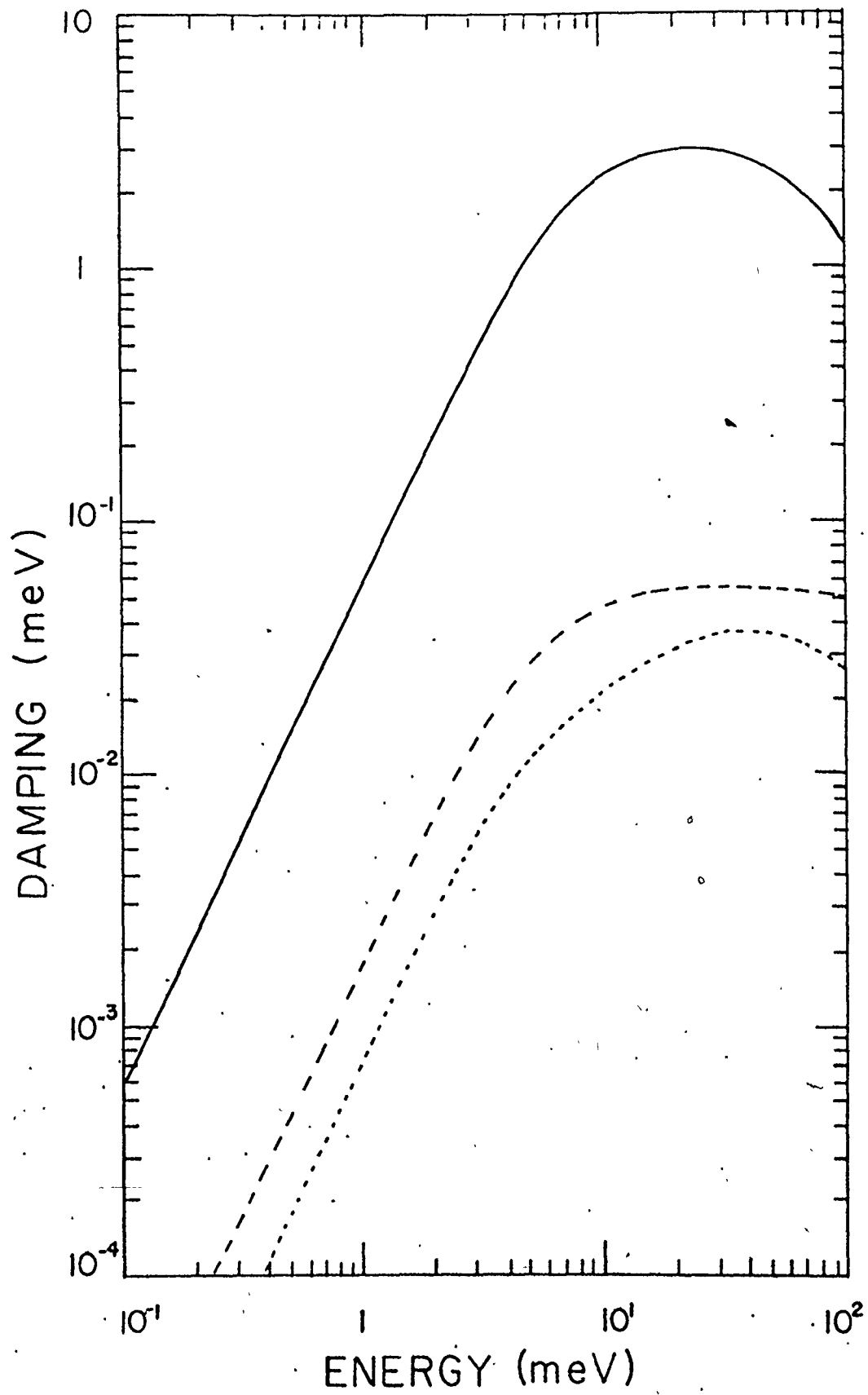


Figure 3-8 shows the final results for the electron-hole damping in the static approximation. It can be seen that it first rises quadratically, reaches a maximum value of 1.9 meV at around 20 meV and then decreases very slowly. For energies below or about 3 meV the damping is at least one order of magnitude smaller than its maximum value. This very small damping at low energies makes possible the existence of a threshold in the EHD absorption, produced by the onset of interband transitions. In contrast the  $r_s = 1$ ,  $\alpha = \frac{m_h}{m_e} = 3$  case calculated by Tzoar and Platzman predicts too high a damping in this region, completely washing out any sharp onset (at 2 meV, their value is 0.9 meV as compared with that calculated here, 0.185 meV). The value at the maximum is questionable since dynamic correlations were neglected in this calculation and they are important in the frequency region where the maximum appears (Tzoar and Platzman, 1976). This fact and its effect in the EHD absorption are discussed in section 3.6 below.

In chapter 6 the calculations for frequencies below 10 meV are compared with experimental values for the damping obtained using different experimental techniques.

### 3.6 Experimental Results

Figures 3-9, 3-10 and 3-11 show the measured absorption spectrum of EHD in pure Ge immersed in a He bath temperature of 1.2°K. In figure 3-9 the region of 2.5 meV to 30 meV is shown. The vertical scale is  $\ln \frac{I_0}{I}$  where  $I_0$  is the signal

Fig. 3-8

Overall electron-hole damping in Ge as a function of frequency. The line has been calculated considering the effects of anisotropy of the conduction band and splitting of the valence band.

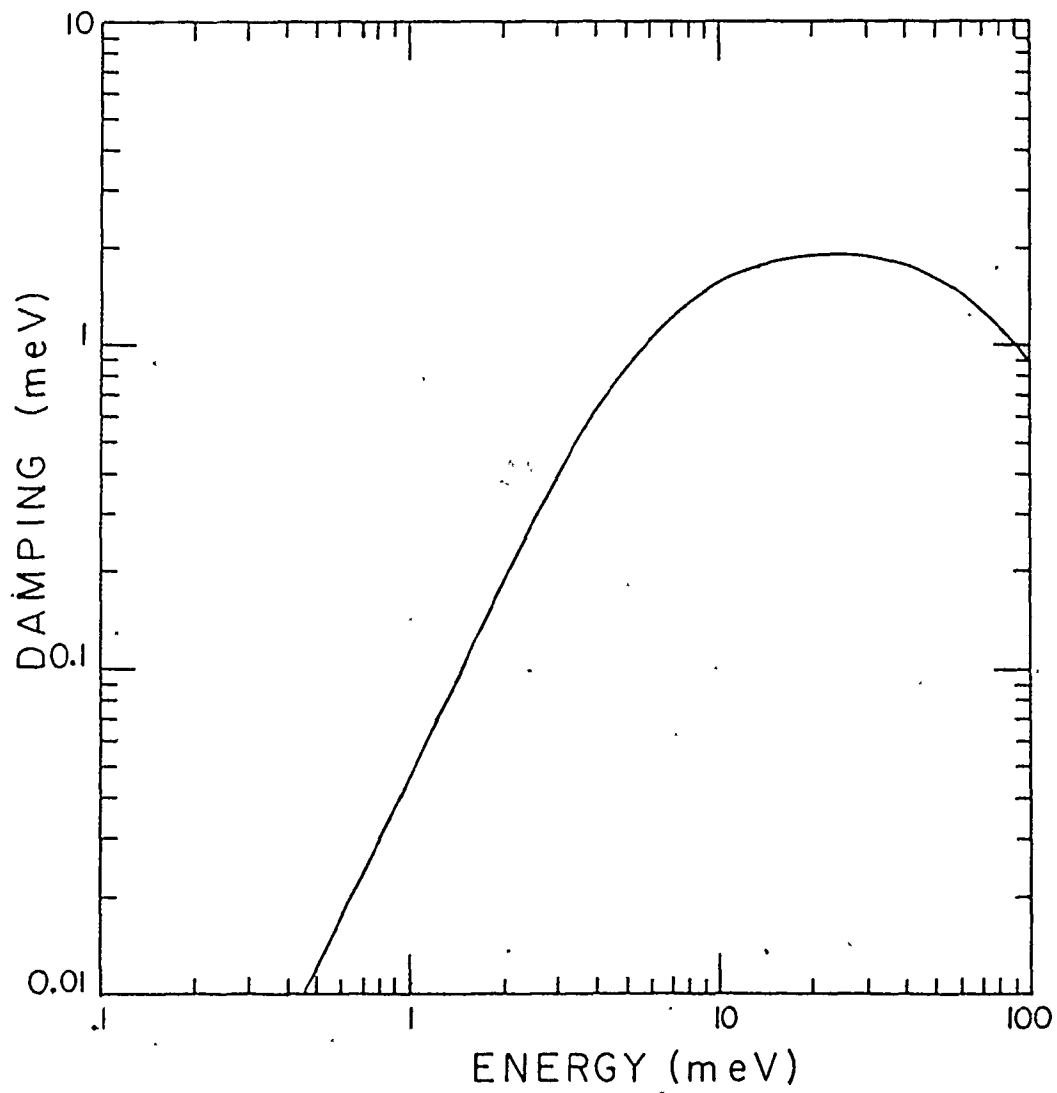




Fig. 3-9

Absorption spectrum of EHD at 1.2°K from 2.5 to 30 meV.

A resonant peak occurs at 9.3 meV near  $1/\sqrt{3}$  of the plasma frequency.

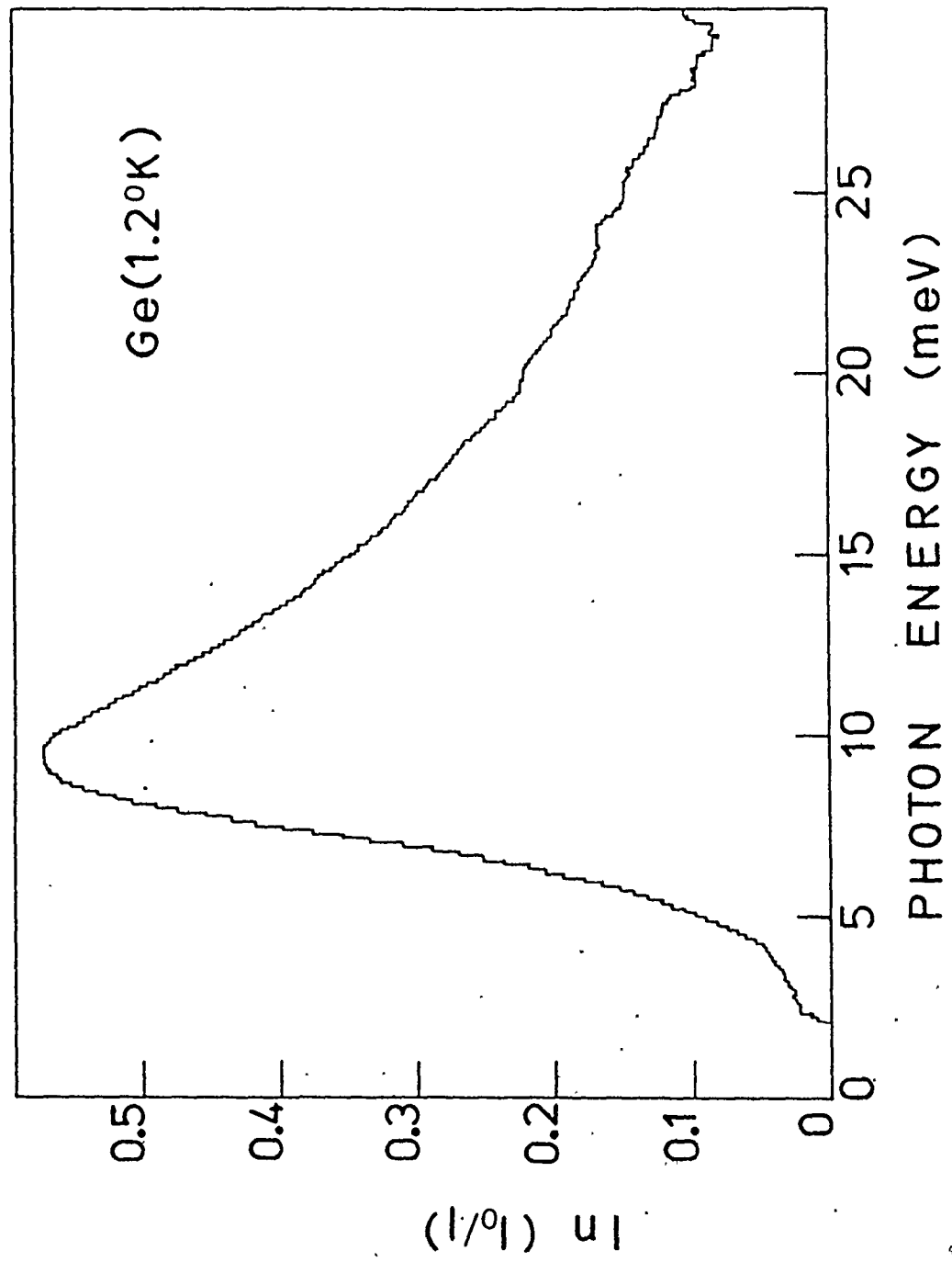


Fig. 3-10

The low energy region of the absorption spectrum of EHD at 1.2°K. A clear threshold can be seen at 2.8 meV that is identified with the onset of interband transitions.

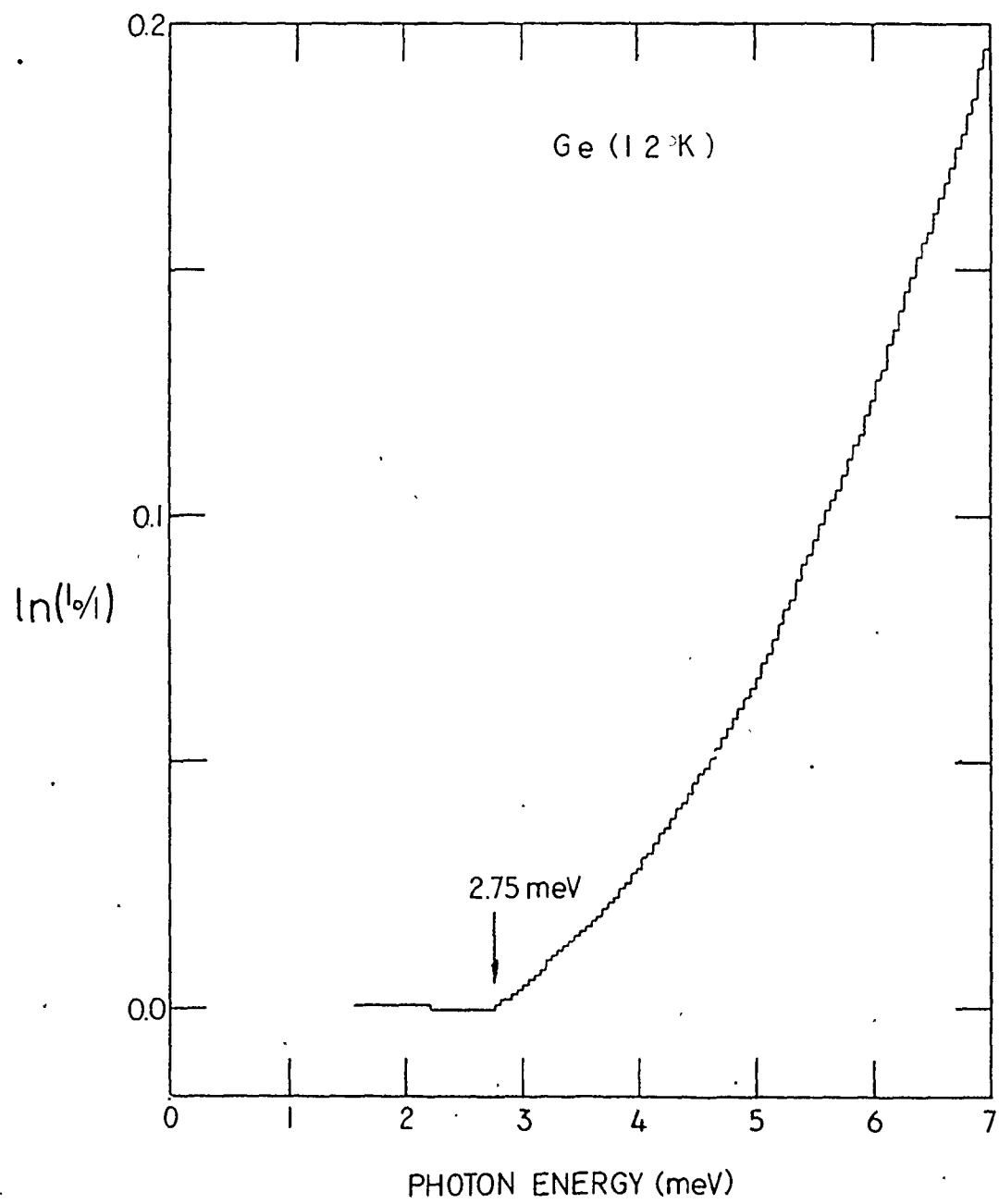
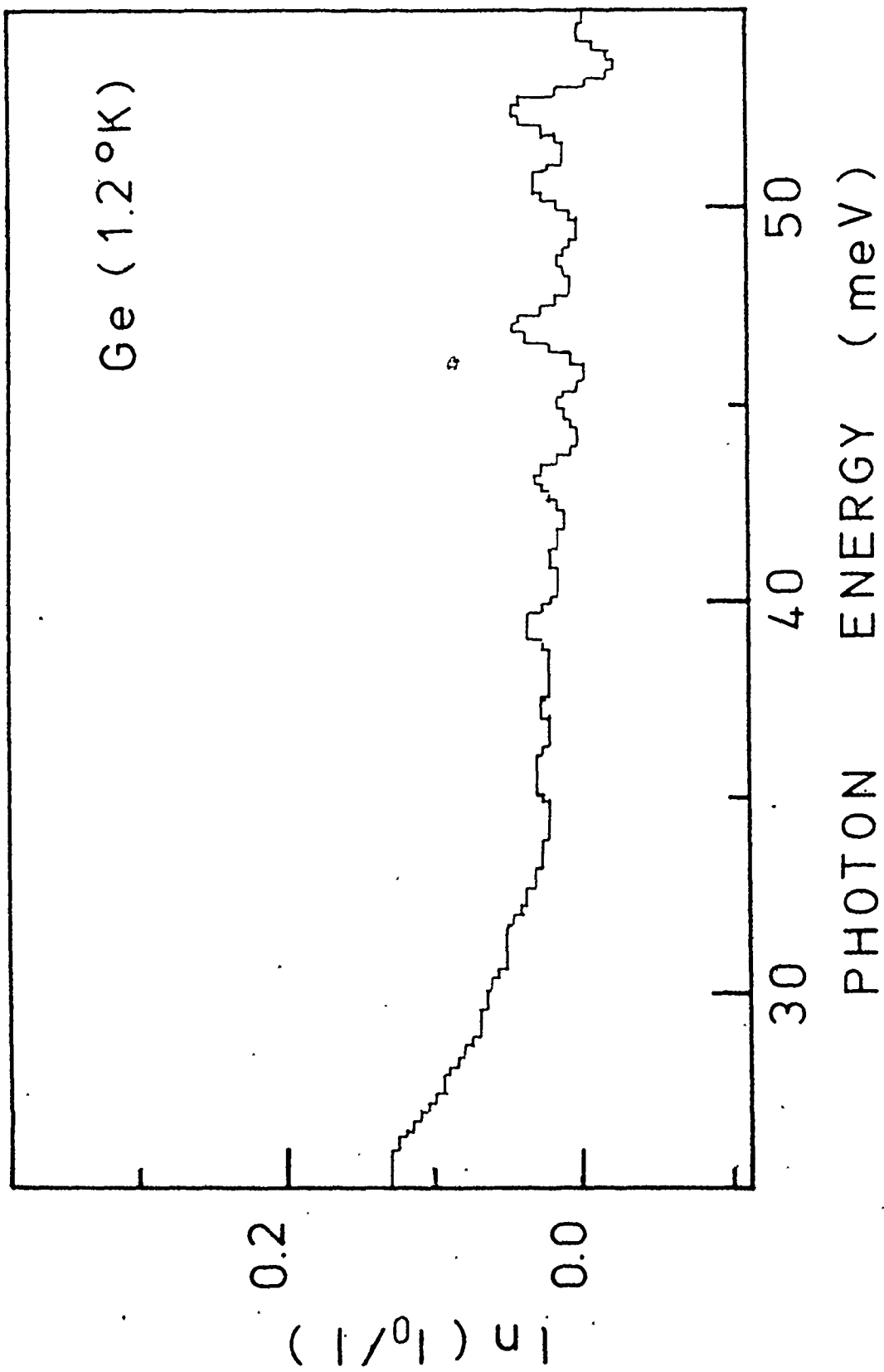


Fig. 3-11

The high-energy region of the absorption spectrum of EHD at 1.2°K. The material becomes transparent at around 40 meV at the cut off of interband transitions.



with the exciting laser off and  $I$  with the laser on; the spectrum shown corresponds to an incident power on the sample of  $\frac{9\text{mW}}{\text{mm}^2}$ . The absorption is a broad and asymmetric line peaking at  $(9.3 \pm 0.1)$  meV, for this particular laser power the maximum of  $\ln\left(\frac{I_0}{I}\right)$  is 0.57. Figure 3-10 shows in detail the low energy region from 1.5 to 7 meV; the exciting power for this case is slightly less than that of figure 3.9, the corresponding absorption at the maximum being estimated as  $\ln\left(\frac{I_0}{I}\right)_{\text{max}} = (0.39 \pm 0.02)$ . The clearest feature in the figure is a sharp threshold at 2.75 meV: the material is completely transparent for lower energies. figure 3-11 shows a measurement of the high energy region from 25 to 55 meV. It is very clear that the material becomes transparent again at around 40 meV; from there on  $\ln\left(\frac{I_0}{I}\right) = 1$  and just an increased noise level produced by the poorer response of the equipment at high frequencies is observed. The estimation for the absorption at the resonance frequency is  $\ln\left(\frac{I_0}{I}\right)_{\text{max}} = 0.58 \pm 0.04$ , at experimental conditions similar to those that produced graph 3-9. For a sample with a uniform concentration of absorbers, the quantity  $\ln\left(\frac{I_0}{I}\right) = \alpha d$  where  $d$  is the thickness of the absorbing region. At medium excitation conditions like the ones presented here, Worlock et al (1974) found that the concentration of drops decreases exponentially with depth; in this case  $\alpha = \alpha(0)e^{-x/d}$  where  $\alpha(0)$  is the absorption constant at the surface. It is easy to show that in this condition  $\ln\left(\frac{I_0}{I}\right) = \alpha(0)d$ . For a high excitation intensity produced by focussing the optical excitation into a small point, generally less than  $100\mu$

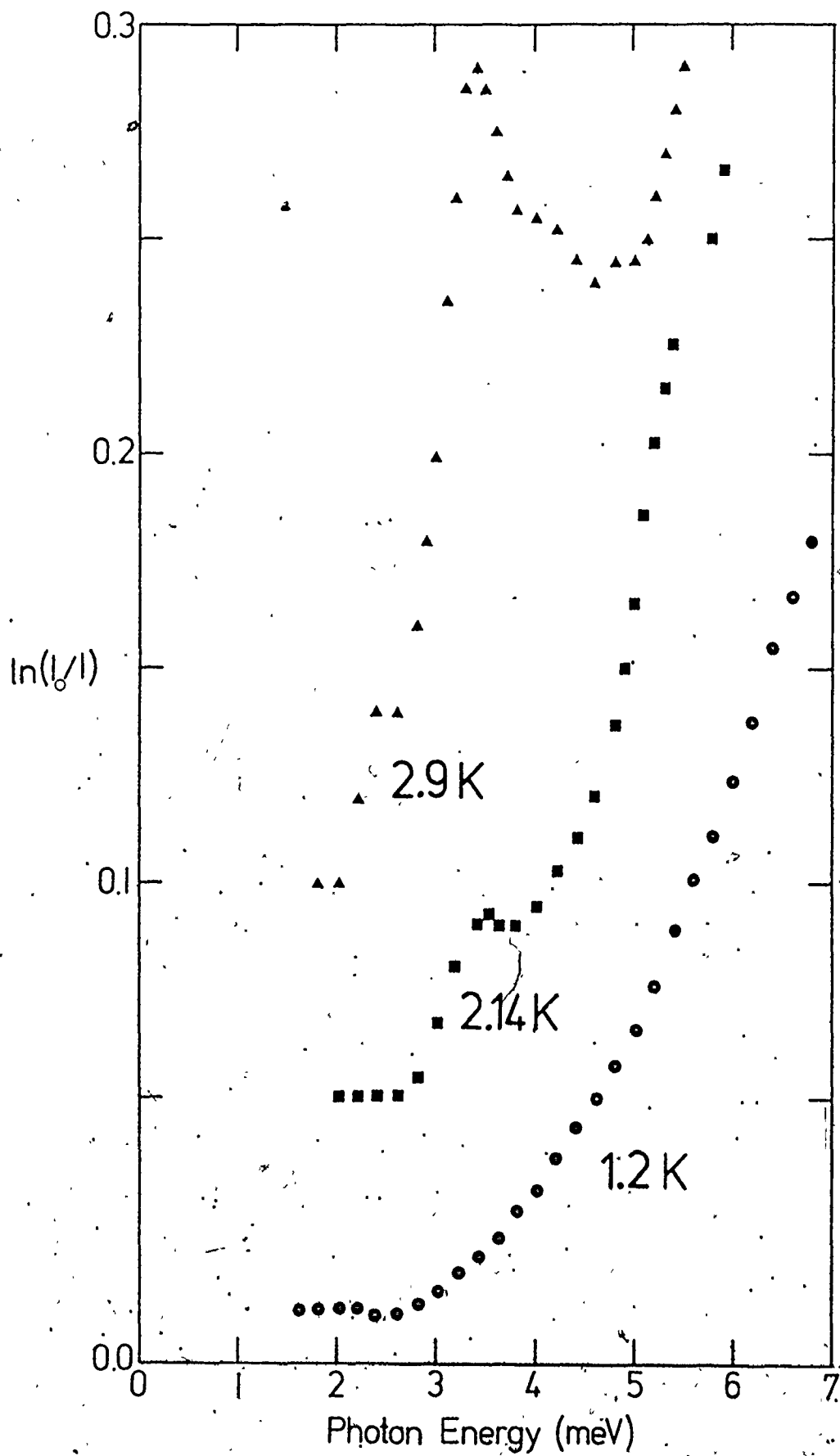
diameter, several investigators (e.g. Alekseev et al, 1974; Voos et al, 1974) found that the drops distribute in a hemispherical cloud around the excitation point. This cloud has a sharp edge and the density changes smoothly inside it ; for these cases clearly, the penetration depth  $d$  is the cloud radius. In general  $d$  changes between 0.3 and 2 or 3 mm depending on the excitation conditions (Pokrovskii and Svistunova, 1974; Bagaev et al, 1976). Under our conditions  $d$  is less than 1 mm and considerably smaller than the sample thickness. We can assume  $\ln \frac{I_0}{I} \sim \alpha_0 = \sigma N_0$  and consider our spectrum to be proportional to the absorption cross section.

Another uncertainty in the experiment is the real crystal temperature. The bath temperature stayed in all experiments fixed at 1.2°K, but the optical excitation can produce a local raise of temperature. Comparing with data taken with temperature controlled samples in exchange gas, we can safely put an upper limit of 2°K in our cases. This is clear from figure 3-12 where we can see the low energy region of the spectrum at different temperatures: at 1.2°K the sharp threshold is evident and there are no signs of excitons. At 2.14°K we note the first appearance of the 3.5 meV exciton absorption, which grows to dominate the threshold region as the temperature is further raised to 2.9°K. Following Manenkov et al (1974), an estimate of the superheating product by the laser excitation may be found from the threshold resistivity of Kapitsa  $R = \frac{\sigma \Delta T}{W} \left( \frac{\text{cm}^2 \text{deg}}{W} \right)$



Fig. 3-12

The low energy region of the spectrum at different temperatures (lines are shifted in 0.05 with respect to each other). At a bath temperature of 1.2°K the sharp threshold at 2.8 meV stands out. As the temperature is raised to 2.14K, the exciton absorption at 3.2 meV can be seen and it completely dominates at 2.9°K.



where  $\sigma$  is the sample exposed area,  $\omega$  is the laser power and  $\Delta T$  the difference in temperature with respect to the bath (Kapitsa 1941). For a He-Ge boundary  $R = \frac{50}{T^3}$  (K.N. Zinov'eva, 1971). For the surface area of our sample ( $11 \text{ cm}^2$ ), irradiation with a 50 mW laser would produce an increase in temperature of only  $.1^\circ\text{K}$ . The certainty that the sample temperature was low validates the use of the approximation  $T=0$  in the calculation of the interband dielectric constant of section 3-4 and intraband damping of section 3-5. The effect of finite temperature in  $\epsilon_{\text{inter}}$  was discussed by Murzin et al; at  $1.2^\circ\text{K}$  it is equivalent to increase by a few percent the interband damping, and is negligible as compared with uncertainties that will be discussed later. The effect on  $\gamma_{\text{intra}}$  is similar.

As will be discussed in the next chapter, the excitation conditions and temperature in our experiments are such that drop sizes are around  $1\mu$ , very small as compared with the wavelength; thus, they absorb in the Rayleigh limit. The absorption cross section can, in this case, be calculated using equation (3.3.16). Fig. 3-13 (solid line) shows the theoretical curve calculated using a dielectric constant that includes intraband and interband transitions as in section 3.4 and with the frequency dependent damping of section 5. The line shown has been obtained using a plasma frequency  $\omega_p = 15.2 \text{ meV}$  corresponding to an electron-hole pair density of  $2.02 \times 10^{17} \text{ cm}^{-3}$  and a hole Fermi energy of  $3.5 \text{ meV}$ . The experimental points in the

Fig. 3-13

Overall absorption spectrum of EHD in Ge. The solid line is a theoretical curve that includes intraband and interband transitions and a frequency dependent electron-hole damping; the electron-hole pair density is  $2.02 \times 10^{17} \text{ cm}^{-3}$ . The dots are the experimental results corresponding to the matching of figures 3-9, 3-10 and 3-11.

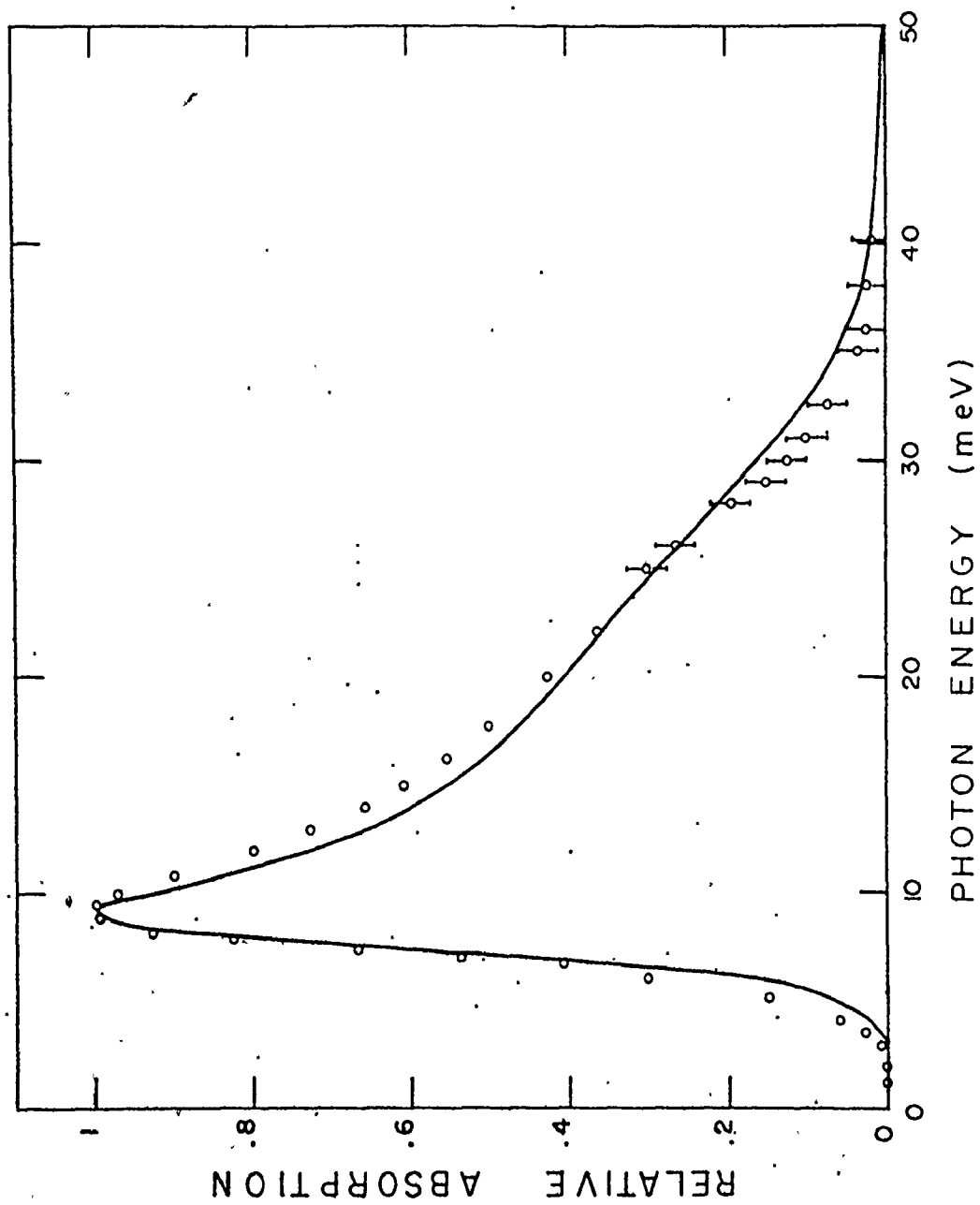


figure correspond to the matching of figures 3-9, 3-10, and 3-11, the large error bars above 25 meV reflect the uncertainty in the matching of the two curves. Theoretical and experimental points have been normalized to the maximum.

To explain the line shape in the region around 10 meV a damping of 2.7 meV is required, while the maximum calculated value is only 1.9 meV. Indeed, a very good fit to the experiment is possible if the damping curve of fig. 3-8 is just multiplied by the constant factor of 1.4. There are two effects that can contribute to this discrepancy: first, the static approximation used in the calculation of section 3.5. Tzoar and Platzman find that dynamic correlation effects are important in the frequency region where plasma oscillations occur, and have the effect of increasing the damping considerably. The second effect is the interband damping: the solid line in fig. 3-13 was obtained assuming it was the same as the intraband without any particular justification. Within the random phase approximation used in section 3.4 for the calculation of the dielectric constant there is no broadening of the states involved; usually the broadening is phenomenologically fitted to the experimental points. A self consistent calculation similar to that of Tzoar and Platzman or that of Silver and Aldrich (1978), who calculated the interband absorption for heavy hole-split off band transitions using multiple scattering theory, would be required. As was discussed in section 3.4 (eq. (3.4.11) and (3.4.20), damping values for both the intraband and interband

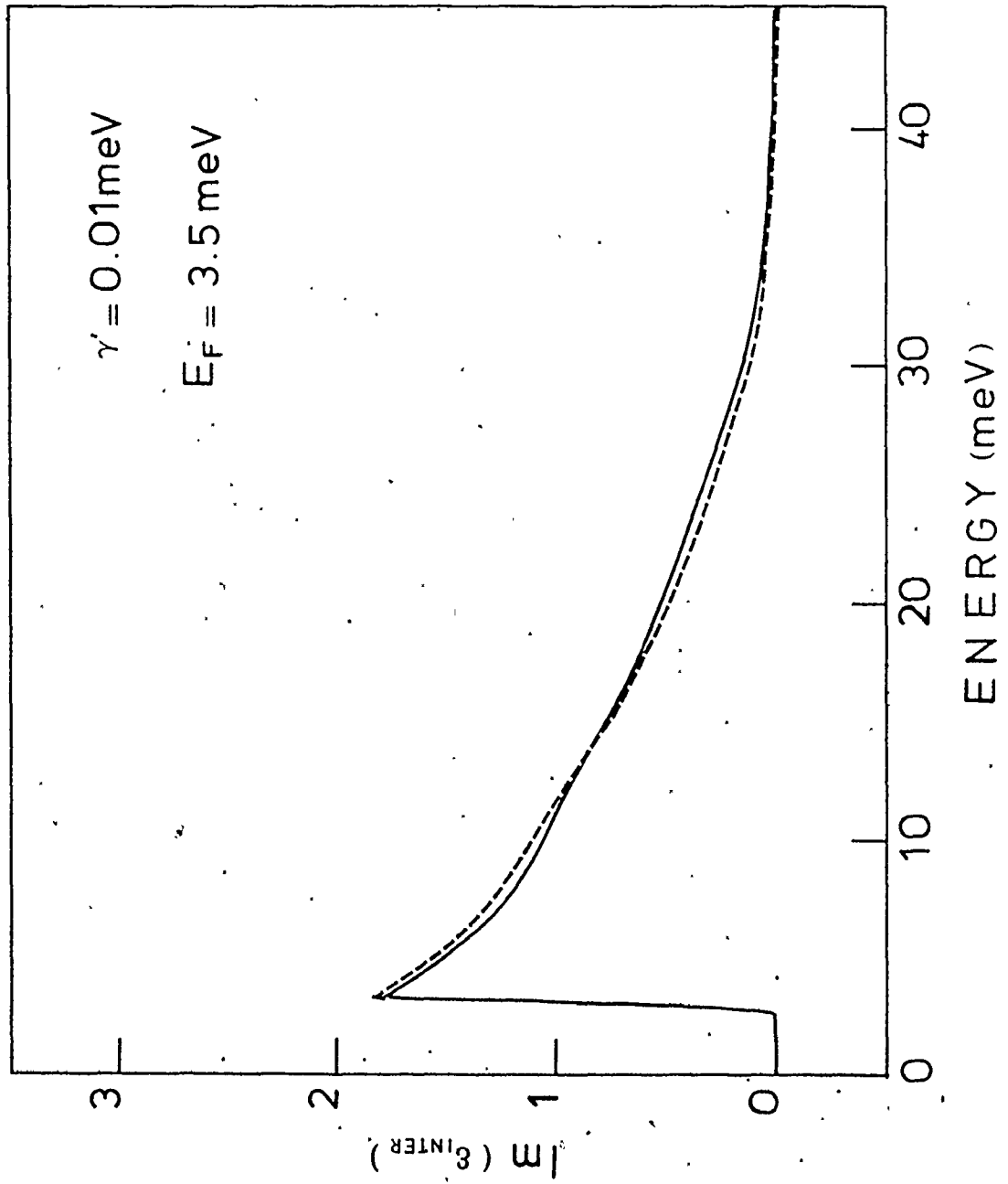
terms change the resonance condition affecting the electron-hole pair density value obtained from it. If smaller interband damping is assumed for the same intraband value a better fit to the experimental results is obtained; actually both dynamical correlation effects and interband damping should be included at the same time in a calculation if a good value of  $n$  from the peak position is required; since both effects are of the same order, it makes no sense to include one of them without considering the other.

At high frequencies (30 meV and over) the theoretical absorption is slightly higher than the experimental results. At these frequencies the absorption is mainly produced by the interband transitions and any discrepancy can be attributed to the approximations used in the calculation of the interband dielectric constant. In the appendix I calculate the matrix elements for the interband transitions in the valence band of Ge under [111] uniaxial stress. As it is discussed there, eq. (3.4.18) is just a particular case of eqs. (A.22) to (A.24) for zero stress and spherical approximation. A calculation of the  $\text{Im}(\epsilon_{\text{inter}})$  with the matrix elements of eqs. (A.22) to (A.24) is shown in fig. 3-14, together with one where the spherical approximation matrix elements were used. The correct matrix elements give a slightly larger value of  $\text{Im}(\epsilon)$  at low frequencies and smaller  $\text{Im}\epsilon$  at frequencies larger than 15 meV; the difference becomes relatively important at high frequencies. At

Fig. 3-14

Imaginary part of the interband dielectric constant with different matrix elements. The solid line corresponds to the spherical approximation; the broken line uses the correct expression from the appendix at zero stress.





30 meV it is about 30% of its approximate value. The magnitude and sign of this correction agrees with the discrepancy observed at high energies. Clearly the spherical approximation used in the calculation of the curve of fig. 3-13 is what produces the difference with the experimental points at high energies.

The value for the density obtained from the plasma frequency can be compared with the result obtained from other features in the curve. As shown in section 3-4, the threshold and cutoff of the interband transitions are related to the electron hole density via the Fermi energy (eqs. (3.4.14) and (3.4.15)). Experimentally they appear at 2.8 and 42 meV respectively (after correction for resolution broadening). These values are in agreement with a density of  $2.02 \times 10^{17} \text{ cm}^{-3}$ . A summary of results is presented in table 2.

The electron-hole pair density changes with temperature. Minimizing the Landau theory free energy, it can be easily shown that it decreases as  $T^2$ :

$$n(T) = n_0 (1 - \delta_n (k_B T)^2) .$$

$\delta_n$  is a factor of the order of 1 in Ge. Thomas et al (1973) measured a value of 0.94, Lo (1974) gives 1.35 and theoretical calculations by Vashista et al (1974) gives 1.2 (value in  $\text{meV}^{-2}$ );  $n_0$  is the density at  $0^\circ\text{K}$ . Using  $T = 1.2^\circ\text{K}$  and  $\delta_n = 1.3$ , a value of  $n_0$  larger than  $n$  by  $0.03 \times 10^{17} \text{ cm}^{-3}$  at  $2^\circ\text{K}$ .

Table 2

Experimental values of electron-hole  
pair density for EHD in Ge

<u>Method</u>	<u>Result</u>	<u>nd (<math>10^{17} \text{cm}^{-3}</math>) (T = 1.2°K)</u>
Peak position (9.3 meV)	$\omega_p = 15.2 \pm 0.1$	$2.02 \pm 0.05$
Threshold at 2.8 meV	$E_{Fh} = 3.5 \pm 0.13$	$2.04 \pm 0.10$
Cutoff at 42 meV	$E_{Fh} = 3.6 \pm 0.3$	$2.1 \pm 0.3$

## CHAPTER 4

### THE INFLUENCE OF DROPLET SIZE ON THE PLASMA RESONANCE

#### 4.1 Introduction

Slight variations in the lineshape of the EHD plasma resonance line have been reported by earlier investigators (Vavilov et al, 1969; Timusk and Silin, 1975). This effect seemed surprising in the light of the model of dipolar absorption used to interpret the data. Within the Rayleigh limit for the absorption cross section (eq. 3.3.16),  $\alpha d$  is proportional to the filling factor of electron-hole drops in the absorbing region and the cross section per electron-hole pair is a constant at a given frequency. Then, if the density of electron-hole pairs is kept constant, only the maximum value of the absorption should change and the lineshape should remain the same for the different experimental conditions. The small variations in lineshape (especially line broadening) can be traced to sample heating produced by the excitation source. This heating contributes in two ways to the lineshape changes. At temperatures larger than 2°K the vapor pressure of the exciton gas is high enough to cause an observable exciton absorption between 3 and 6 meV. The photoionization tail acts to distort the droplet lineshape. This effect was already

discussed in section 3. At high temperature and/or high excitation, drops are larger (Bagaev et al, 1976; Aksenov and Zhurkin, 1980) and this change in size affects the lineshape. Distortion in the spectra is observed, too, when the temperature and excitation level are very low. It is shown in this chapter that in these conditions drops are so small that surface effects are important and change the lineshape.

The aim of this chapter is to study these effects. I present here lineshapes measured over a wide range of excitation intensities. The corresponding absorption at the peak of the line varies from 0.06 to 1.6. Special precautions have been taken to avoid sample heating, and in this way obtain the lineshape at different excitation intensities with minimum temperature influence. Size effects can be observed at both very high and very low excitation. Estimates of the droplet sizes were obtained by numerical fit.

The results of this chapter were previously published (Timusk and Zarate, 1977; Zarate and Timusk, 1979).

#### 4.2 The Line Shape of Drops with Radii Comparable to the Wavelength of Electromagnetic Radiation

Rose, Shore and Rice (1978) realized that when the droplet radius begins to approach the wavelength of the electromagnetic radiation in the medium, the dipolar approximation for the absorption cross section does not hold and the full Mie theory for homogeneous sphere of section 3.3 has to be applied to study the plasma resonance of EHD. They calculated the

extinction cross section for a variety of drop sizes and found that below 1  $\mu\text{m}$  lines do not change and the limiting case for small drops is applicable (eq. 3.3.16).

In section 3.3 it is shown that if particles remain smaller than the wavelength of the incoming radiation ( $\frac{2\pi}{\lambda} \sqrt{\epsilon_0} R \lesssim 1$ ), the coefficients  $a_n$  and  $b_n$  of the Mie expansion (eq. (3.3.10 and 3.3.11) are usually computed by expanding them in a power series in  $k_1 R$ . In this way equation (3.3.14) for the extinction cross section  $\sigma_{\text{ext}}$ , and (3.3.15) for the scattering cross section are obtained. In (3.3.14) the term  $\alpha R^3$  is the Rayleigh limit and describes the scattering for EHD with  $R \lesssim 1 \mu$ . For drops of the order of 2  $\mu\text{m}$  terms  $\alpha R^5$  and  $\alpha R^6$  become important and the lineshape becomes a function of drop size. The absorption cross section, in this case, is:

$$\sigma_{\text{abs}} = 4\pi k_1 R^3 \left\{ \text{Im} \left[ \left( \frac{\bar{\epsilon}-1}{\bar{\epsilon}+2} \right) + \left( \frac{k_1 R}{15} \right)^2 \left( \frac{\bar{\epsilon}-1}{\bar{\epsilon}+2} \right)^2 \left( \frac{\bar{\epsilon}^2 + 27\bar{\epsilon} + 38}{2\bar{\epsilon}+1} \right) \right] + \right. \\ \left. + (k_1 R)^3 \left[ -\frac{2}{3} \text{Re} \left( \frac{\bar{\epsilon}-1}{\bar{\epsilon}+2} \right)^2 + \left| \frac{\bar{\epsilon}-1}{\bar{\epsilon}+2} \right|^2 \right] \right\} \quad (4.2.1)$$

The line obtained with this approximation for 2  $\mu\text{m}$  drops agrees with the results of Rose et al using the full Mie equations.

#### 4.3 Surface Effects

At 1.2°K and very low excitation intensity EHD in Ge are expected to be very small. Etienne et al (1975) worked with excitation levels between 20 and 430  $\mu\text{W}/\text{mm}^2$  found drops smaller than 0.15  $\mu\text{m}$ . An estimate of their size can be found by setting

the rate of decay of the carrier in the drop equal to the rate of inflow of excitation. This approximation neglects evaporation and surface energy contribution to the radius. With this method (Pokrovskii and Svistunova, 1970):

$$R = \frac{3}{4} \frac{v_{ex} n_{ex} \zeta_0}{n}$$

where  $v_{ex}$  and  $n_{ex}$  are the velocity and density of excitons;  $\zeta_0$  and  $n$  the lifetime and density of EHD.

Values as low as 0.2  $\mu\text{m}$  have been obtained with this method by Gershenzon et al. (1976).

When drop sizes in Ge become this small, surface effects are important. Two effects would affect the lineshape in this case. First, the electron-hole density near the surface decreases from its bulk value to zero in a continuous fashion; thus the drop has a skin of the order of the excitonic Bohr radius  $r_0$  of lower density surrounding the core of bulk density (Kalia and Vashishta, 1978). As the drop radius decreases more of the volume fraction of the drop belongs to this skin and its electromagnetic properties are modified. At the same time, collisions with the surface begin to affect the lifetime of the carriers; as a consequence the damping is increased.

The effect of the lower surface density is approximated with the "coated-sphere" model for the electron-hole drop. The drop is assumed to have a core characterized by a dielectric constant  $\epsilon_1$  and to be surrounded by a coating of thickness  $r_0$ .

with a different dielectric constant  $\epsilon_2$  uniform throughout the coating. The absorption constant for a coated sphere with radius  $R$  much smaller than the wavelength of the medium is (Kerker, 1969);

$$Q = 4\pi k_1 R^3 \operatorname{Im} \left( \frac{(\epsilon_2 - 1)(\epsilon_1 + 2\epsilon_2) + \alpha^3 (2\epsilon_2 + 1)(\epsilon_1 - \epsilon_2)}{(\epsilon_2 + 2)(\epsilon_1 + 2\epsilon_2) + \alpha^3 (2\epsilon_2 - 2)(\epsilon_1 - \epsilon_2)} \right) \quad (4.3.2)$$

where

$$\alpha = (R - \frac{1}{2} r_0) / (R + \frac{1}{2} r_0) .$$

For  $R \gg r_0$ ,  $\alpha \rightarrow 1$  and eq. (4.2.3) reduces to the dipolar absorption for a sphere. If  $R \gtrsim r_0$  the absorption depends on the size of the drop and the difference between  $\epsilon_1$  and  $\epsilon_2$ . In the model  $\epsilon_1$  is the bulk dielectric constant calculated in (3.4) and  $\epsilon_2$  is equal to the dielectric constant of the bulk EHD of section 3.4, but with only half the density.

For these small drops the damping is given by

$$\frac{1}{\tau} = \frac{1}{\tau_1} + \frac{v_F}{R} \quad (4.3.3)$$

where  $\frac{1}{\tau_1}$  is the damping in absence of surface effects and  $v_F$  is the Fermi velocity. The second term  $v_F/R$  is the time between collisions with the surface of a sphere of radius  $R$  (Euler, 1954). This term adds a further size dependence.

#### 4.4 Experimental Results

The far infrared absorption of EHD in Ge was studied under a larger range of optical excitations. The corresponding



absorption at the peak of the line varies from 0.02 to 1.6. The dependence of  $\alpha d(\max)$  with the excitation density changes at  $\ln\left(\frac{I_0}{I}\right)_{\max} = 0.2$ . Below this value we found  $\ln\left(\frac{I_0}{I}\right)_{\max} \propto \omega^3$  and above this  $\ln\left(\frac{I_0}{I}\right)_{\max} \propto \omega^{0.7}$ .  $\ln\left(\frac{I_0}{I}\right)_{\max} = 0.2$  corresponds to an incident power density of  $W = 2\text{mW/mm}^2$ . The values of  $\alpha d$  obtained are somewhat smaller than those expected for the power and wavelength of the exciting radiation. A top limit to the value of  $\alpha d(\max)$  as a function of the incident power can be easily obtained assuming that every photon incident on the sample produces an electron-hole pair that condenses in EHD. In this case:

$$g = \frac{N}{\tau_0} \quad (4.4.1)$$

where  $g$ : number of photons incident per second  
 $N$ : number of non equilibrium carriers in the sample  
 $\tau_0$ : lifetime of EHD.

With the assumption that the electron hole fluid occupies a volume equal to the area of the laser spot ( $A$ ) times the penetration depth ( $d$ ),  $\alpha d(\max)$  is given by:

$$\alpha d(\max) \leq \frac{g \tau_0 \sigma(\max)}{An} \quad (4.4.2)$$

where  $\sigma(\max)$  is the maximum value of the cross section per electron hole pair and  $n$  is the density of electron-hole pairs in the drop. From eq. (4.4.2) an incident power density of  $2\text{mW/mm}^2$  would give a maximum possible value  $\alpha d(\max)$  of 0.6.

When the excitation is such that the absorption at the maximum of the peak  $\alpha_d(\max)$  is between 0.4 and 1.2 no variation of the lineshape with excitation can be seen. The results agree with the theory of chapter 3 and the line is given by fig. 3-13. Outside these limits the lineshape does begin to change. Figure 4-1 shows the absorption at very low, medium and very high excitation levels. At very low excitations the peak shifts towards lower frequencies and there is some additional broadening. A similar effect occurs at very high levels of excitation. These curves have been fitted to the Mie theory using the droplet size as an unknown parameter. For the  $\alpha_d(\max) = 2.1$  curve a radius  $r = 2.0 \pm 0.2 \mu\text{m}$  has been obtained. For the low excitation curve fitting the coated sphere model of eq. (4.3.2) together with the damping of (4.3.3) gives a drop radius of  $0.06 \mu\text{m}$ . No observation of drops with  $\alpha_d(\max) < 0.03$  was possible. This corresponds to  $R < 0.05 \mu\text{m}$ . Figure 4-2 shows the far-infrared spectrum obtained in this case. At 3.5 meV an exciton absorption with  $\alpha_d(\max) \approx 0.004$  is observed. At higher excitation levels the exciton absorption cannot be observed at this temperature. The presence of excitons allows us to obtain another estimate of the drop sizes using the Pokrovskii radius of eq. (4.3.1), for  $\alpha_d(\max)_{\text{exciton}} = 0.004$  and using the effective exciton mass of Kane (1975), a radius of approximately  $0.07 \mu\text{m}$  is obtained. These droplet sizes are

Fig. 4-1

Effect of the excitation level on the shape of the EHD absorption. The filled circles correspond to a medium level of excitation. At low levels of excitation (the triangles), the line shifts to lower frequencies. Also, at very high levels of excitation (open circles) the line shape changes.

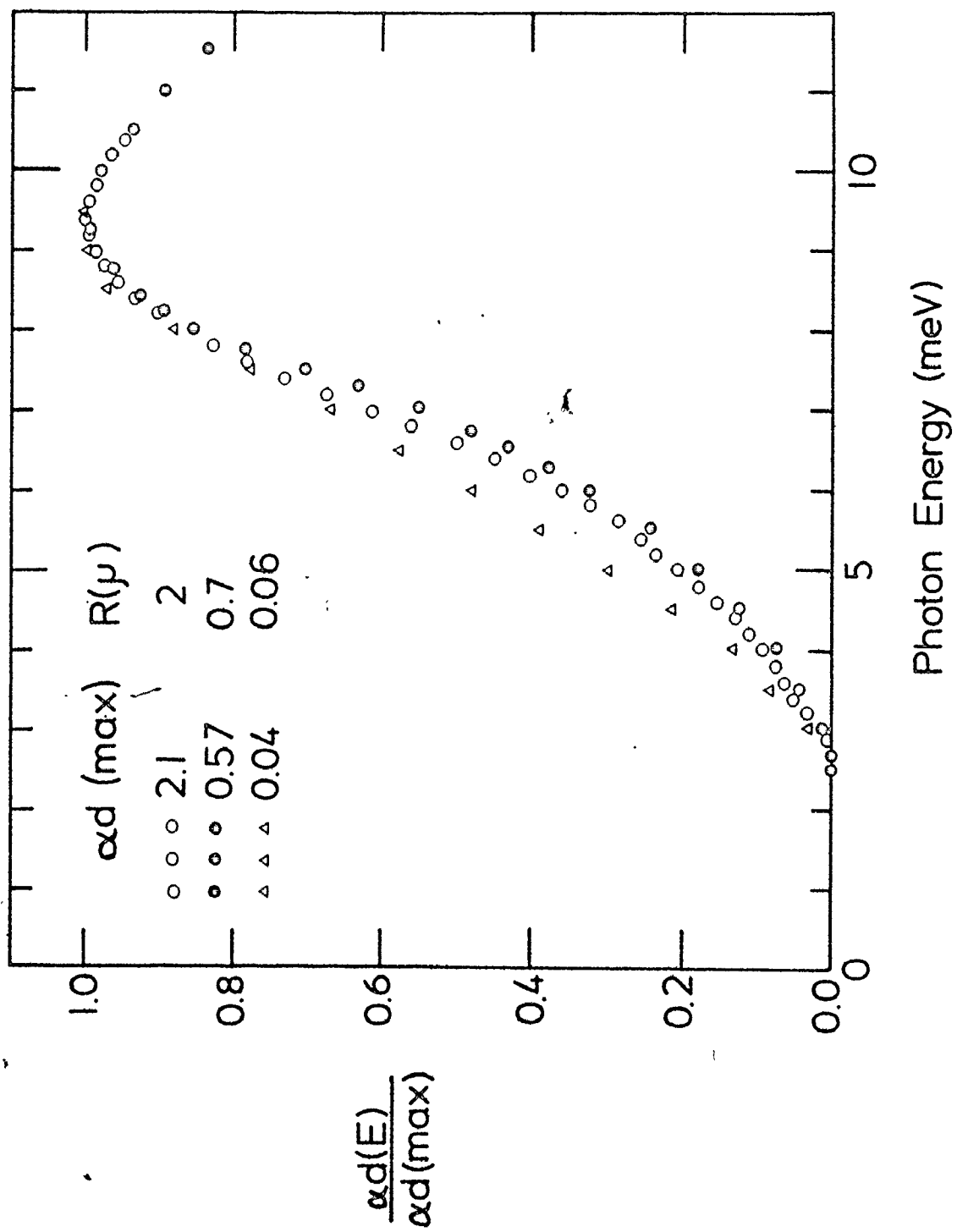
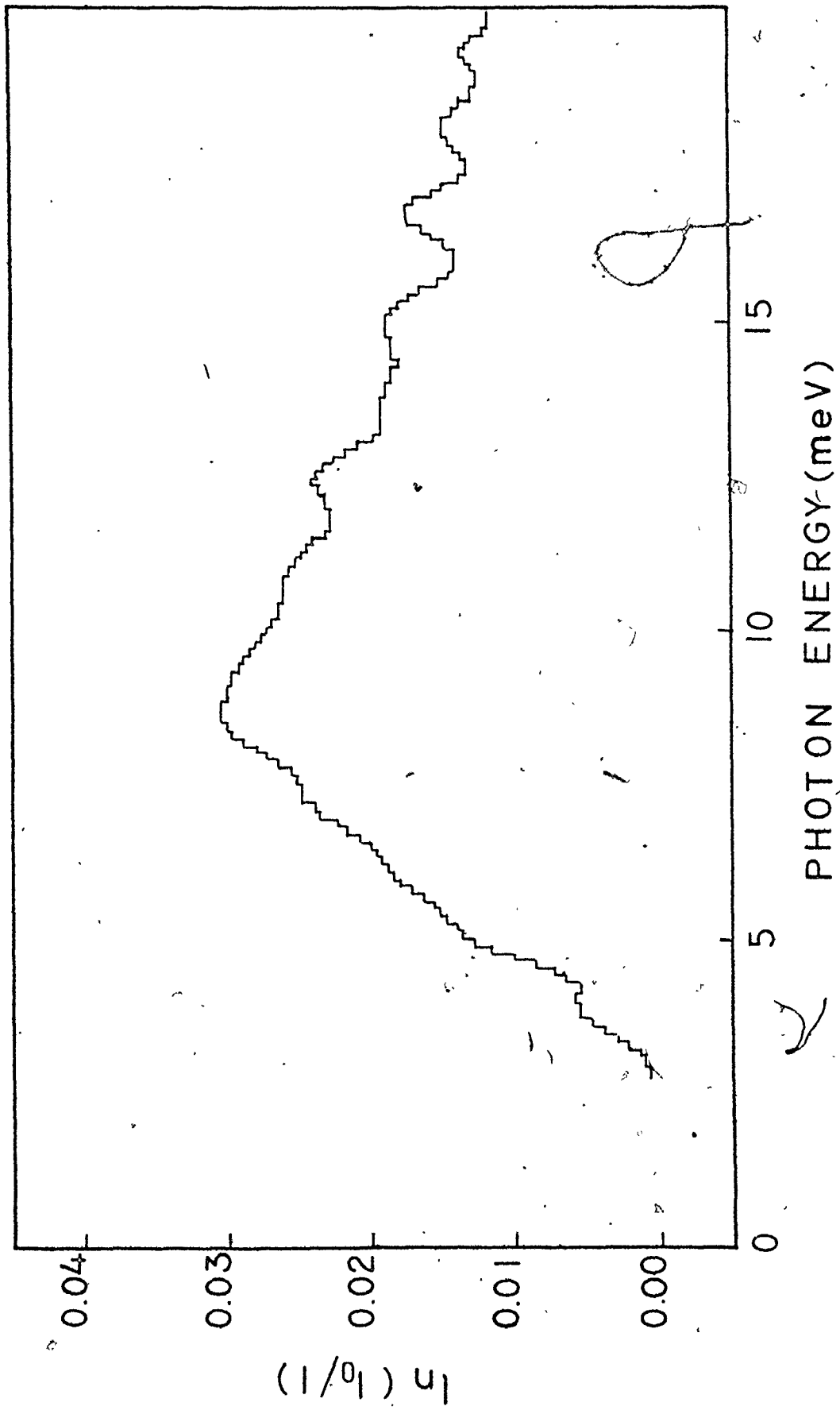


Fig. 4-2

Far-infrared spectrum of EHD at very low excitation levels. The line corresponds to the lower level at which drops were observed. The estimated drop size is  $R \approx 0.05 \mu\text{m}$ .



clearly near the minimum stable radius of EHD at 1.2°K. Westvelt (1976) has calculated, using nucleation theory, a radius of 0.04  $\mu\text{m}$  near threshold at 1.2°K assuming homogeneous nucleation.

The size of the drops as a function of the strength of the absorption at the peak  $\alpha d(\text{max})$  can be obtained using the coated sphere model. The simplest way of doing this is to fit the experimental value of  $E_{1/2}$ , the frequency of the low frequency half maximum, to the value predicted by the coated-sphere model. Fig. 4-3 shows the experimental  $E_{1/2}$  plotted as a function of  $\alpha d(\text{max})$ . It can be seen that at very low excitations where  $\alpha d(\text{max}) < 0.1$ , the line begins to move to lower frequencies very rapidly. The slight drop in the points at  $\alpha d(\text{max}) > 1.6$  is due to higher-order terms in the Mie expansion. Figure 4-4 shows the drop sizes calculated this way: the coated-sphere model is used to fit  $E_{1/2}$  for small  $\alpha d(\text{max})$  and the higher-order Mie terms for  $\alpha d \sim 2.0$ . There are no points for  $0.3 < \alpha d(\text{max}) < 1.5$  since here the line shape is almost independent of drop size. From these points it appears that the droplet size varies approximately linearly with  $\alpha d(\text{max})$ . This fact should not be considered too seriously. The error bars in fig. 4-4 come only from experimental uncertainties. The model used to fit the data is subject to several uncertainties such as the assumptions of a constant density surface layer and unmodified scattering rate. The actual error bars of the radii can be larger, especially at low  $\alpha d$  values. If the concentra-

Fig. 4-3

Change in the frequency of the low-energy half-maximum absorption point ( $E_{1/2}$ ) as a function of maximum absorption.



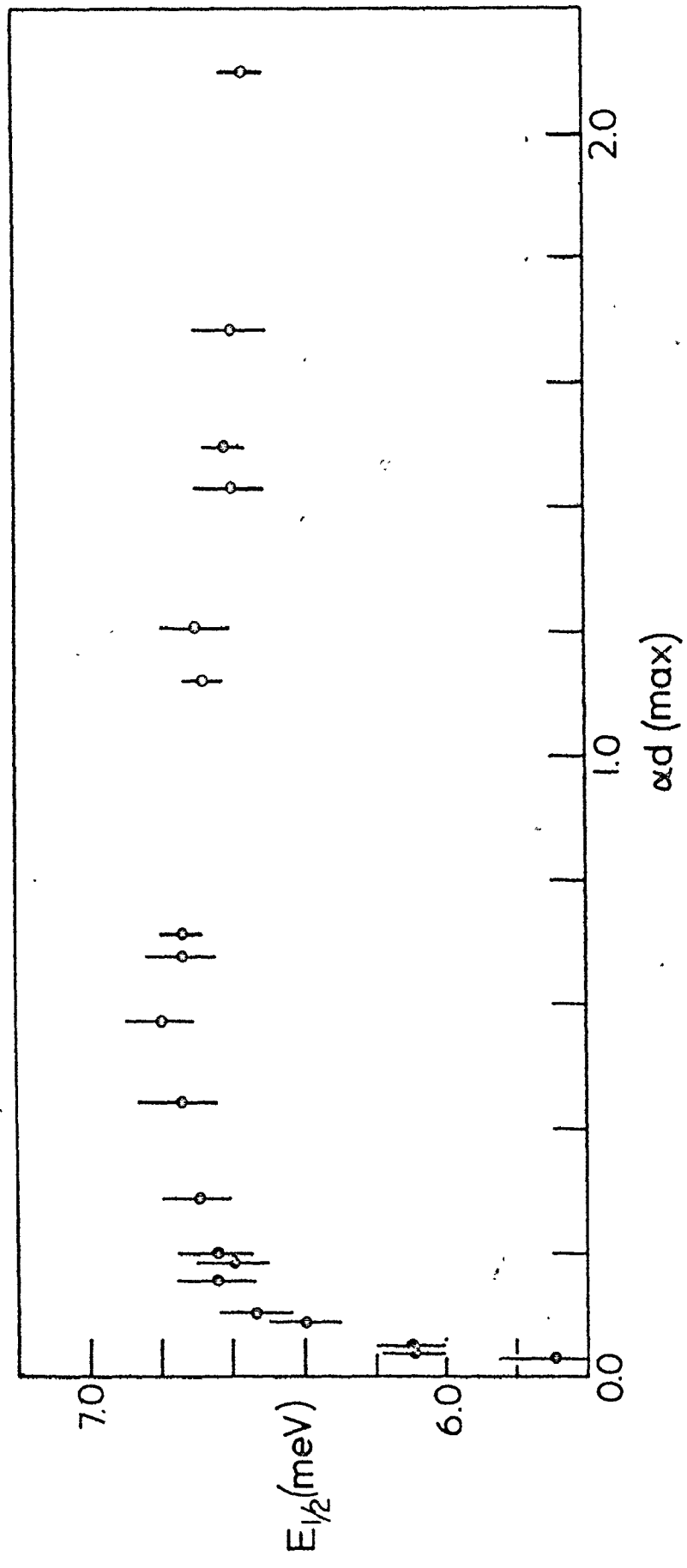
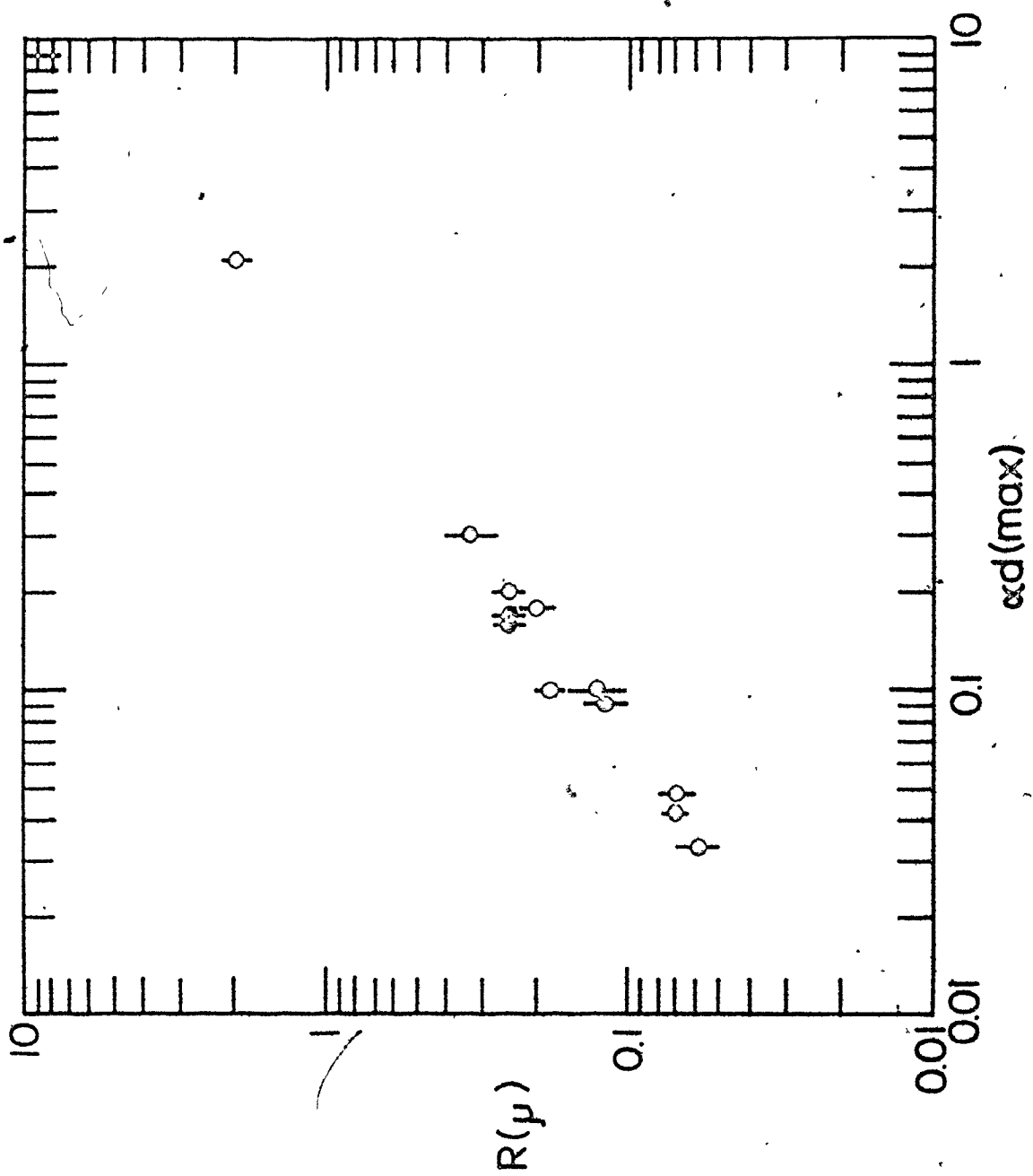


Fig. 4-4


Calculated droplet radii as a function of absorption level. The points for  $\alpha d \leq 0.3$  were obtained by fitting the  $E_{1/2}$  point to the coated sphere model of the EHD absorption. For  $\alpha d = 2.1$  the calculation was extended to include higher-order terms in the expansion. Between these values the lineshape is independent of the drop radius.



tion of drops remains constant,  $R$  should be proportional to  $(\alpha d)^{1/3}$ . A fact that can contribute to the steep dependence observed is the increase in drop temperature with excitation. Higher temperature decreases the concentration of EHD (Bagaev et al, 1976) and hence the absorption coefficient for a given droplet size and cross section for electron-hole pair.

The size of drops observed agrees with the size observed by other investigators under comparable conditions. Etienne et al (1975) worked with excitation levels between 20 and  $430 \mu\text{W}/\text{mm}^2$  and found drops smaller than  $0.15 \mu\text{m}$  and a good fit to a linear relationship between droplet radius and the excitation level. Extrapolating their data to our conditions we find our sizes range between  $0.1$  and  $1.5 \mu\text{m}$ . Bagaev et al measured drops at  $3.8$  and  $8 \text{ mW}$  on a  $200 \mu\text{m}$  spot from  $2$  to  $4^\circ\text{K}$ . Extrapolating their curves gives values similar to the ones shown in fig. 4-4.

The shift of the plasma resonance towards low frequency at very high excitation levels was observed by Zayats et al (1977) as well. They worked with exciting powers of around  $10 \text{ mW}/\text{mm}^2$  but with very small "bounded" samples with thickness much smaller than the penetration depth ( $d \approx 0.06 \text{ mm}$ ). Under these conditions they observed shifts of the line towards lower frequencies that they explain in terms of a distribution of drop sizes ranging up to  $16 \mu\text{m}$ .



## CHAPTER 5

### THE INFLUENCE OF UNIAXIAL STRESS ON THE PLASMA RESONANCE

#### 5.1 Introduction

Since very early in the history of the electron hole drops, the study of the effect produced on the fluid by deformation of the semiconductor crystal has received the attention of several investigators. The early studies of the luminescence spectra by Bagaev et al. (1969), Benoit à la Guillaume et al. (1970-1972), Alekseev et al. (1973) and Pokrovskii and Svistunova (1974) showed the existence of the liquid phase and that it was modified by stress (shift in peak position and change in linewidth and intensity of the luminescence line were observed). These changes were qualitatively consistent with a decrease in the liquid binding energy and density of the fluid with stress.

Application of a [111] stress to germanium removes several of the degeneracies of the conduction and valence bands. The conduction ellipsoid whose main axis is parallel to the stress is lowered in energy while the three others are raised. The valence-band maximum is split into two branches but considerable coupling between them remains until large stresses. In the limit of very large stress the two hole bands become

ellipsoids and the calculation of the electron-hole liquid properties becomes very simple. For this reason all the early theoretical studies were in the "infinite" stress limit. The first calculations of Combescot and Nozières (1972) and Brinkman and Rice (1973) gave an electron-hole liquid barely bound or not bound with respect to the exciton state. A more sophisticated calculation of Vashishta et al. (1974) showed that the liquid is stable at infinite stress with a density considerably reduced from the zero stress case. Vashishta et al. (1976) also studied an ideal system with electron effective masses corresponding to infinite stress and hole effective masses at zero stress; they found this system to also be stable and with an EHL density intermediate between the other two cases. Calculations of the electron-hole density and binding energy at finite stress values were carried out recently by L. Liu (1978 a,b), Markiewicz and Kelso (1978), Kirczenow and Singwi (1979) and Kelso (1979) using different approximations.

Some recent luminescence studies with uniform uniaxial [111] stress in Ge by Chou, Wong and Feldman (1977), Feldman et al. (1977, 1978) and Thomas and Pokrovskii (1978) give experimental results for the electron-hole density at several stress values which agree reasonably well with the theory at intermediate and high stresses, but there is still some uncertainty about the behaviour at low stress, especially in the region around  $3 \text{ kg/mm}^2$ . Near this stress the upper ellipsoids empty and current theory predicts a very sharp decrease of density

in a very narrow range of stress. The luminescence results are not sensitive enough to draw any conclusions about this region.

No observations of the far infrared absorption of EHD in Ge under uniform uniaxial stress existed previously to this thesis. Aurbach et al. (1976) measured the far infrared absorption in inhomogeneously stressed Ge along the [110] and [100] directions obtaining a spectrum very similar to that of the unstressed EHD but broader, particularly in the low energy region for [110] stress. Similar results were obtained by S. Pak (1975). Aurbach et al. interpreted their data as the absorption produced by a giant drop ( $\gamma$  drop), 250  $\mu$  in size, confined because of the stress and with a reduced electron-hole density and damping constant. They obtained a fairly good fit with those values without including interband transitions and mass anisotropy. The similarity with the zero stress case suggests another possible explanation: the spectrum is just that of "normal" drops broadened at low energies because of the stress inhomogeneity. Presumably ordinary drops occur in the low stress regions of the crystal near the surface and are observed as they diffuse toward the stress well. The large drop in the well itself is not observable because of its small cross-section relative to the broad infrared beam.

A theoretical estimate of the far infrared absorption of EHD under uniform stress was given by Markiewicz (1978a). He

studied the effect of electron mass anisotropy on the plasma resonance and found that in EHD in Ge stressed along the [111] direction the absorption would depend on the direction of polarization of the electric field.

The purpose of this chapter is the experimental study of the effects of uniaxial stress on the resonance absorption of electron-hole drops in Ge. In the next sections I investigate theoretically the effects of uniaxial [111] stress in the Ge band structure and hence in the far infrared absorption. Section 5.2 gives the absorption cross section for small drops under uniaxial stress. In section 5.3 the dielectric function as a sum of the Drude intraband contributions and the interband transitions between the stress split valence band branches, is calculated. The experimental results are presented and discussed in section 5.4 and a summary and conclusion are given in section 5.5.

## 5.2 The Absorption Cross Section for Small Drops Under Uniaxial Stress

Application of uniaxial stress to a Ge crystal destroys its cubic symmetry. The conductivity and dielectric constant are no longer scalars. For a coordinate system with the z axis along the stress direction the conductivity tensor is diagonal and the dielectric tensor has the form:

$$\epsilon_{ij} = \begin{pmatrix} \epsilon_{\perp} & 0 & 0 \\ 0 & \epsilon_{\perp} & 0 \\ 0 & 0 & \epsilon_{||} \end{pmatrix} \quad (5.2.1)$$



where  $\epsilon_{\perp}$  and  $\epsilon_{\parallel}$  stand for the components of the dielectric constant perpendicular and parallel to the stress direction, respectively. We have seen in Chapter 3 that for small particles the absorption cross section can be calculated in the Rayleigh limit (only electric-dipole terms considered). In this case eq. (3.3.16) can be generalized using depolarization fields (see for example van de Hulst, Chapter 6), to include an anisotropic medium. The absorption coefficient for a small sphere with an anisotropic dielectric constant (5.2.1) is:

$$\alpha(\omega) = \frac{4\pi\omega}{C} \sqrt{\epsilon_0} NR^3 \left\{ \cos^2\theta \operatorname{Im} \left( \frac{\epsilon_{\parallel} - \epsilon_0}{\epsilon_{\parallel} + 2\epsilon_0} \right) + \sin^2\theta \operatorname{Im} \left( \frac{\epsilon_{\perp} - \epsilon_0}{\epsilon_{\perp} + 2\epsilon_0} \right) \right\} \quad (5.2.2)$$

where  $\theta$  is the angle between the electric field and the z axis.

### 5.3 The Dielectric Function

Generalizing eq. (3.4.2) to (3.4.5) the intraband contributions to the dielectric function, parallel and perpendicular are given by:

$$\epsilon_{\parallel \text{ intra}} = - \frac{4\pi e^2}{\omega(\omega + i\gamma_{\parallel})} \left[ \frac{n_e}{m_{oe\ell}} + \frac{n_H}{m_{oHh\ell}} + \frac{n_L}{m_{oLh\ell}} \right] \quad (5.3.1)$$

$$\epsilon_{\perp \text{ intra}} = - \frac{4\pi e^2}{\omega(\omega + i\gamma_{\perp})} \left[ \frac{n_e}{m_{oet}} + \frac{n_H}{m_{oHht}} + \frac{n_L}{m_{oLht}} \right] \quad (5.3.2)$$

The subscripts  $\ell$  and  $t$  stand for longitudinal and transverse.

The quantities  $n_e$ ,  $n_H$ ,  $n_L$ ,  $m_{oe}$ ,  $m_{oHh}$ ,  $m_{oLh}$ ,  $m_{oet}$ ,  $m_{oHht}$  and  $m_{oLht}$  are stress dependent.

The first term of the right hand side of equations (5.3.1) and (5.3.2) is due to the conduction band. As it was discussed in section 5.1, application of stress along the [111] direction lowers in energy the ellipsoid along this direction and raises the other three (see fig. 5.1). For Ge, the splitting between these bands is (Hensel and Suzuki, 1974):

$$\Delta_e = 1.03 \text{ meV}/(\text{kg}/\text{mm}^2) \cdot |S| \quad (5.3.3)$$

where  $S$  is a compressive stress (negative sign) in  $\text{kg}/\text{mm}^2$ .

If the stress is large enough that the electron Fermi energy is smaller than the splitting, then only one valley is occupied. Assuming that the valleys retain the same effective mass as for  $S = 0$  then for  $\Delta_e > E_{Fe}$ :

$$n_e = n$$

$$m_{oet}(S) = m_{et} = 0.08152 m_0 \quad (5.3.3)$$

$$m_{oel}(S) = m_{el} = 1.588 m_0 \quad (5.3.4)$$

If the splitting is smaller than the Fermi energy, all four valleys are partially occupied up to  $E_{Fe}$  with  $n_1$  electrons in the lower valley and  $n_2$  in each of the other three. In this situation:

Fig. 5-1

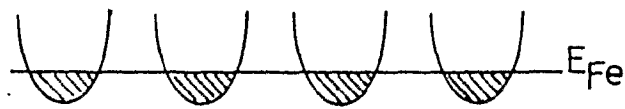
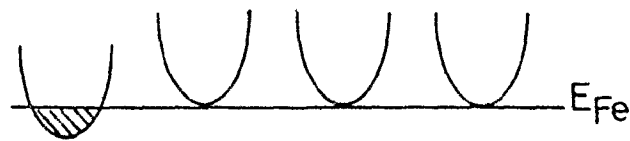
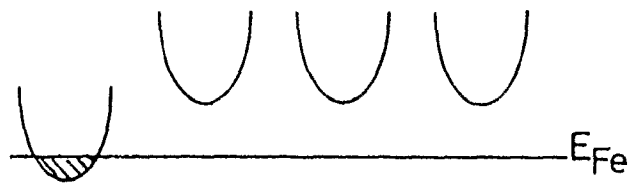
Splitting of the conduction and valence bands for uniaxial compression along the [111] direction in Ge. The ellipsoid along the stress direction is lowered in energy relative to the other three. For a medium stress this splitting is larger than the Fermi energy of the electrons  $E_{Fe}$ , and only one ellipsoid is populated. The balance bands are both populated until stresses near  $7 \text{ kg/mm}^2$  when the splitting between them becomes larger than the hole Fermi energy  $E_{Fh}$ .

Ge  $\langle 111 \rangle$  stress

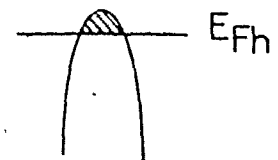
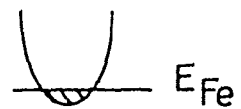
Conduction band

Valence band

Stress 0

Stress  $3 \text{ kg/mm}^2$ Stress  $7 \text{ kg/mm}^2$ 

Infinite stress



$$\frac{n_e}{m_{oet}(S)} = \frac{n_1(S)}{m_{et}} + n_2(S) \left[ \frac{5}{3} \frac{1}{m_{et}} + \frac{4}{3} \frac{1}{m_{el}} \right] \quad (5.3.5)$$

$$\frac{n_e}{m_{oel}(S)} = \frac{n_1(S)}{m_{el}} + n_2(S) \left[ \frac{8}{3} \frac{1}{m_{et}} + \frac{1}{3} \frac{1}{m_{el}} \right]. \quad (5.3.6)$$

If the intervalley relaxation time is small compared to the lifetime of an electron-hole pair, then:

$$n_1 = n \left[ 1 + 3 \left( 1 - \frac{\Delta_e}{E_{Fe}} \right)^{3/2} \right]^{-1} \quad (5.3.7)$$

$$n_2 = n \left( 1 - \frac{\Delta_e}{E_{Fe}} \right)^{3/2} \left[ 1 + 3 \left( 1 - \frac{\Delta_e}{E_{Fe}} \right)^{3/2} \right]^{-1} \quad (5.3.8)$$

The energy eigenvalues of the valence band under stress are discussed in detail in part a) of the appendix. The density of states masses have been calculated as a function of stress by Markiewicz and Kelso (1978) and the optical masses by Kelso (1979). Their results are shown in figures 5-2 and 5-3. The independent variable is  $E/S$  where  $E$  is the energy of the band and  $S$  the stress. These optical masses have been used together with theoretical values of  $E_{Fh}$  to calculate (5.3.1) and (5.3.2).  $n_H$  and  $n_L$  were obtained from the density of states masses of fig. 5-1 using:

$$\left\{ \begin{array}{l} \frac{n_L}{n_H} = \left( \frac{m_{dLh}}{m_{dHh}} \right)^{3/2} \cdot \left( \frac{E_{Fh} - \Delta_h}{E_{Fh}} \right)^{3/2} \quad \text{for } E_{Fh} > \Delta_h \\ \frac{n_L}{n_H} = 0 \quad \text{for } \Delta_h > E_{Fh} \end{array} \right. \quad (5.3.9)$$



Fig. 5-2

Density-of-states masses for heavy and light holes in stressed Ge, as a function of reduced energy  $E/S$ . The arrows indicate the values at zero stress (after Kelso, 1979).

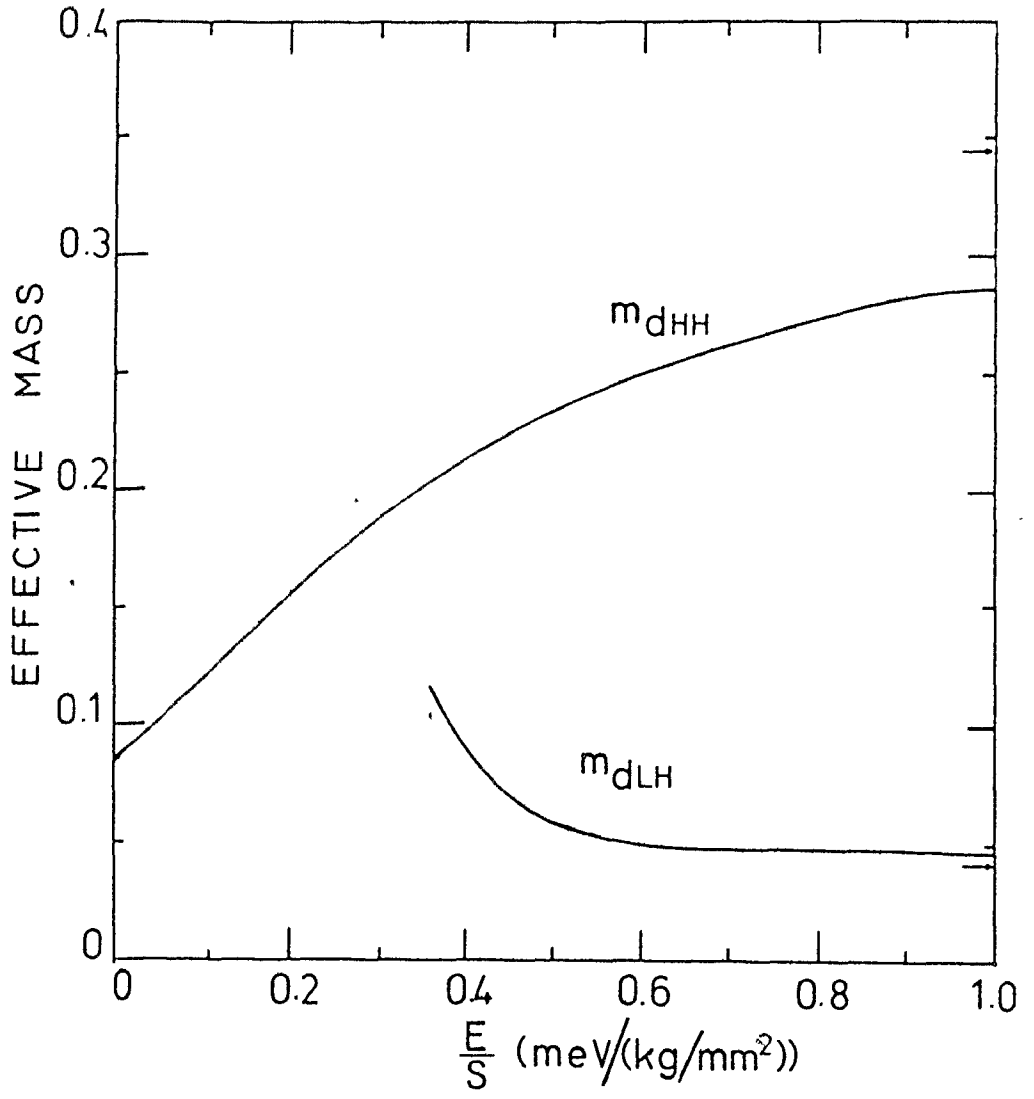
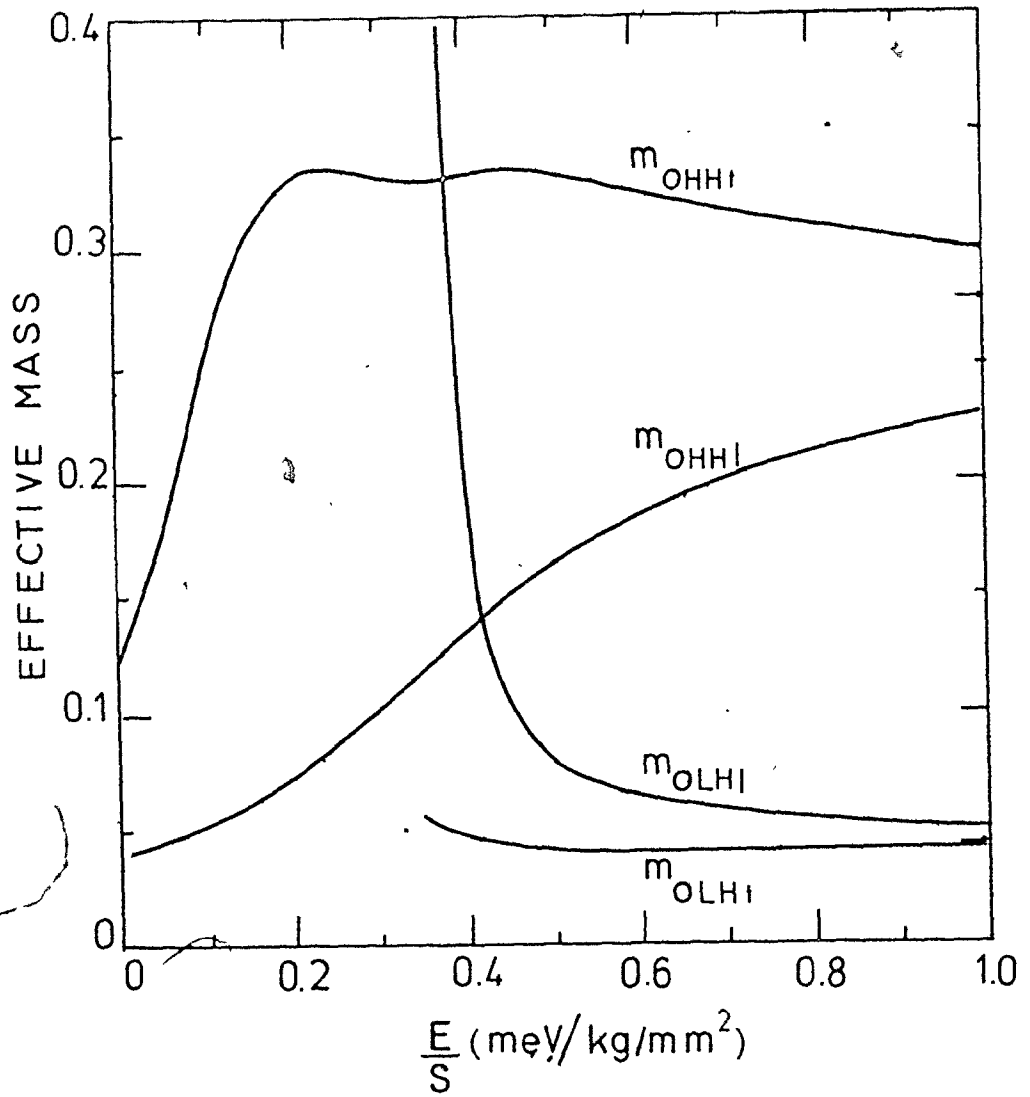


Fig. 5-3

Longitudinal and transverse optical masses for heavy and light holes for [111] stressed Ge, as a function of reduced energy  $E/S$ . The arrows indicate the values at zero stress. (After Kelso, 1979).





where  $\Delta_h$  is the valence band splitting in meV.

From A-10:

$$\frac{\Delta_h}{|S|} = 0.366 \text{ meV}/(\text{kg}/\text{mm}^2) \quad (5.3.10)$$

the interband contribution to the dielectric constant is:

$$\lim_{q \rightarrow 0} \epsilon_{\text{inter}}(q, \omega) = \lim_{q \rightarrow 0} 4\pi e^2 \frac{2}{(2\pi)^3} \int d^3k \frac{(f_{\mathbf{k}}^+ - f_{\mathbf{k}+\mathbf{q}}^-)(E_{\mathbf{k}}^+ - E_{\mathbf{k}+\mathbf{q}}^-)}{(E_{\mathbf{k}}^+ - E_{\mathbf{k}+\mathbf{q}}^-)^2 - \omega(\omega + i\gamma)} \times \frac{|\rho_{\mathbf{k}, \mathbf{k}+\mathbf{q}}^\pm|^2}{q^2} \quad (5.3.11)$$

The energy eigenvalues of the two valence bands  $E^\pm$  are obtained in section b) of the appendix. Their values measured from the vertex of the heavy hole band, for Ge stressed in the [111] direction, are:

$$E^\pm = (-A)k^2 + |E_0| \pm E(k) \quad (5.3.12)$$

and

$$E(k) = [B^2 k^4 + C^2 (k_x^2 k_y^2 + \text{c.p.}) + 4\gamma_3 E_0 (k_x k_y + \text{c.p.}) + E_0^2]^{1/2}$$

where c.p. means cyclic permutation.

The constants A, B and C are given in Table 1.  $E_0 = \frac{\Delta_h}{2}$  is half the valence band splitting at  $k=0$  given in table 3, and

$$\gamma_3 = \frac{1}{2\sqrt{3}} (3B^2 + C^2)^{1/2}$$

The matrix elements  $\rho_{\mathbf{k}, \mathbf{k}+\mathbf{q}}^\pm$  depend on the polarization direction  $\hat{q}$ , a calculation of their value to second order in  $q$

Table 3  
Parameters used in Ge [111] calculations

Parameter	Value	Reference
$D'_u$ (deformation potential)	$(3.81 \pm 0.25)$ eV	a
$S_{44}$ (elastic constant)	$1.443 \times 10^{-4}$ mm <sup>2</sup> /kg	b
$\frac{\Delta_e}{ S }$ (conduction band splitting at $k=0$ )	$1.05$ meV/kg/mm <sup>2</sup>	c
$\frac{\Delta_h}{ S }$ (valence band splitting at $k=0$ )	$0.366$ meV/kg/mm <sup>2</sup>	d
$m_{ht}$ (infinite stress hole transverse mass)	$0.130$ m	e
$m_{h\ell}$ (infinite stress long. mass)	$0.040$ m	e
$m_{dh}^m$ (infinite stress density of state mass)	$0.080$ m	e

a Hensel and Suzuki, 1974

b) taken from Ch. Kittel (4th edition)

c)  $\frac{\Delta_e}{|S|} = \frac{4}{9} \theta_\mu S_{44}$  with  $\theta_\mu = 16.6$  eV (I. Balslev, 1966)

d)  $\frac{\Delta_h}{|S|} = \frac{2}{3} D'_u S_{44}$

e) In the high stress limit the hole bands are ellipsoidal with longitudinal and transverse mass given by

$$\frac{m_{h\ell}}{m} = \left( A + \frac{1}{2} \sqrt{\frac{3B^2 + C^2}{3}} \right)^{-1}$$

$$\frac{m_{ht}}{m} = \left( A - \frac{1}{2} \sqrt{\frac{3B^2 + C^2}{3}} \right)^{-1}$$

is given in section d) of the appendix for [111] stressed Ge.

$$\rho^{\pm}(\bar{k}, \bar{k}+\bar{q}) = \frac{1}{2E^2(k)} [F_2(\bar{k}, \bar{q}) - \frac{F_1^2(\bar{k}, \bar{q})}{E^2(\bar{k})}] \quad (5.3.14)$$

with

$$F_1 = q\{12(\gamma_2^2 - \gamma_3^2)[k_x^3 \hat{q}_x + k_y^3 \hat{q}_y + k_z^3 \hat{q}_z] + (12\gamma_3^2 - 4\gamma_2^2)k^2(k_x \hat{q}_x + \text{c.p.}) \\ + 2\gamma_3 \epsilon_0 [(\hat{q}_x + \hat{q}_y + \hat{q}_z)(k_x + k_y + k_z) - (\hat{q}_x k_x + \text{c.p.})]\} \quad (5.3.15)$$

$$F_2 = q^2\{24(\gamma_2^2 - \gamma_3^2)(k_x^2 k_y^2 + \text{c.p.}) + 12\gamma_3^2 k^2 q^2 + (12\gamma_3^2 - 8\gamma_2^2)(k_x \hat{q}_x + \text{c.p.})^2\} \quad (5.3.16)$$

$$\bar{q} = q(\hat{q}_x, \hat{q}_y, \hat{q}_z) .$$

Figures 5-4 and 5-5 show the result of computing the imaginary part of the interband dielectric constant from eqs. (5.3.11) to (5.3.16), for several stress values and hole Fermi energies at  $T=0$ . Figure 5-4 corresponds to the polarization parallel to the stress direction ( $\bar{q} = \frac{1}{\sqrt{3}}, \frac{1}{\sqrt{3}}, \frac{1}{\sqrt{3}}$ ), and Fig. 5-5 to perpendicular polarization ( $\bar{q} = \frac{1}{\sqrt{2}}, -\frac{1}{\sqrt{2}}, 0$ ). It can be seen that, for the same stress values and Fermi energies, the longitudinal dielectric constant is larger than the transverse one. Increasing stress value decreases  $\text{Im}(\epsilon_{\text{inter}})$  considerably, as the two valence bands separate. Thus at high stresses the relative importance of the interband contribution decreases and the intra-band plasma peak dominates the absorption.

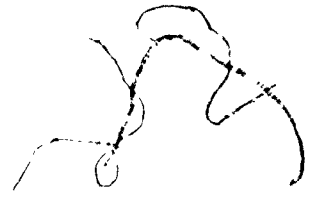


Fig. 5-4

Imaginary part of the interband dielectric constant for several stress values for light polarized parallel to the stress direction. The stress values ( $S$ ) are given in  $\text{kg/mm}^2$  and the hole Fermi energies  $E_F$  in  $\text{meV}$ . In these calculations the interband damping has been assumed very small as compared to the Fermi energy.

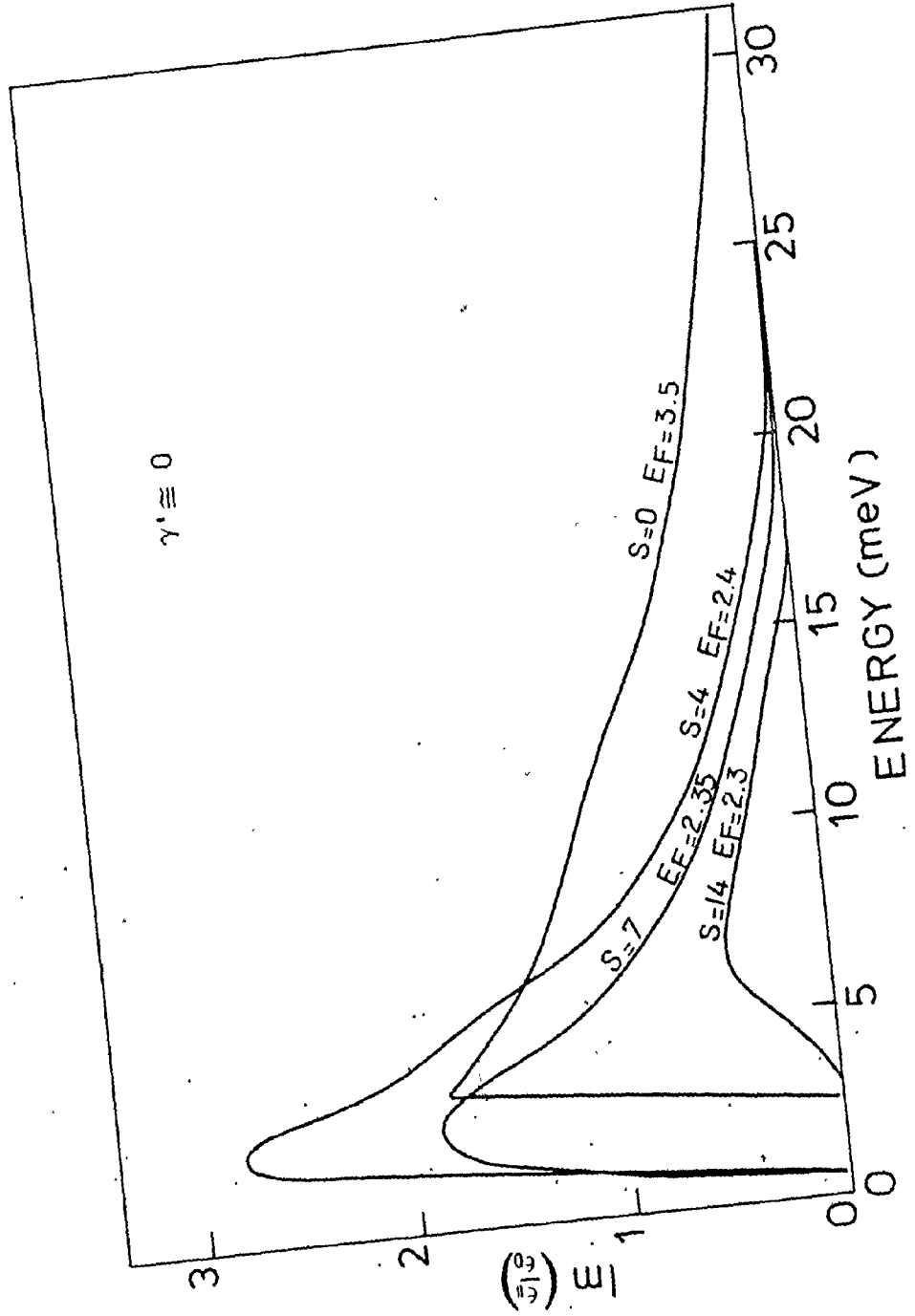
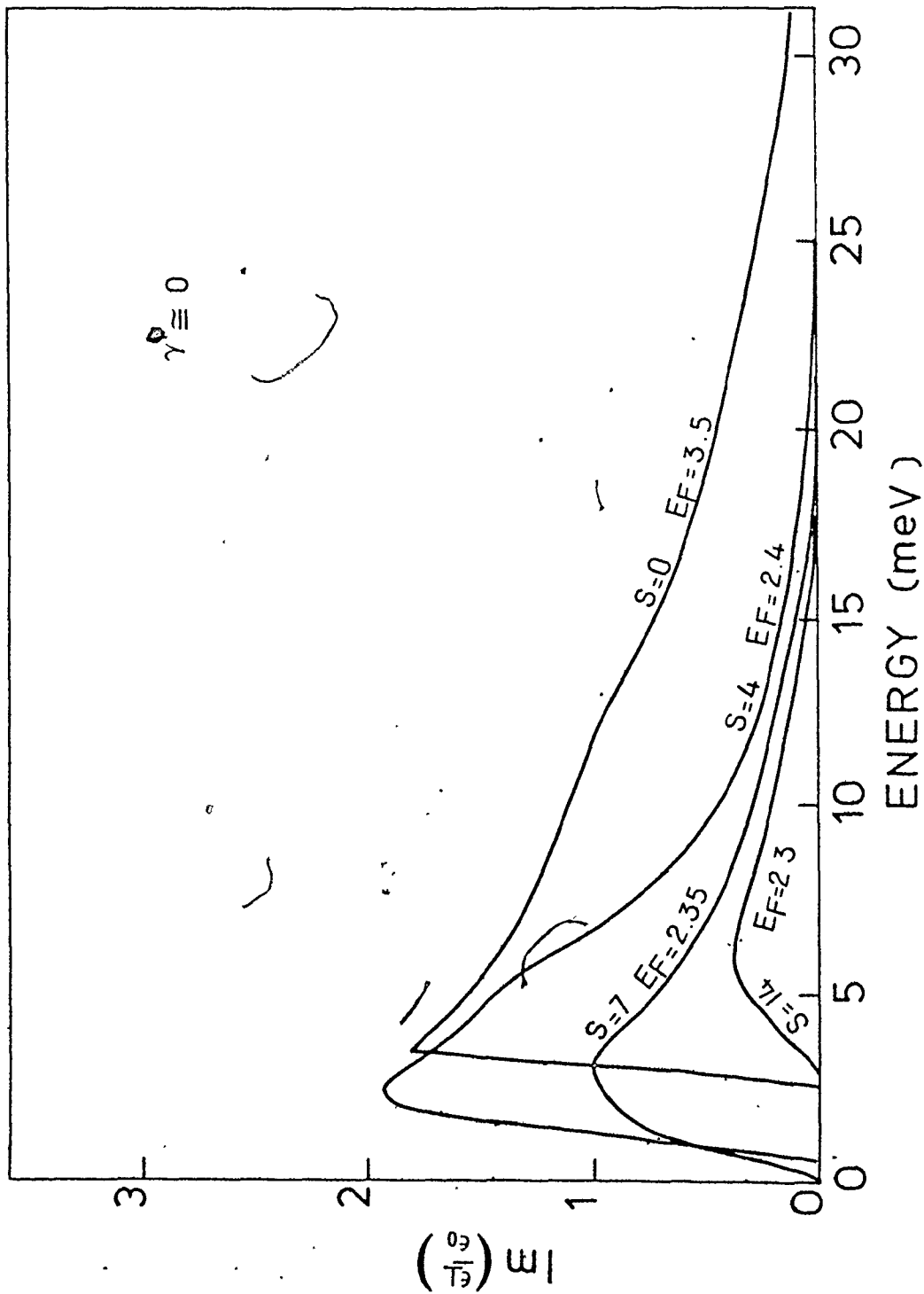


Fig. 5-5

Imaginary part of the interband dielectric constant for several stress values for light polarized perpendicularly to the stress direction. The stress values (S) are given in meV. The figure corresponds to interband damping  $\gamma' \sim 0$ .





#### 5.4 Experimental Results and Discussion

##### a) Electric field of the incoming radiation perpendicular to the stress direction ( $\vec{E} \perp \vec{S}$ )

Figures 5-6, 5-7 and 5-8 show the measured absorption spectra of light polarized along  $[1\bar{1}0]$  by EHD in pure Ge stressed along  $[111]$ . Fig. 5-6 corresponds to a stress of  $2 \text{ kg/mm}^2$ , fig. 5-7 to  $5 \text{ kg/mm}^2$  and 5.8 to  $10 \text{ kg/mm}^2$ . These experiments were performed with the sample immersed in a He bath at a temperature of  $1.2^\circ\text{K}$ . Data on fig. 5-6 and 5-8 have been taken at similar laser power, fig. 5-7 with approximately 30% less. At  $2 \text{ kg/mm}^2$  the lineshape is very similar to non stressed Ge and the line peaks at around the same value as at zero stress. The main difference between both cases is that  $\alpha_{\text{max}}$  is smaller for  $S=2$  than for  $S=0$ ; in some of the experiments there is almost a factor of two difference between the two cases. These features do not change up to a stress value of about  $2.5 \text{ kg/mm}^2$ . Between  $2.5$  and  $3 \text{ kg/mm}^2$  there is a dramatic shift of the line towards lower frequencies. At  $5 \text{ kg/mm}^2$  (figure 5-7), the line peaks at  $(5.6 \pm 0.1) \text{ meV}$ , is narrower and more symmetric than  $S=0$ . When the stress is increased further, the line continues to narrow and shifts slowly towards lower frequencies. At  $11 \text{ kg/mm}^2$  (figure 5-8)  $\alpha_{\text{max}}$  occurs at  $\omega = (4.3 \pm 0.1) \text{ meV}$ . At the same laser power  $\alpha_{\text{max}} (S=11) > \alpha_{\text{max}} (S=5)$ .

Figure 5-9 gives the change of resonance frequency for perpendicular polarization ( $\omega_{0\perp}$ ) as a function of stress. The

Fig. 5-6

Far-infrared absorption spectrum of EHD in Ge under small uniaxial stress for light polarized perpendicularly to the stress direction. The observed spectrum is similar to unstressed Ge, the main differences are a broadening of the line, specially at low frequencies, and a smaller value of the absorption at the maximum.

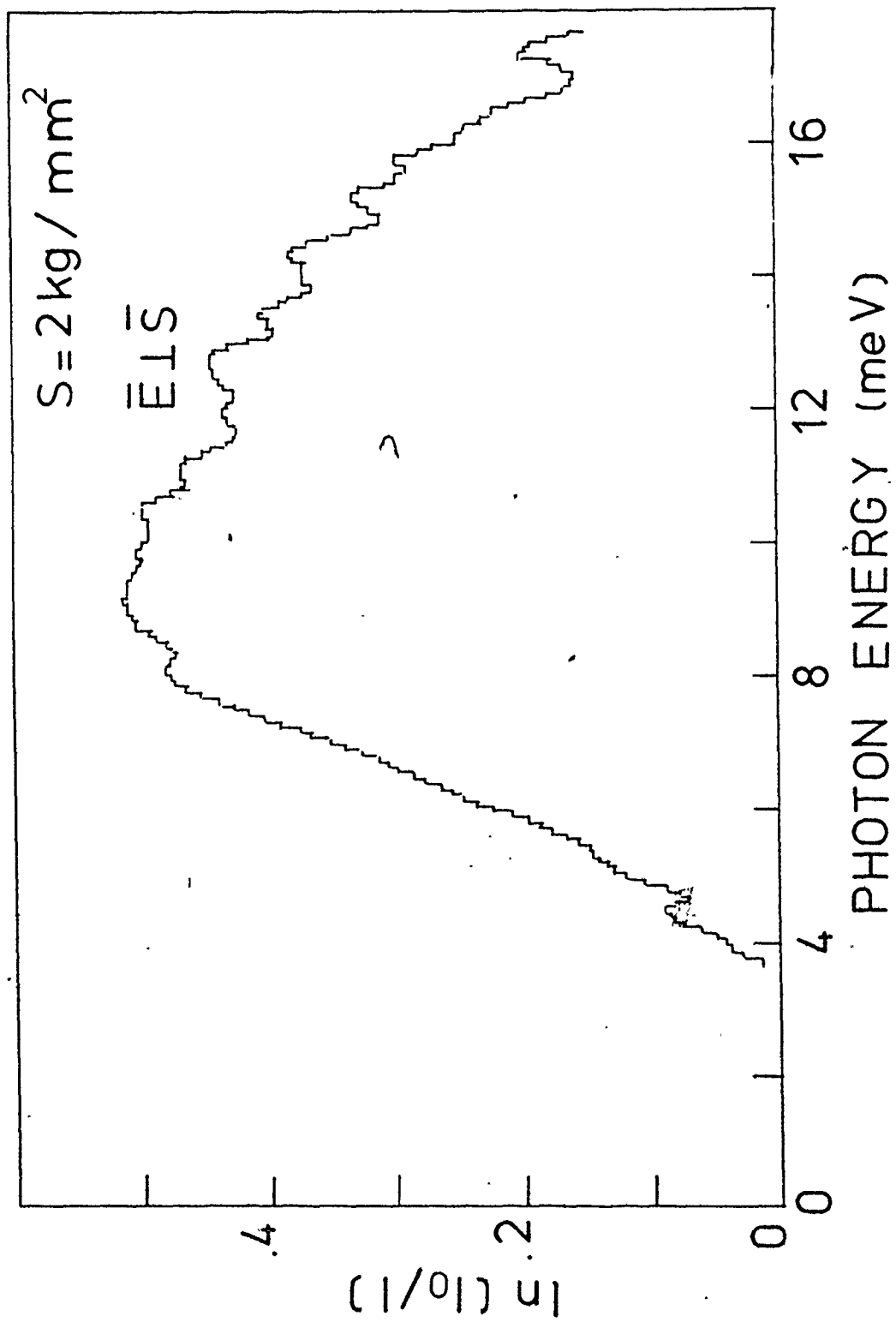


Fig. 5-7

Far-infrared absorption spectrum of EHD in Ge under intermediate uniaxial stress along [111] for light polarized along  $[1\bar{1}0]$ . The data shown corresponds to  $5 \text{ kg/mm}^2$  and  $1.2^\circ\text{K}$ . Note that the plasma peak has moved from its unstressed position at 9 meV to near 6 meV.

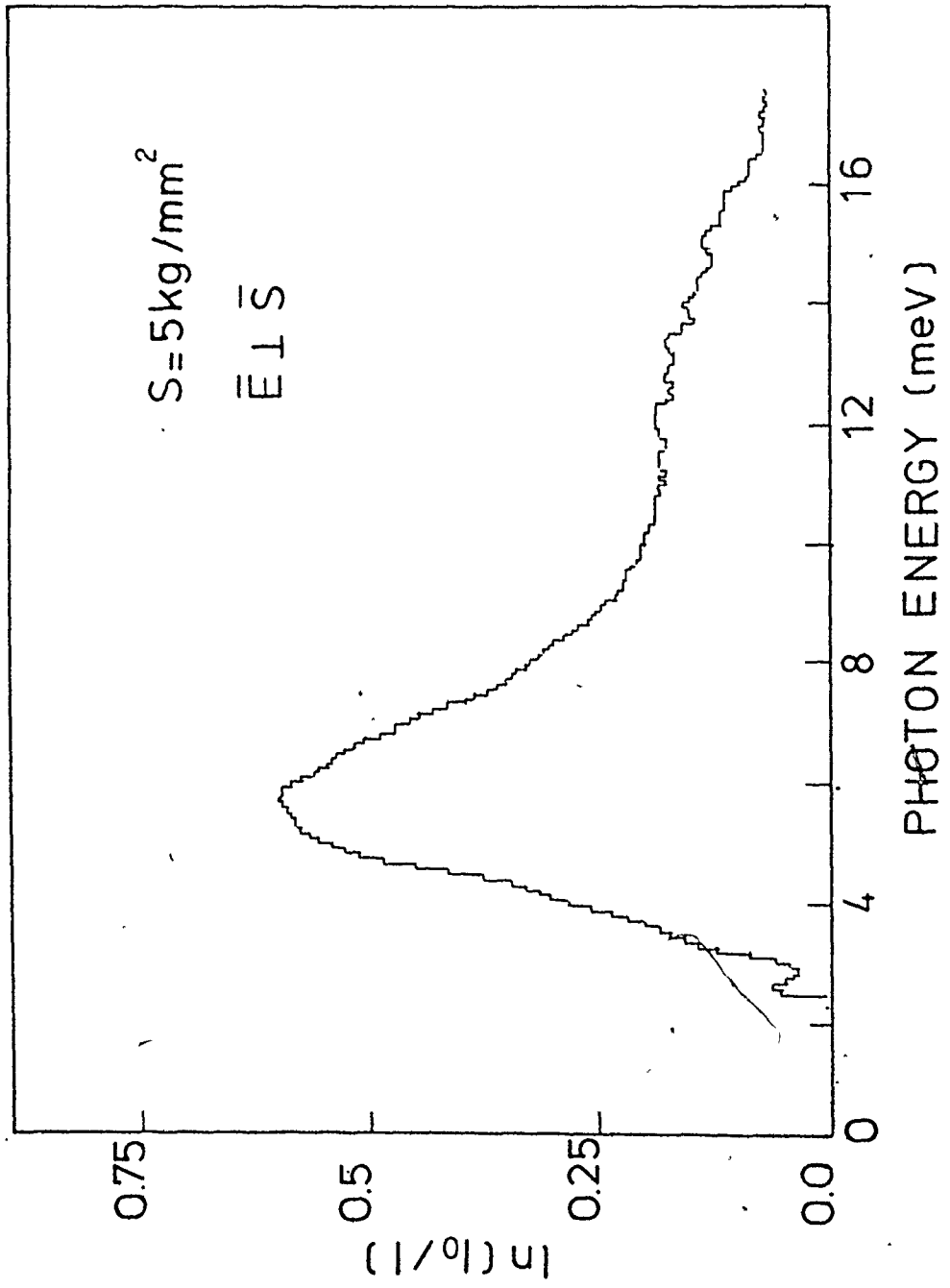


Fig. 5-8

Far-infrared absorption spectrum of EHD in Ge under 11 kg/mm<sup>2</sup> of [111] stress for light polarized along [1 $\bar{1}$ 0]. The plasma peak is close to 4 meV; the absorption at high frequencies is smaller relative to its value at the maximum than for small or medium stresses.

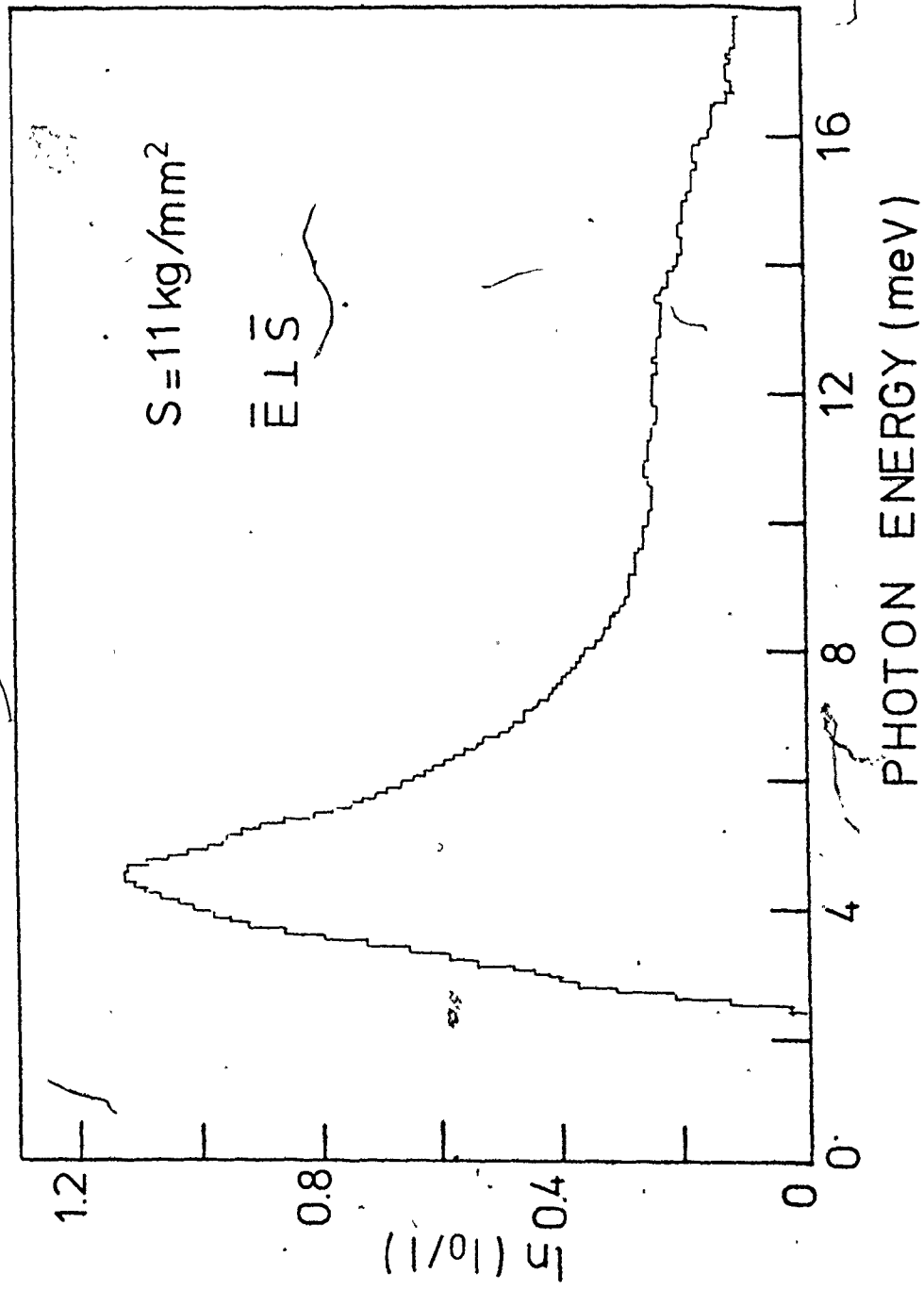
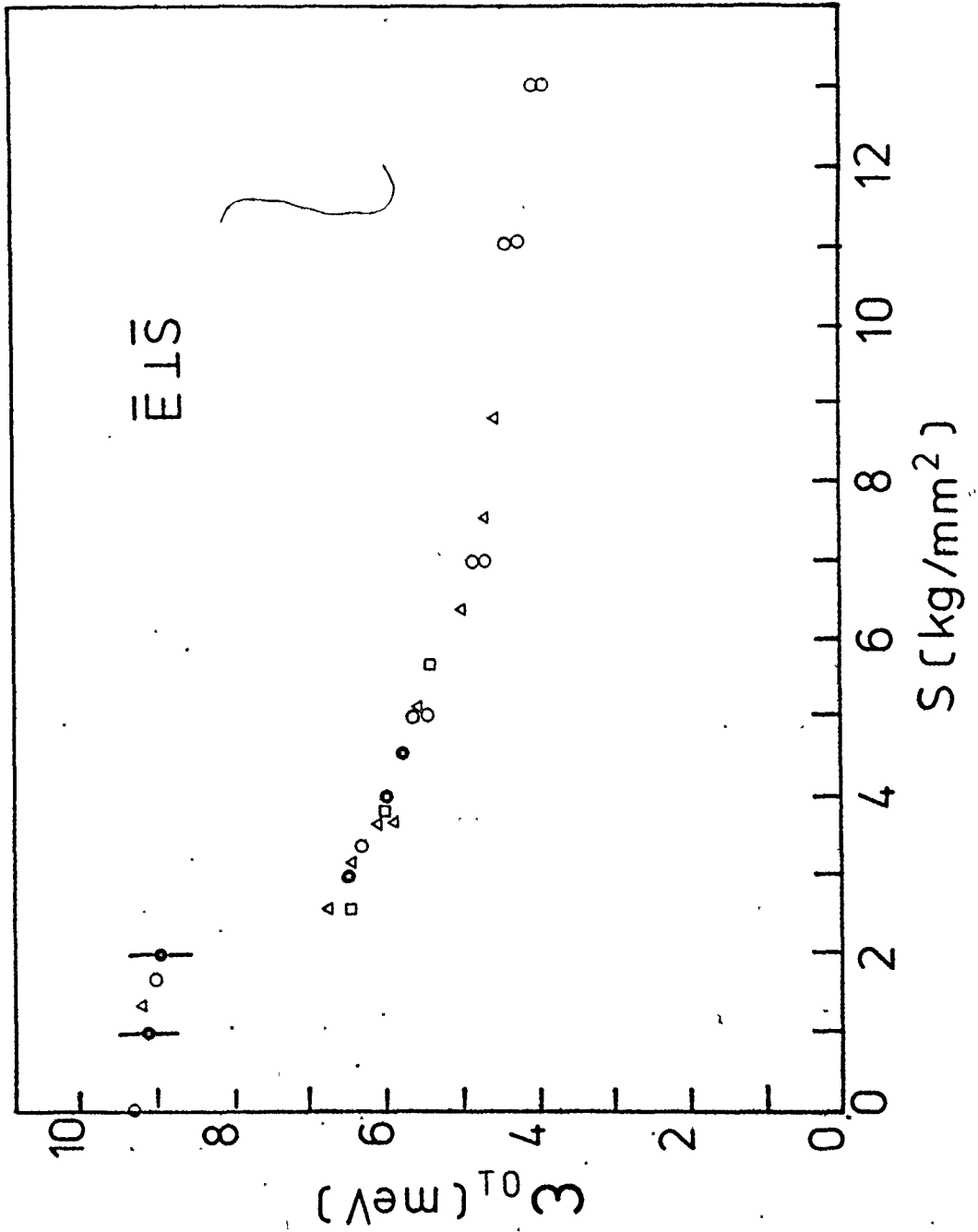


Fig. 5-9

Plasma resonance frequency of electron-hole drops for infrared light polarized perpendicularly to the stress direction as a function of stress, at 1.2°K. The different symbols in the figure correspond to different runs; the squares and dark circles have been obtained with a different sample. The sharp decrease in  $\omega_{0\perp}$  occurs when the upper conduction valleys empty.





different symbols in the figure correspond to different sets of experiments. The most striking feature in the figure is the strong decrease in  $\omega_{0\perp}$  at  $S_E = 2.5 \text{ kg/mm}^2$ . For  $S < S_E$ ,  $\omega_{0\perp}$  is approximately a constant 9 meV; for  $S > S_E$   $\omega_{0\perp}$  decreases slowly from 6.5 meV to 3.8 meV at  $13 \text{ kg/mm}^2$ . These changes in  $\omega_{0\perp}$  can be explained in terms of the variations of electron-hole pair density and effective masses that occur when the Ge band structure is altered by [111] stress. For small stress, when the conduction band splitting is smaller than  $E_{Fe}$ , the upper valleys are partially populated and the electrons perpendicular optical effective mass (when averaged over the valleys) decreases from its  $S = 0$  value to the much smaller one that occurs when only one ellipsoid is occupied (see eqs. (5.3.5), (5.3.7) and (5.3.8)). At these stresses the hole effective masses are almost constant and equal to their zero stress values (fig. 5-3). The change in  $m_{et}$  should shift the line towards higher frequencies. The fact that  $\omega_{0\perp}$  does not change clearly indicates a slight decrease of the electron hole pair density in this region. At a stress very close to, but smaller than  $S_E$  the best fit to the line that peaks at 9 meV with the theory of sections 5.2 and 5.3 can be obtained with an electron-hole pair density of  $(1.5 \pm 0.2) \times 10^{17} \text{ cm}^{-3}$  in agreement with the calculations of Kirczenow and Singwi. The large error limits reflect the uncertainty of the damping at this stress which was taken as an adjustable parameter. We have seen in section 3.4

that  $\gamma$  shifts the peak position affecting the estimation of the density.

The sharp decrease in  $\omega_{0\perp}$  at around  $3 \text{ kg/mm}^2$  is consistent with the change in the equilibrium density expected when the upper conduction valleys empty and only the lower valley remains occupied. This change occurs when  $E_{Fe} = \Delta_e$  and theoretical models predict it at stresses between  $2.5$  and  $3 \text{ kg/mm}^2$  (Kelso, 1979; Kirczenow and Singwi, 1979). Our experimental value of  $S_E$  is somewhat uncertain, due to problems in knowing the zero of the stress calibration. But even if the value is not known accurately, it is certain that the transition between four valleys and one valley occupied (Ge(4,2) and Ge(1,2) respectively), occurs within less than  $0.5 \text{ kg/mm}^2$ .

The further decrease in  $\omega_{0\perp}$  for  $S > S_E$  reflects the variation in equilibrium density ( $n$ ) produced by the splitting and deformation of the valence bands. At these stresses, the absorption of light with  $\vec{E} \perp \vec{S}$  is a good probe for the study of density variations, since changes in the hole effective masses and interband transitions are not very important in this polarization. The main contribution to  $\omega_{0\perp}$  comes from the electrons due to the small value of  $m_{e\perp}$  (see table 3). The non parabolicity and change with stress of the hole effective masses is then masked by the large value of the electron contribution to the plasma frequency. Since the conduction bands do not deform with stress  $\omega_{\perp\text{plasma}}^2$  is approximately proportional to  $n$ .

As in non-stressed Ge, the position of the resonance peak changes from its Drude value  $\omega_p/\sqrt{3}$  due to damping and interband transitions (eqs. (3.4.11) and (3.4.20)). The latter ones become less important for high stress (fig. 5-5), producing an increasing symmetry and narrowing of the line.

The solid line in fig. 5-10 shows the result of a calculation of  $\sigma_{\perp}$  with the theory of sections 5.2 and 5.3 for a stress of  $7 \text{ kg/mm}^2$ . The experimental data correspond to the same stress value; the peak position at 4.9 meV and overall fit agrees with the parameters  $n = 0.47 \times 10^{17} \text{ cm}^{-3}$  and  $\gamma = 1.5 \text{ meV}$ , used to calculate the theoretical line.

Table 4 gives the peak positions for several stress values and the electron hole pair density calculated from  $\omega_{0\perp}$  corrected for the intraband damping and interband transition contributions. The values of  $\gamma$  necessary to fit the curves at  $S > S_E$  are generally around 1.5 meV. The experimental results agree very well with the theoretical values of Kirczenow and Singwi except at just above  $S = S_E$ , for example at  $S = 3$ , the electron-hole pair density is somewhat larger than the theoretical value of .67. Our measurements agree very well with the last luminescence results of Chou and Wong (1978) for  $S > S_E$ ; for  $S < S_E$  unlike us, they report a continuous decrease of  $n$  with increasing stress.

In order to estimate the density of the electron-hole

Fig. 5-10

Absorption spectrum of electron-hole drops in Ge under [111] stress and perpendicular polarization. The experimental curve was obtained with a stress of  $7 \text{ kg/mm}^2$  at  $1.2^\circ\text{K}$ . The filled line is a theoretical calculation with the theory described in the text for the same stress value and a density of  $0.47 \times 10^{17} \text{ cm}^{-3}$ . The damping constant was chosen to fit the linewidth.

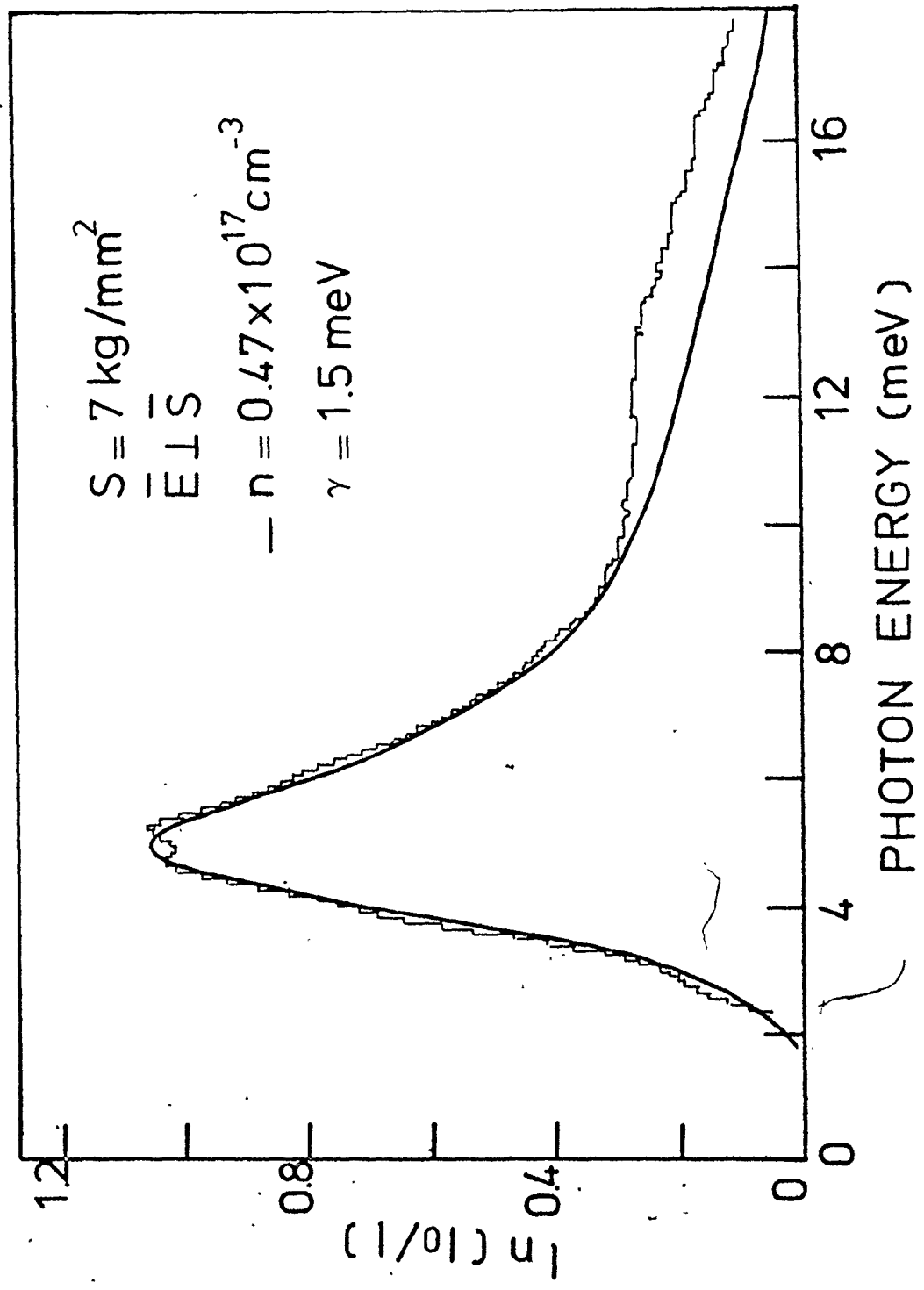


Table 4

Perpendicular plasma frequency and density  
for selected stress values

<u>Stress (kg/mm<sup>2</sup>)</u>	<u><math>\omega_{0\perp}</math> (meV)</u>	<u><math>n (\times 10^{17} \text{ cm}^{-3})</math></u>
0	9.3±0.1	2.02±0.05
2.5	9 ±0.2	1.5 ±0.2
3	6.7±0.3	0.75±0.06
4.5	6.1±0.2	0.62±0.04
5.5	5.5±0.2	0.55±0.03
7	5.0±0.2	0.46±0.03
10	4.2±0.1	0.35±0.02
13	3.9±0.1	0.30±0.01
20	3.4±0.2	0.24±0.02
∞	2.6±0.2	0.11±0.02

fluid at infinite stress, an extrapolation of  $\omega_{0\perp}^2$  as a function of  $\frac{1}{S}$  for  $\frac{1}{S} \rightarrow 0$  is used. Figure 5-11 shows the points for  $S > 4 \text{ kg/mm}^2$  ( $\frac{1}{S} < 0.25 \text{ mm}^2/\text{kg}$ ). It can be seen that  $\omega_{0\perp}^2$  is linear within error limits with  $\frac{1}{S}$  and the intercept at  $\frac{1}{S} = 0$  corresponds to  $\omega_{0\perp}^2(\infty) = (7 \pm 1) (\text{meV})^2$ . Using the infinite stress masses of table 3 an electron hole pair density  $n_{\infty} = 0.105 \pm 0.015 \times 10^{17} \text{ cm}^{-3}$  is obtained in good agreement with theoretical calculations (Vashishta et al, 1974).

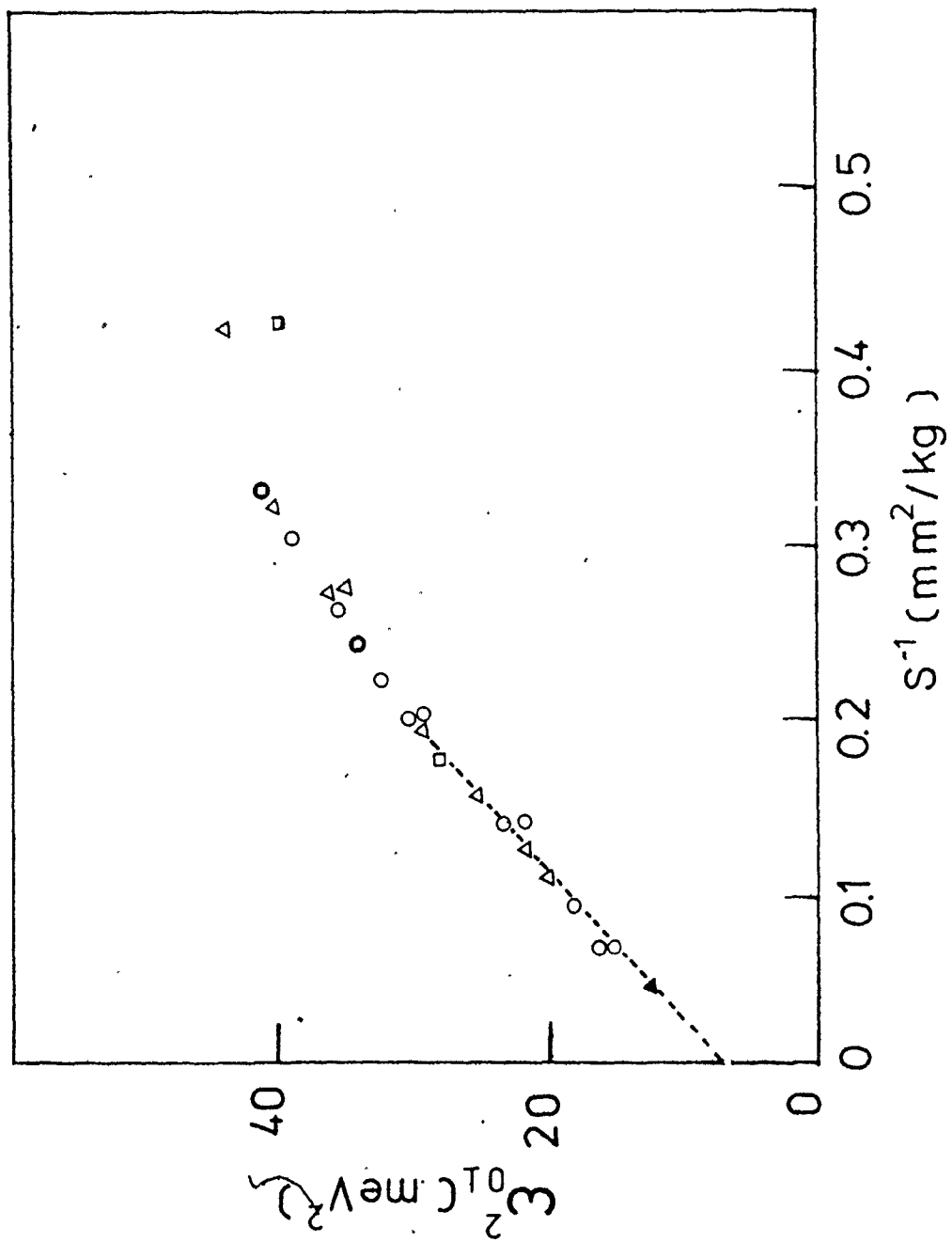
b) Electric field of the incoming radiation parallel to the stress direction ( $\vec{E} \parallel \vec{S}$ )

Figure 5-12 shows the plasma resonance for  $\vec{E} \parallel \vec{S} \parallel [111]$  and at a stress of  $1.5 \text{ kg/mm}^2$ . It can be seen that, unlike the case of perpendicular polarization, the line shifts towards lower frequencies for very small stress. The reason for this shift is twofold: a slight decrease in density and the strong increase in electron optical effective mass when the upper conduction valleys become depopulated (eqs. (5.3.6) to (5.3.8)) lower the plasma frequency. Assuming zero intervalley relaxation time and correcting for intraband damping,  $\omega_{0\parallel} = 7.5 \text{ meV}$  for  $S = 1.5 \text{ kg/mm}^2$  gives  $n = 1.93 \times 10^{17} \text{ cm}^{-3}$  of which  $1.13 \times 10^{17} \text{ cm}^{-3}$  are in the lower valley and  $0.80 \times 10^{17} \text{ cm}^{-3}$  in the three upper valleys. The lineshape remains similar to the zero stress case since the interband contribution is about the same. At stress values between 3 and  $5 \text{ kg/mm}^2$  lines similar to figure 5-13 are observed. The absorption is generally weaker than at



Fig. 5-11

Square of the perpendicular resonance frequency as a function of reciprocal stress values. At small values of  $S^{-1}$  a linear relationship is observed with an extrapolated value of  $\omega_{0\perp}^2 = 7 \text{ meV}^2$  at  $\infty$  stress. The different symbols in the figure correspond to different runs.



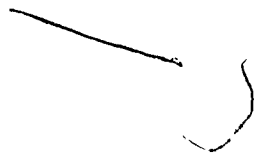


Fig. 5-12

Far-infrared absorption of EHD in Ge with  $1.5 \text{ kg/mm}^2$  of stress along [111] and parallel polarization. Even small stress values shift the plasma peak with respect to its zero stress position when the light is polarized parallel to the stress direction. The shift is mostly produced by the change in electron optical mass.

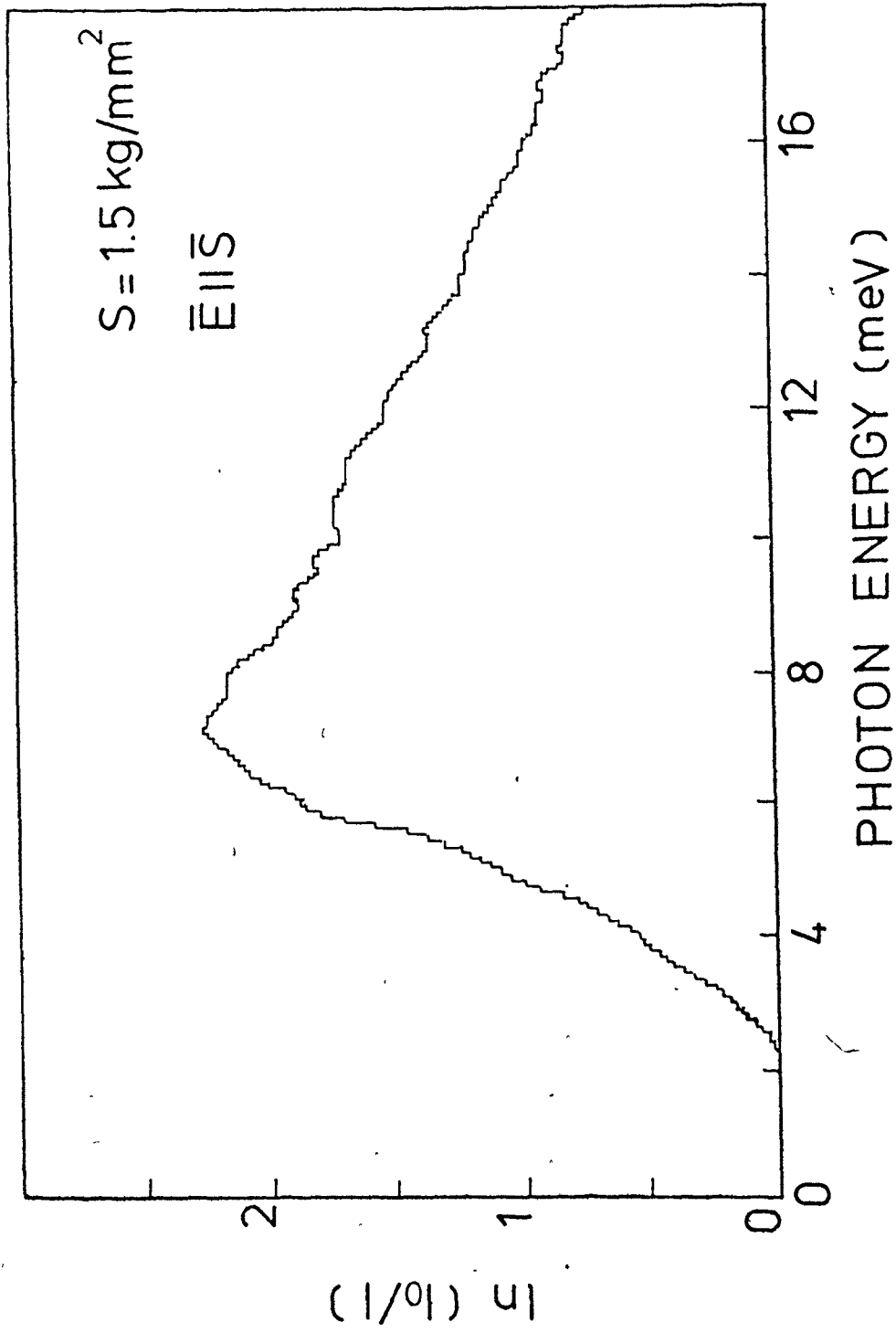
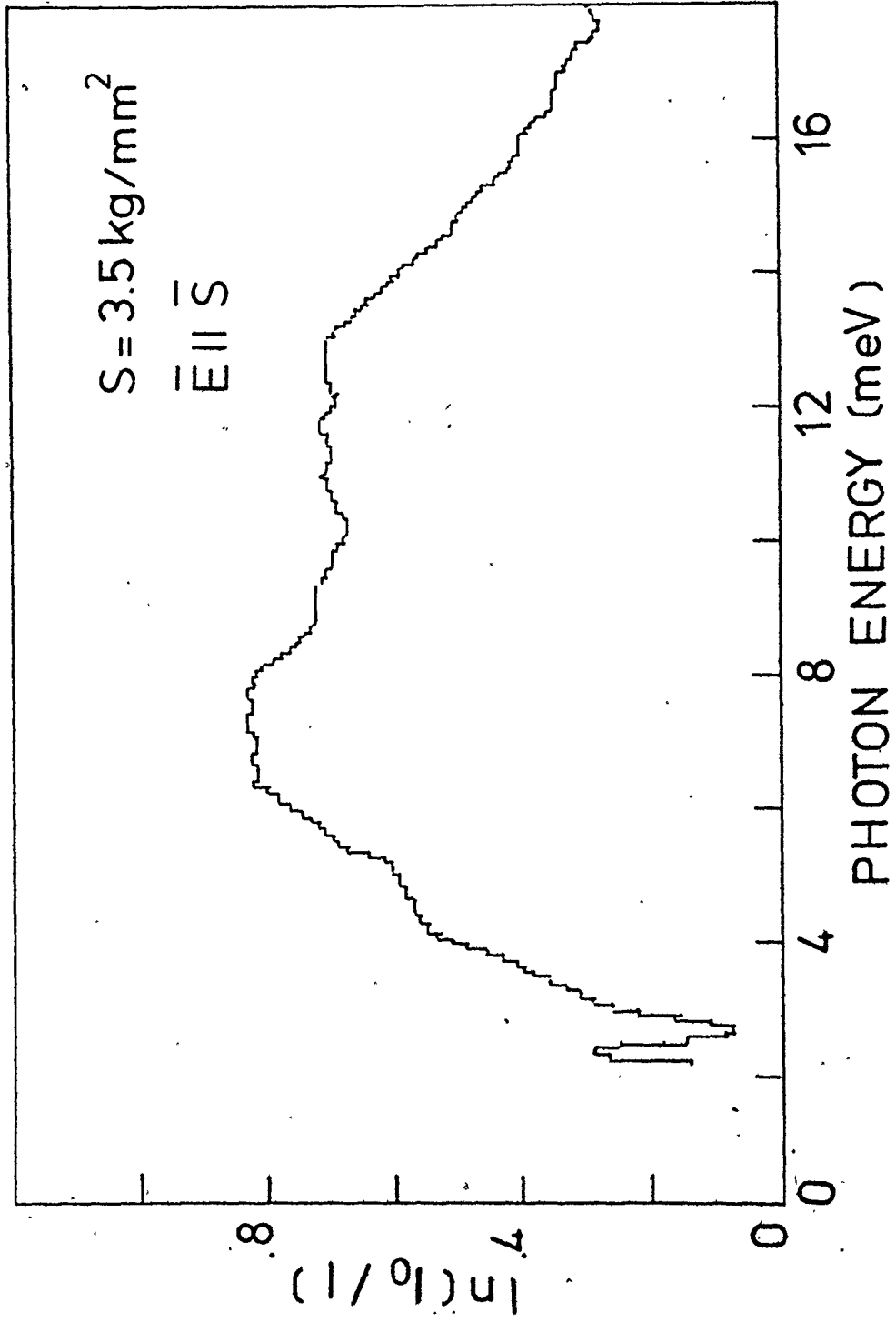


Fig. 5-13

Far-infrared absorption of EHD in Ge with  $3.5 \text{ kg/mm}^2$  of stress along [111] and parallel polarization. The broad line around 7 meV corresponds to interband transitions, the plasma peak is near 4 meV. The absorption at 12 meV can not be explained with the presented theory and is discussed in the text.

2



lower stress or than with perpendicular polarization. At these stress values, assuming  $n \sim 0.6 \times 10^{17} \text{ cm}^{-3}$  gives  $\frac{\omega_{p||}}{\sqrt{3}}$  3 or 4 meV but a peak seldom appears at these frequencies. Generally the broad line around 6 or 7 meV obscures any other features.

This broad line is produced by the interband transitions. As shown in figures 5-4 and 5-5 the contribution to the dielectric constant of the interband transitions is larger for the parallel configuration than for the perpendicular. This effect is emphasized by the plasma absorption which is decreased considerably by a factor of  $\frac{\omega_{p||}^2}{\omega_{p\perp}^2}$ .

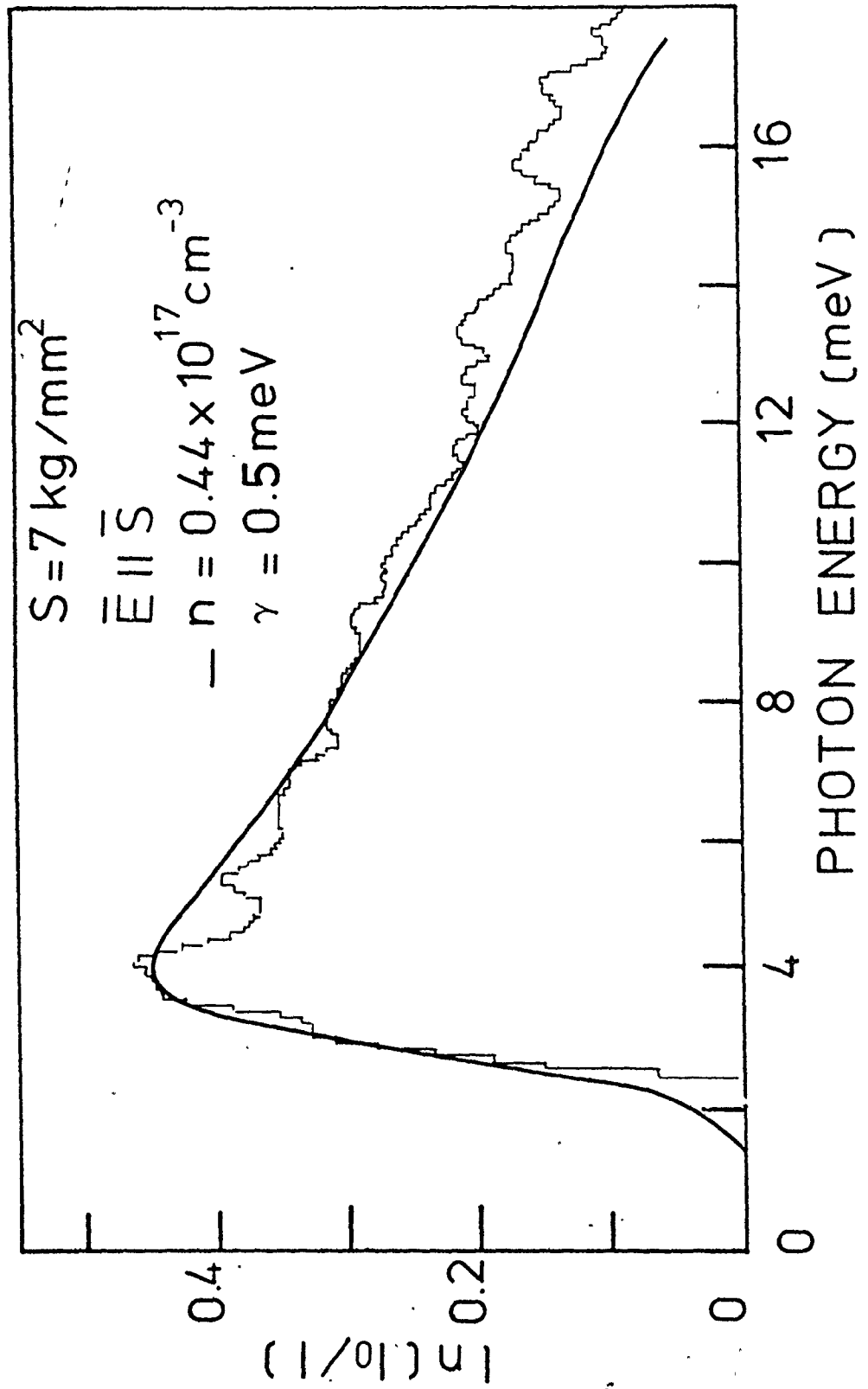
The shoulder between 10 and 12 meV cannot be explained with this theory and will be discussed in the next section.

At  $7 \text{ kg/mm}^2$  the plasma peak is again visible, as can be seen in fig. 5-14, even if the interband transitions are still strong and the line asymmetric. A good theoretical fit to the experiment is obtained for a density of  $(.44 \pm 0.02) \times 10^{15} \text{ cm}^{-3}$  in agreement with the observed values for  $\bar{E}_{\perp} \bar{S}$ , and a damping constant of 0.5 meV. The asymmetry disappears at higher stresses due to the decrease of the interband transitions, and for  $S \sim 11 \text{ kg/mm}^2$  the line resembles  $\sigma_{\perp}$  since there is a slight increase of  $\omega_{p||}$  produced by the decrease in  $m_{oh||}$ .

Fig. 5-14

Absorption spectrum of electron-hole drops in Ge under  $7 \text{ kg/mm}^2$ , [111] stress and parallel polarization. The solid line is a calculation with the theory described in the text for the same stress value as the experimental data and a density of  $0.44 \times 10^{17} \text{ cm}^{-3}$ . A damping constant of 0.5 meV was chosen to fit the experiment.





### 5.5 Summary and Conclusions

It was shown in the last section that the far infrared absorption lineshapes of electron-hole drops in Ge under stress can be successfully explained in terms of intraband and interband transitions in the stress modified bands. These bands are occupied by electrons and holes with a density that agrees in most cases with calculated values for EHD in Ge under [111] stress.

The most important assumptions of the model used to fit the experimental results is that the EHD remain spherical under uniaxial stress and with a radius much smaller than the wavelength in the outside medium (dipolar absorption). This hypothesis is justified by the experimental results. No important variation of the lineshape with absorbed power was detected and there is a usual linear dependence between  $\alpha_{\text{max}}$  and the exciting laser power. It is well known that drops increase in size with generation rate. If the drop size were comparable with the wavelength, the absorption lineshape would be strongly affected by the change in laser power. The fact that this does not occur seems to support the assumption of small drops. Besides, the resonant frequency of large size drops would have been strongly shifted towards lower energies and additional structure would have been present in the absorption line. These effects were not observed and the good agreement between the experimental and expected values of  $n$  shows that there are no large shifts of the plasma line.

The assumption of sphericity is supported by the good agreement between densities obtained fitting lines with parallel and perpendicular polarization. If anisotropic surface tension produced elliptical drops then eq. (5.2.2) would not apply. The correct expressions for parallel and perpendicular polarization would be quite different and the use of (5.2.2) would yield different results for  $n$  if applied to the absorption of perpendicular or parallel polarized light.

An observation that remains unexplained by the theory is the larger than expected absorption in the region 9 - 14 meV, where a clear shoulder appears. This effect can be seen in figures 5-7, 5-8 and 5-10 for  $\sigma_{\perp}$  and in fig. 5-13 for  $\sigma_{\parallel}$ . There is some evidence that this absorption is produced by the presence of hot electrons in the system. It has been assumed here that for  $S > S_E$  the upper conduction valleys are empty; this is not always the case. Chou et al (1977) showed that at intermediate stress values in very pure, homogeneously stressed crystals, these valleys are partially occupied by electrons with a lifetime comparable with that of the "cold" electrons and they detect their presence in the electron-hole liquid. Kirczenow and Singwi (1978) proposed that when the concentration of these hot electrons is not very high, an additional liquid phase of higher density containing hot and cold electrons could form. The absorption by a coated sphere with a central high density phase and a coating of the normal "cold" liquid

could explain our results (Timusk and Zarate, 1981), but further studies are required in order to confirm the existence of this controversial second phase.

CHAPTER 6  
CONCLUSIONS

The study of the absorption of far-infrared radiation by electron-hole drops is a powerful tool in the understanding of its properties.

The threshold and cutoff of the absorption line are related to the Fermi energy, and the peak position to the plasma frequency, allowing the determination of three independent values of the electron-hole density in the fluid with the same experimental technique. The peak position, the easiest of these values to measure, is affected by the interband transitions and intraband damping. Calculations of these quantities were needed to give an accurate value of the density as well as to understand the general line shape.

The plasma oscillations are heavily damped as is apparent from the width of the line. This damping, produced by electron-hole collisions, is strongly frequency dependent. At frequencies less than the Fermi energy it is small enough as to allow the existence of a sharp threshold at the onset of the interband transitions. Near the plasma peak it is at least one order of magnitude larger. It is found that the main contribution to this damping comes from electrons that collide with holes in the heavy-hole band. The contributions from the scat-

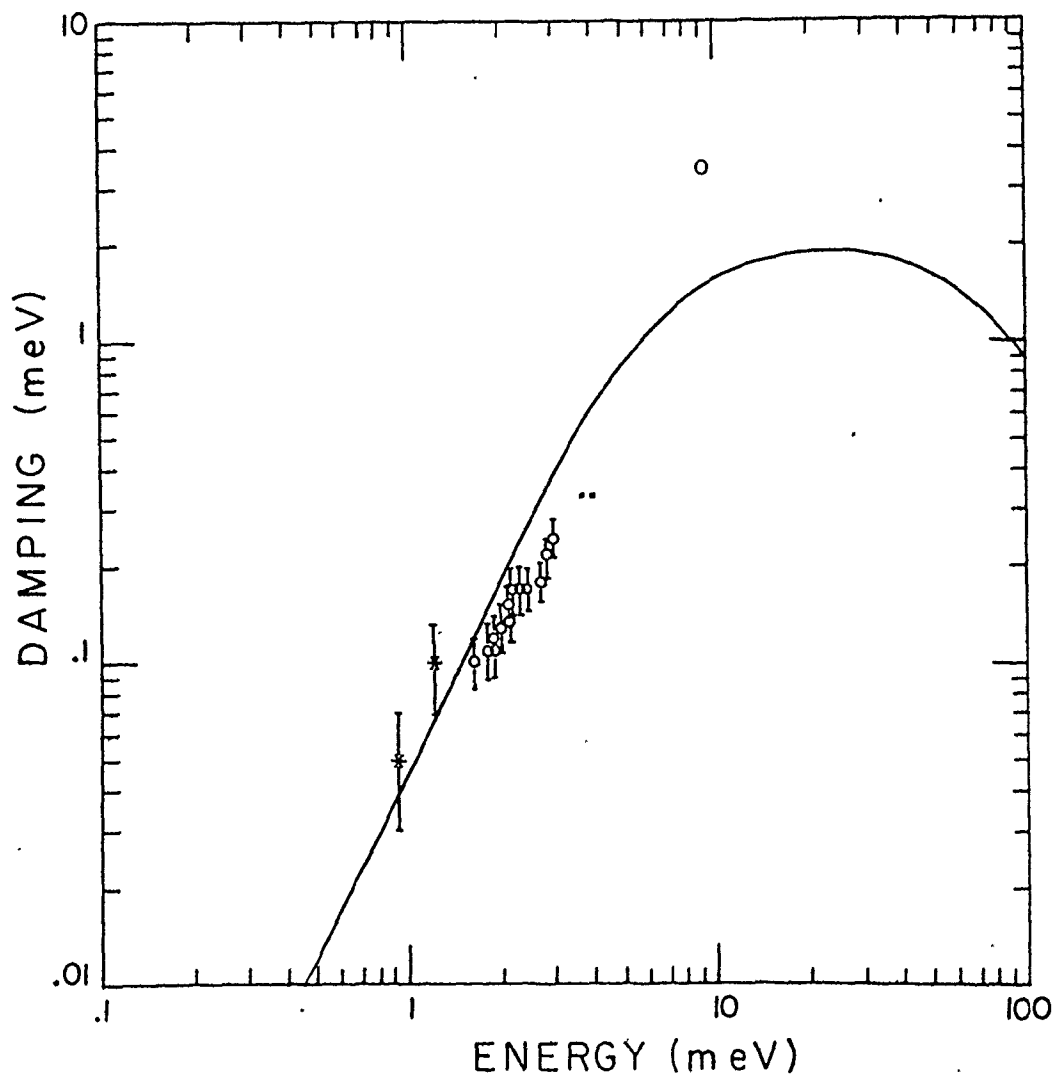
tering with holes in the light-hole band, as well as with ones that when scattering occurs jump from one valance band to the other, are considerably smaller. No dynamic correlations have been considered in this calculation of the electron-hole damping. This approximation gives an overall value somewhat smaller than that necessary to explain the width of the plasma resonance, but agrees well at low frequencies with the experimental results of magneto-plasma resonance of Gavrilenko et al., (1976), Muro and Nisida, (1976), and Gavrilenko et al., (1977) as can be seen from figure 6-1.

The overall fit with the theoretical model to the experimental far infrared absorption is very good but there are still some discrepancies with the value of the electron-hole pair density obtained from luminescence experiments, (Thomas et al., 1973). The variation of the EHD line shape with laser power is consistent with an increase in droplet size with excitation level. At very low powers the drops can no longer be considered uniform spheres, since surface effects are important; within a coat of the order of the excitonic Bohr radius the density is lower than that of the bulk. At these levels the Rayleigh approximation holds. At high laser powers a complete Mie theory is necessary to explain the line shape.

Application of uniaxial stress alters the band structure of Ge affecting the properties of the electron-hole liquid and thus its far infrared absorption. The changes are stronger

Fig. 6-1

Comparison between theoretical and experimental values of damping in Ge. The solid line is the same as fig. 3-8. The experimental points come from magnetoplasma-resonance measurements: the circles are from Gavrilenko et al. (1976), the squares from Muro and Nisida (1976), and the stars from Gavrilenko et al. (1977).





when the stress is applied parallel to one of the conduction band main directions ( $[111]$  in Ge). The strong anisotropy of the conduction band produces a strong dependence of the plasma frequency on the direction of the electric field with respect to the stress axes. Its value and hence the electron-hole density decreases with increasing stress with a sharp jump when the conduction valleys that are not aligned along the stress direction empty. Further decreases in the plasma resonance are produced by changes in the valence band. At the highest stresses applied in these experiments the plasma resonance is still considerably larger than the value extrapolated at infinite stress, indicating that the valence bands are still strongly coupled.

In general, the approximations and models used in the calculation of the theoretical lineshapes give very good agreement with the experimental results. The only exception is the high energy region of Ge under intermediate  $[111]$  stress where an additional maximum appears. A possible explanation for this extra absorption is the presence of hot electrons in the system condensed in an electron-hole fluid of higher density than the normal phase. Many interesting experiments are possible in this area: the study of the variation of hot electron concentrations as a function of temperature, the possible condensation in the high density phase and its phase diagram, are just a few examples.

## APPENDIX

## EFFECTS OF STRESS IN THE VALENCE BAND OF Ge

a) The energy bands:

The effects of deformation on the hole energy band of germanium and silicon was originally considered by G.E. Pikus and G.L. Bir (1959). J.C. Hensel and G. Feher (1963) obtained the inverse mass parameters and deformation potentials in uniaxially stressed silicon using cyclotron resonance. A similar study in Ge was done by J.C. Hensel and K. Suzuki (1974).

As I discussed in section 3.2, in the absence of stress and spin-orbit interaction, the valence band in Ge and Si is sixfold degenerate at the zone centre with symmetry  $\Gamma_{25}$ . This multiplet is comprised of three bands each two fold degenerate due to spin. In the vicinity of  $\underline{k} = 0$  the shape of the bands can be determined using  $\underline{k} \cdot \underline{p}$  perturbation theory ( $\underline{p}$  = momentum operator) (G. Dresselhaus, A.F. Kip and C. Kittel, 1955).

Spin-orbit interaction partially removes the degeneracy at  $k = 0$ . It is quite strong in Ge with a splitting at  $k = 0$  of 300 meV, much larger than the stress effects and the effects of the  $\bar{k} \cdot \bar{p}$  perturbation near the zone centre. In this case the six-dimensional space is broken into a four-dimensional  $j = \frac{3}{2}$  subspace and a two-dimensional  $j = \frac{1}{2}$  subspace.

Application of uniaxial stress breaks the  $j = \frac{3}{2}$  multi-

plet into two Kramers doublets and the cubic symmetry is removed.

Kleiner and Roth (1959) constructed a strain Hamiltonian in terms of the angular momentum operator  $\bar{J}$  ( $j = \frac{3}{2}$ ) to describe the splitting of the states at  $\underline{k} = 0$ . It is a Hamiltonian to first order in the strain components and reflects the symmetry of the system.

$$H_e = D_d^V(e_{xx} + e_{yy} + e_{zz}) + \frac{1}{3} D_u \left\{ (J_x^2 - \frac{1}{3} J^2) e_{xx} + \text{c.p.} \right\} + \frac{1}{3} D_u' \left\{ \{J_x J_y\} e_{xy} + \{J_z J_x\} e_{xz} + \{J_y J_z\} e_{yz} \right\} \quad (\text{A-1})$$

$e_{xx}, e_{xy}$  etc. are the strain components.  $D_d^V$ ,  $D_u$  and  $D_u'$  are deformation potentials with the last two describing the splittings for uniaxial stress along the  $[0,0,1]$  and  $[1,1,1]$  directions respectively. For  $\underline{k} \neq 0$  the Hamiltonian for the  $\underline{k} \cdot \underline{p}$  perturbation  $H_k$ , must be added to A-1 (Luttinger, 1956). There are no linear terms in  $\underline{k}$  in the expansion of  $E(\underline{k})$  near the minimum, second order terms are the only ones to be considered.

$$H_k = Ak^2 + \gamma_2 \left\{ [J_x^2 + \frac{1}{3} J^2] k_x^2 + \text{c.p.} \right\} + \gamma_3 \left\{ \{J_x J_y\} k_x k_y + \text{c.p.} \right\} \quad (\text{A-2})$$

where  $\gamma_2$  and  $\gamma_3$  are related to the Kittel notation band constants from Table 1 by:

$$\gamma_2 = -\frac{B}{2} \quad (\text{A-3})$$

$$\gamma_3 = \frac{1}{2\sqrt{3}} (3B^2 + C^2)^{1/2} \quad (\text{A-4})$$

The non-diagonal part of  $H_0 = H_e + H_k$  applied to the eigenfunctions of  $j = \frac{3}{2}$  gives the matrix below:

$$H_0^2 \begin{pmatrix} L & M & N & 0 \\ M^* & -L & 0 & N \\ N^* & 0 & -L & -M \\ 0 & N^* & -M^* & L \end{pmatrix} \quad (\text{A-5})$$

with

$$L = 3\gamma_2 \left( k_z^2 - \frac{k_x^2}{3} \right) + D_u (e_{zz} - \frac{(e_{xx} + e_{yy} + e_{zz})}{3})$$

$$M = 2\sqrt{3}\gamma_3 (k_y k_z + i k_x k_z) + \frac{2}{\sqrt{3}} D_u' (e_{yz} + i e_{xz})$$

$$N = \sqrt{3}\gamma_2 (k_y^2 - k_x^2) + \frac{D_u}{\sqrt{3}} (e_{yy} - e_{xx}) + 2i\sqrt{3}\gamma_3 k_x k_y + \frac{2i}{\sqrt{3}} D_u' e_{xy}$$

The eigenvalues  $\lambda$  of  $H_0^2$  are the solutions of the fourth order determinant:

$$\left\| H_0^2 - \lambda I \right\| \quad (\text{A-6})$$

The solutions to (A-6) are  $\epsilon_{12} = \pm \epsilon$  with:

$$\epsilon = \sqrt{L^2 + |M|^2 + |N|^2} \quad (\text{A-6})$$

Clearly a twofold degeneracy remains (Kramers theorem)

b) Stress parallel to [111]

For  $S \parallel [111]$  the strain components are related to the applied stress  $S$  by:

$$\begin{aligned} e_{xx} = e_{yy} = e_{zz} &= (S_{11} + 2S_{12})S \\ e_{xy} = e_{xz} = e_{yz} &= \frac{S_{44}S}{3} \end{aligned} \quad (\text{A-8})$$

where  $S_{11}$ ,  $S_{12}$  and  $S_{44}$  are cubic elastic compliance constants. For energies measured from the vertex of the heavy-hole band (positive energies), then:

$$E_{\pm} = (-A)k^2 + |E_0| \pm \sqrt{B^2k^4 + C^2(k_x^2k_y^2 + \text{c.p.}) + 4\gamma_3 E_0(k_xk_y + \text{c.p.}) + E_0^2} \quad (\text{A-9})$$

where c.p. means cyclic permutation  $E_0 = \frac{1}{3} D_u S_{44} S$ .

The expression (A-9) reduces to the heavy hole and light hole energies for  $S = 0$ .

The splitting  $\Delta_h$  of the two bands at  $K=0$  is:

$$\Delta_h = 2|E_0| = \frac{2}{3} |D_u S_{44} S| = 0.366 \frac{\text{meV}}{(\text{kg}/\text{mm}^2)} |S| \quad (\text{A-10})$$

for Ge under [111] stress.

c) Wave functions

We have seen that (A-5) gives the effect of the perturbing Hamiltonian on the basis  $\psi_i$  (eigenfunctions of  $j = \frac{3}{2}$ ), then:

$$H_0 \psi_i = \sum_j a_{ij} \left| \frac{3}{2}, m_j \right\rangle \quad (a_{ij} = \{H_0^2\}) \quad (\text{A-11})$$

The basis functions  $\phi_k$  for the Hamiltonian can be obtained in terms of the  $\psi_j$

$$H_0 \phi_k = E_k \phi_k \quad (\text{A-12})$$

$$\phi_k = \sum_j b_{kj} \left| \frac{3}{2}, mj \right\rangle$$

then:

$$\sum_{ij} b_{ki} (a_{ij} - E_k \delta_{ij}) \left| \frac{3}{2}, mj \right\rangle . \quad (\text{A-13})$$

From A-13 we can obtain the coefficients  $b_{ki}$  that give the eigenfunctions as a linear combination of the  $\left| \frac{3}{2}, mj \right\rangle$ .

The degenerate eigenfunctions corresponding to  $E_+$  are:

$$\begin{cases} \phi_1 = \frac{1}{((E-L)2E)^{1/2}} [M \left| \frac{3}{2}, \frac{3}{2} \right\rangle + N^* \left| \frac{3}{2}, -\frac{3}{2} \right\rangle + (E-L) \left| \frac{3}{2}, \frac{1}{2} \right\rangle] \\ \phi_2 = \frac{1}{((E-L)2E)^{1/2}} [N \left| \frac{3}{2}, \frac{3}{2} \right\rangle - M^* \left| \frac{3}{2}, -\frac{3}{2} \right\rangle + (E-L) \left| \frac{3}{2}, -\frac{1}{2} \right\rangle] \end{cases} \quad (\text{A-14})$$

For  $E_-$

$$\begin{cases} \phi_3 = \frac{1}{((E-L)2E)^{1/2}} [(E-L) \left| \frac{3}{2}, \frac{3}{2} \right\rangle - M^* \left| \frac{3}{2}, \frac{1}{2} \right\rangle - N^* \left| \frac{3}{2}, -\frac{1}{2} \right\rangle] \\ \phi_4 = \frac{1}{((E-L)2E)^{1/2}} [(E-L) \left| \frac{3}{2}, -\frac{3}{2} \right\rangle - N \left| \frac{3}{2}, \frac{1}{2} \right\rangle + M \left| \frac{3}{2}, -\frac{1}{2} \right\rangle] \end{cases} \quad (\text{A-15})$$

#### d) Absorption matrix elements

As it was discussed in Chapters 3 and 5, interband and intraband matrix elements between the heavy and light hole valence band are necessary to obtain the dielectric constant of electron-hole drops. For stressed Ge these matrix elements were first

calculated by A. Manoliu (1976). I will follow his procedure. Combescot and Nozières (1972) consider the density fluctuation  $\rho_{\bar{q}}^V$  that describes transitions from  $\bar{k}$  to  $(\bar{k}+\bar{q})$  inside the valence band, they show that  $\rho_{\bar{q}}^V$  is a unit matrix in the Kohn-Luttinger basis (eigenfunctions of  $j = \frac{3}{2}$ ). At  $k \neq 0$  the matrix elements between two eigenstates  $k_n, k'_n$  are:

$$(\rho_{\bar{q}}^V)_{k_n, k'_n} = \langle \bar{k}_n | e^{i\bar{q} \cdot \bar{r}} | k'_n \rangle = \sum_i U_{ni}^\dagger(\bar{k}) U_{in}(\bar{k}') \quad (\text{A-16})$$

where  $U(\bar{k})$  is the rotation that brings the eigenfunctions  $\phi_i$  (from (A-14) and (A-15)) to the Kohn-Luttinger basis:

$$U = \begin{pmatrix} \frac{M}{(2E(E-L))^{1/2}} & \frac{N}{(2E(E-L))^{1/2}} & \left(\frac{E-L}{2E}\right)^{1/2} & 0 \\ \left(\frac{E-L}{2E}\right)^{1/2} & 0 & \frac{-M^*}{(2E(E-L))^{1/2}} & \frac{-N}{(2E(E-L))^{1/2}} \\ 0 & \left(\frac{E-L}{2E}\right)^{1/2} & \frac{-N^*}{(2E(E-L))^{1/2}} & \frac{M}{(2E(E-L))^{1/2}} \\ \frac{N^*}{(2E(E-L))^{1/2}} & \frac{-M^*}{(2E(E-L))^{1/2}} & 0 & \left(\frac{E-L}{2E}\right)^{1/2} \end{pmatrix} \quad (\text{A-17})$$

For the band with eigenvalue  $E_+$  the intraband matrix element is given by

$$\rho_{\text{intra}}^2 = |\langle \phi_1(\bar{k}) | e^{i\bar{q} \cdot \bar{r}} | \phi_1(\bar{k}') \rangle|^2 + |\langle \phi_1(\bar{k}) | e^{i\bar{q} \cdot \bar{r}} | \phi_2(\bar{k}') \rangle|^2 \quad (\text{A-18})$$

An equivalent expression holds for  $E_-$  with  $\phi_3$  and  $\phi_4$  replacing  $\phi_1$  and  $\phi_2$ .

From (A-14), (A-15) and (A-17), it can be seen that  $\rho_{intra}^2$  is the same for both bands and is given by:

$$\rho_{intra}^2 = \frac{2EE' + 2LL' + MM'^* + M'M^* + NN'^* + N'N^*}{4EE'} \quad (A-19)$$

where the prime indicates that they are functions of  $k'$  instead of  $k$ .

The interband matrix elements are given by:

$$\rho_{inter}^2 = |\langle \phi_i | e^{i\bar{q} \cdot \bar{r}} | \phi_3 \rangle|^2 + |\langle \phi_1 | e^{i\bar{q} \cdot \bar{r}} | \phi_4 \rangle|^2 \quad (A-20)$$

$$\rho_{inter}^2 = 1 - \rho_{intra}^2 = \frac{2EE' - (2LL' + MM'^* + M'M^* + NN'^* + N'N^*)}{4EE'} \quad (A-21)$$

with  $E$ ,  $L$ ,  $M$  and  $N$  given by equations (A-6) and (A-8).

For stress along  $[1,1,1]$ :

$$\begin{aligned} \rho_{intra}^2 \times 2EE' = & \frac{2}{2} [(3k_z^2 - k^2)(3k_z'^2 - k'^2) + 3(k_x^2 - k_y^2)(k_x'^2 - k_y'^2)] \\ & + 12\gamma_3^2 (k_x k_y k_x' k_y' + c.p.) + 2\gamma_3 E_0 [k_x k_y + c.p. + k_x' k_y' + c.p.] + E_0^2 \end{aligned} \quad (A-22)$$

where

$$k_z' = k_z + q_z, \quad k_y' = k_y + q_y, \quad k_x' = k_x + q_x$$

$$\bar{q} = q(\hat{q}_x, \hat{q}_y, \hat{q}_z)$$

For optical transitions  $\bar{q}$  is very small as compared with the Fermi wavevector. Expanding (A-21) in powers of  $q$ , and considering second order terms, the following expression is obtained (Markiewicz, 1978b)



$$\rho_{\text{inter}}^2 = \frac{1}{2E^2} \left[ F_2 - \frac{F_1^2}{E^2} \right] \quad (\text{A-23})$$

with:

$$\begin{aligned} F_1 = & q \{ 12(\gamma_2^2 - \gamma_3^2) (k_x^3 \hat{q}_x + \text{c.p.}) + \\ & + (12\gamma_3^2 - 4\gamma_2^2) k^2 (k_x \hat{q}_x + \text{c.p.}) + \\ & + 2\gamma_3 E_0 [(\hat{q}_x + \hat{q}_y + \hat{q}_z) (k_x + k_y + k_z) - (\hat{q}_x k_x + \text{c.p.})] \} \end{aligned} \quad (\text{A-24})$$

$$\begin{aligned} F_2 = & q^2 \{ 24(\gamma_2^2 - \gamma_3^2) (k_x^2 \hat{q}_x^2 + \text{c.p.}) + 12\gamma_3^2 k^2 q^2 + \\ & + (12\gamma_3^2 - 8\gamma_2^2) (k_x \hat{q}_x + \text{c.p.})^2 \}. \end{aligned} \quad (\text{A-25})$$

At zero stress and in the spherical approximation for the energy bands (A-23), (A-24) and (A-25) give the same result that Combescot and Noziere's. In this case with  $\gamma_2 = \gamma_3$

$$E^2 = 4\gamma_2^2 k^4$$

$$F_1 = q(8\gamma_2^2) k^3 \cos\theta$$

$$F_2 = q^2 4\gamma_2^2 k^2 \cos^2\theta + 12\gamma_2^2 k^2 q^2$$

( $\theta$ : angle between  $\hat{q}$  and  $\hat{k}$ )

$$\rho_{\text{inter}}^2 \quad \left( \begin{array}{l} (S=0) \\ \gamma_2 = \gamma_3 \end{array} \right) = \frac{4}{3} \frac{q^2}{k^2} \sin^2\theta \quad (\text{A-26}).$$

## BIBLIOGRAPHY

- Aksenov, V.P. and Zhurkin, B.G. (1980), Solid State Comm. 33, 1033.
- Alekseev, A.S., Astemirov, T.A., Bagaev, V.S., Galkina, T.I., Penin, N.A., Sybeldin, N.N., and Tsvetkov, V.A., (1974), Proceedings of the Twelfth International Conference on the Physics of Semiconductors, Stuttgart, 1974, edited by M.H. Pilkuhn (Teubner, Stuttgart), p. 152.
- Alekseev, A.S., Bagaev, V.S., Galkina, T.I. (1973), Zh. Eksp. Teor. Fiz. 63, 1020 (1972) [Sov. Phys.-JETP 36, 536 (1973)].
- Asnin, V.M., Rogachev, A.A., and Ryvkin, S.M., (1968), Fiz. Tekh. Poluprovodn. 1, 1742 (1967) [Sov. Phys.-Semicond. 1, 1447 (1968)].
- Aurbach, R.L., Eaves, L., Markiewicz, R.S., and Richards, P.L., (1976), Solid State Comm. 19, 1023.
- Bagaev, V.S., Galkina, T.I., Gogolin, O.V., and Keldysh, L.V., (1969), Pis'ma Zh. Eksp. Teor. Fiz. 10, 309 [JETP Lett. 10, 195].
- Bagaev, V.S., Zamkovets, N.V., Keldysh, L.V., Sibel'din, N.N. and Tsvetkov, V.A., (1976), Zh. Eksp. Teor. Fiz. 70, 1501 [Sov. Phys. JETP, 43, 783].
- Balslev, I., (1966), Phys. Rev. 143, 636.
- Benôit à la Guillaume, C., Voos, M., and Salvan, F., (1970), J. Lumin. 1/2, 315.
- Benôit à la Guillaume, C., Voos, M., and Salvan, F., (1972), Phys. Rev. B 5, 3079.

- Brinkman, W.F. and Rice, T.M., (1973), Phys. Rev. B7, 1508.
- Chou, H.-h. and Wong, G.K., (1978), Phys. Rev. Lett. 41, 1677.
- Chou, H.-h., Wong, G.K., and Feldman, B.J., (1977), Phys. Rev. Lett. 39, 959.
- Combescot, M. and Nozières, P., (1972), J. Phys. C 5, 2369, and Solid State Comm. 10, 301.
- Dresselhaus, G., Kip, A.F., and Kittel, C., (1955), Phys. Rev. 98, 368.
- Drew, D.H. and Sievers, A.J., (1967), J. Appl. Optics, 8, 2067.
- Ehrenreich, H. and Cohen, M.H., (1959), Phys. Rev. 115, 786.
- Etienne, B., Benôit à la Guillaume, C., and Voos, M., (1975), Phys. Rev. Lett. 35, 536.
- Euler, J., (1954), Z. Phys. 137, 319.
- Feldman, B.J., Chou, H.-h., and Wong, G.K., (1977), Solid State Comm. 24, 521.
- Feldman, B.J., Chou, H.-h. and Wong, G.K., (1978), Solid State Comm. 26, 209.
- Garrilenko, V.I., Kononenko, V.L., Mandel'shtam, T.S., and Murzin, V.N., (1976), Pis'ma Zh. Eksp. Teor. Fiz. 23, 701 [JETP Lett. 23, 645].
- Gavrilenko, V.I., Kononenko, V.L., Mandel'shtam, T.S., Murzin, V.N., and Saunin, S.A., (1977), Pis'ma Zh. Eksp. Teor. Fiz. 26, 102 [JETP Lett. 26, 95].
- Gershenson, E.M., Gol'tsman, G.N., and Ptitsina, N.G., (1976), Zh. Eksp. Teor. Fiz. 70, 224 [Sov. Phys.-JETP 43, 116].

- Gurzhi, R.N., and Kaganov, M.I., (1965), Zh. Eksp. Teor. Fiz. 49, 941 [Sov. Phys.-JETP 22, 654].
- Haller, E.E. and Hansen, W.L., (1974), IEEE Trans. Nucl. Sci. 21, 279.
- Hensel, J.C. and Feher, G., (1963), Phys. Rev. 129, 1041.
- Hensel, J.C. and Suzuki, K., (1974), Phys. Rev. B 9, 4219.
- Hensel, J.C., Phillips, T.G. and Thomas, G.A., (1977), The Electron-hole Liquid in Semiconductors: Experimental Aspects, in: Solid State Physics, Vol. 32, ed. H. Ehrenreich, F. Seitz and D. Turnbull (Academic, N.Y.) p. 87-314.
- Herman, F., (1955), Proc. Inst. Radio Engrs. 43, 1703.
- Hulst, van de H.C., (1957), Light Scattering Small Particles, (Wiley, New York).
- Kalia, R.K. and Vashishta, P., (1978), Phys. Rev. 17, 2655.
- Kane, E.O., (1975), Phys. Rev. B 11, 3850.
- Kapitsa, P.L., (1941), Zh. Eksp. Teor. Fiz., 11, 1.
- Keldysh, L.V., (1968), Proceedings of the Ninth International Conference on the Physics of Semiconductors, Moscow, Edited by S.M. Ryvkin, (Nauka, Leningrad).
- Kelso, S.M., (1979), thesis, University of California, Berkeley.
- Kerker, M., (1969), The Scattering of Light and Other Electromagnetic Radiation (Academic, New York).
- Kirczenow, G., and Singwi, K.S., (1978), Phys. Rev. Lett. 41, 326.
- Kirczenow, G. and Singwi, K.S., (1979), Phys. Rev. B 19, 2117.

- Kittel, C., (1973), Introduction to Solid State Physics 4th ed., Wiley and Sons, New York.
- Kleiner, W.H. and Roth, L.M., (1959), Phys. Rev. Lett. 2, 334.
- Kohn, W., (1965), Solid State Phys. 5, 257.
- Kubo, R., (1957), J. Phys. Soc. Japan 12, 570.
- Lax, B., and Mavroides, J.G., (1955), Phys. Rev. 100, 1650.
- Levinger, B.W. and Frankl, D.R., (1961), J. Phys. Chem. Solids 20, 281.
- Lindhard, J., (1954), K. Dan. Vidensk. Selsk. Mat. Fys. Medd. 28, 8.
- Liu, L., (1978a), Solid State Comm. 25, 805.
- Liu, L. and Liu, L.S., (1978b), Solid State Comm. 27, 801.
- Lo, T.K., (1974), Solid State Comm. 15, 1231.
- Luttinger, J. M., (1956), Phys. Rev. 102, 1030.
- Manenkov, A.A., Mikhailova, G.N., Seferov, A.S., and Chernetskii, V.D., (1974), Fiz. Tverd. Tela, 16, 2719 [Sov. Phys. Solid State, 16, 1757].
- Manoliu, A., (1976), Private communication.
- Markiewicz, R.S., (1978a), Bull. Am. Phys. Soc. 23, 423.
- Markiewicz, R.S., (1978b), Private communication.
- Markiewicz, R.S. and Kelso, S.M., (1978), Solid State Comm. 25, 275.
- Muro, K. and Nisida, Y., (1976), J. Phys. Soc. Jpn. 40, 1069.
- Murzin, V.N., Zayats, V.A., and Kononenko, V.L., (1975), Fiz. Tverd. Tela 17, 2684 [Sov. Phys. Solid State 15, 2421].
- Navarro, H., (1979), Thesis, McMaster University.
- Pak, S., (1975), Thesis, McMaster University.

- Pikus, G.E. and Bir, G.L., (1959), Fiz. Tverd. Tela 1, 1642  
[Sov. Phys. Solid State 1, 1502].
- Pokrovskii, Ya. E. and Svistunova, K.I., (1970), Fiz. Tekh.  
Poluprov. 4, 491 [Sov. Phys.-Semicond. 4, 409].
- Pokrovskii, Ya. E. and Svistunova, K.I., (1974), Proceedings  
of the Twelfth International Conference on the Physics of  
Semiconductors, Stuttgart, 1974, edited by M.H. Pilkhun  
(Teubner, Stuttgart), p. 71.
- Rice, T.M., (1977), The Electron-hole Liquid in Semiconductors:  
Theoretical Aspects, in: Solid State Physics, Vol. 32, ed.  
H. Ehrenreich, F. Seitz, and D. Turnbull (Academic, N.Y.)  
p. 1-86.
- Rose, J.H. and Shore, H.B., (1975), Bull. Am. Phys. Soc., 20,  
470, and, Rice, T.M., (1975), Bull. Am. Phys. Soc. 20, 470.
- Rose, J. H., Shore, H.B., and Rice, T.M., (1978), Phys. Rev.  
B 17, 752.
- Sherrington, D. and Kohn, W., (1968), Phys. Rev. Lett. 21, 153.
- Silver, R.N., and Aldrich, C.H., (1978), Phys. Rev. Lett. 41,  
1249.
- Suzuki, K. and Hensel, J.C., (1974), Phys. Rev. B 9, 4184.
- Thomas, G.A., Phillips, T.G., Rice, T.M. and Hensel, J.C., (1973),  
Phys. Rev. Lett. 31, 386.
- Thomas, G.A. and Pokrovskii, Ya. E., (1978), Phys. Rev. B 18, 864.
- Timusk, T. and Lin, F.K., (1980), Proc. of the 35th Symposium  
on Molecular Spectroscopy, Columbus, Ohio, p. 68.

- Timusk, T. and Silin, A., (1975), Phys. Status Solidi 69, 87.
- Timusk, T. and Zarate, H.G., (1977), AIP Conf. Proc. 40, 324.
- Timusk, T. and Zarate, H.G., (1981), Bull. Am. Phys. Soc. 26, 487.
- Tzoar, N. and Platzman, P.M., (1976), Linear and Non-Linear Electron Transport in Solids, edited by Devreese and Van Doren (Plenum, New York), p. 199.
- Vashishta, P., Bhattacharyya, P., and Singwi, K.S., (1974), Phys. Rev. B 10, 5108, and, Vashishta, P., Das, S.G., and Singwi, K.S., (1974), Phys. Rev. Lett. 33, 911.
- Vashishta, P., Kalia, R.K., and Singwi, K.S., (1976), Lecture Notes in Physics, edited by M. Veta and Y. Nishina, Vol. 57, (Springer-Verlag, Heidelberg), p. 187.
- Vavilov, V.S., Zayats, V.Z., and Murzin, V.N., (1969), Pis'ma Zh. Eksp. Teor. Fiz. 10, 304 [JETP Lett. 10, 195].
- Voos, M., Shaklee, K.L., and Worlock, J.M., (1974), Phys. Rev. Lett. 33, 1161.
- Westervelt, R.M., (1976), Phys. Status Solidi B 76, 31.
- Worlock, J.M., Damen, T.C., Shaklee, K.L., and Gordon, J.P., (1974), Phys. Rev. Lett. 33, 771.
- Zarate, H.G., Carbotte, J.P., and Timusk, T., (1980), Phys. Rev. B 21, 4649.
- Zarate, H.G. and Timusk, T., (1979), Phys. Rev. B 19, 5223.
- Zayats, V.A., Murzin, V.N., Salganik, I.N., and Shifrin, K.S., (1977), Zh. Eksp. Teor. Fiz. 73, 1422 [Sov. Phys. JETP 46, 748].
- Zinov'eva, K.N., (1971), Zh. Eksp. Teor. Fiz. 60, 2243 [Sov. Phys.-JETP 33, 1205].